UiO : **Department of Physics**
University of Oslo

Active Spacecraft Potential Control of the CubeSTAR Nano-satellite

and Prototype Development of a Miniaturized Electron Gun

Master Thesis

Espen Sørlie Helgeby

December 2013

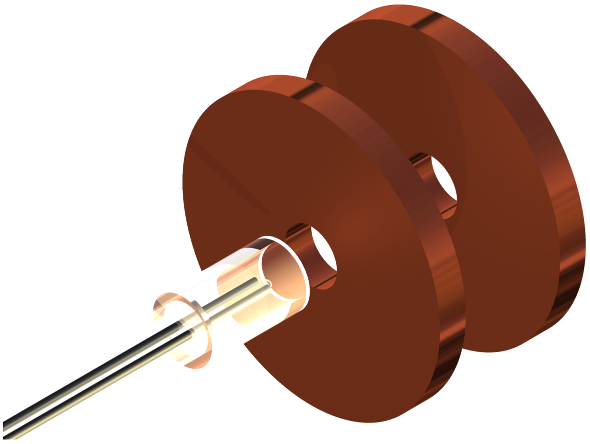

Abstract

This thesis presents a method for providing active spacecraft potential control of the CubeSTAR nano-satellite. The scientific instrument on the satellite, called the multi-Needle Langmuir Probe (m-NLP) system, requires that the spacecraft potential is stable and close to the plasma potential for optimum performance. The development and testing of a low power, miniaturized size thermionic electron gun specifically designed for small CubeSats is described. A review of different spacecraft charging mitigation methods is given, and a transparent conductive coating is proposed for rendering the photovoltaic cells' surfaces conductive. Together with the m-NLP system the spacecraft potential can be measured and controlled.

The electron gun works by emitting electrons from a commercially available light bulb rated for 3 V at 17 mA, which is acceptable for the limited power budgets associated with CubeSats. A mechanical design of the electrodes not found in the literature is presented. This novel design uses plated through-holes on printed wiring boards as the apertured electrodes. Printed wiring boards can be regarded as commercial off-the-shelf products making it an excellent choice for low-cost satellites such as CubeSats. Having the electrodes already supported by an insulating material reduces mechanical parts and making it less fragile and space-consuming. The electrodes are supported and aligned by four metal screws through the insulating part of the printed wiring boards. The electron gun measures 15 × 15 × 10 mm and is capable of emitting a current in the high nA-range with a bias voltage of up to 40 V. A substitute filament rated for 105 mW has been found with an emission current in the desirable low μA-range. Active spacecraft potential control of a preliminary CubeSTAR model was successfully shown during testing in the plasma chamber at the ESA space centre ESTEC.

Preface

The work presented in this master thesis was carried out in the period from January 2012 to December 2013, under the supervision of Associate professor Torfinn Lindem at UIO Electronics Group and Arne Pedersen at UIO Plasma- and Space Physics Group.

I would like to thank Associate professor Torfinn Lindem for introducing me to the CubeSTAR project, for giving me the opportunity to work in such an interesting field and for his encouragement. I would also like to thank Professor emeritus Arne Pedersen for the many fruitful discussions we had regarding the physics behind electron guns and spacecraft charging, and for sharing his many interesting stories. My very great appreciation goes to PhD candidate Tore André Bekkeng for his help and guidance throughout the entire period. Furthermore, I would like to thank everyone who have helped me fill all the necessary roles this interdisciplinary project has demanded. First off, I would like to thank Steinar Skaug Nilsen and the rest of the staff at the mechanical workshop at the Department of Physics. Their help in fabricating the various prototypes, the custom built endplate for the vacuum chamber and the mechanical test fixture has been crucial for the completion of this thesis. I am also grateful for the practical help and advice provided to me by the electrical workshop at the Department of Physics, and engineer Espen Trondsen at UiO Plasma- and Space Physics Group. I am particularly grateful to Viktor Bobal for granting me access to the cleanroom laboratory at MiNaLab, his assistance in running the vacuum chamber and for his useful comments. Furthermore, I wish to acknowledge the help and recommendations provided by Esben Lund in the work with the transparent conductive coating. I would also like to express my appreciation to Jean-Pierre Lebreton for his contribution and hospitality during testing in the ESTEC plasma chamber. To Knut Olav, Lars Jørgen, Bent and all fellow students, thanks for all the discussions, help and nonsense. Last, but not least, I would like to thank my family and friends for their support during these last months.

Oslo, Norway, December 2013
Espen Sørlie Helgeby

Contents

Nomenclature

$m - NLP$	multi-Needle Langmuir Probe
$P - POD$	Poly Picosatellite Orbital Deployer
ASPC	Active Spacecraft Potential Control
CDS	CubeSat Design Spesification
CIC	Solar cell + Interconnects + Coverglass
CVCM	Collected Volatile Condensable Material
DUT	Device Under Test
EGMS	Electron Gun Measurement System
GUI	Graphical User Interface
ITO	Indium Tin Oxide
LEO	Low Earth Orbit
PCB	Printed Cicruit Board
PEEK	Polyether Ether Ketone
PEO	Polar Earth Orbit
PS	Power Supply
PWB	Printed Wiring Board
SMU	Source Measurement Unit
TC	Transparent Conductor
TCR	Temperature Coefficient of Resistance
TiN	Titanium Nitride
TML	Total Mass Loss
VI	Virtual Instrument

List of Figures

List of Tables

Chapter 1

Introduction

This thesis gives an introduction to active spacecraft potential control (ASPC) and describes the design and development of a prototype miniaturized electron gun for the CubeSTAR nano-satellite. The scientific mission of the satellite, which is to perform electron density measurements in the ionosphere, requires that the floating potential of the satellite is close to the plasma potential. To accommodate this requirement, a method is proposed for rendering the surface of the satellite conductive which enables the electron gun control of the floating potential of CubeSTAR.

1.1 The CubeSTAR Project

CubeSTAR is a nano-satellite currently under development at the Department of Physics, University of Oslo (UiO). The project is part of the Norwegian Student Satellite Program (ANSAT), where CubeSTAR is the second out of three student satellites in Norway to be built and deployed into orbit. The program is being financially supported by the Norwegian Space Centre (NSC), while ANSAT itself is being run by the Norwegian Center for Space-related Education (NAROM) in cooperation with Andøya Rocket Range (ARR). The CubeSTAR project was initiated in 2008 and the satellite is expected to be deployed into orbit in 2014. The satellite is primarily being built through the work conducted in graduate thesis, which ensures that the academic goal of recruiting students to the space technology sector is being fulfilled.

1.1.1 The CubeSTAR Satellite

The CubeSTAR satellite is a double-unit CubeSat measuring 10 cm × 10 cm × 20 cm and with a total weight of no more than 2.66 kg. It is built after the *CubeSat Design Specification* (CDS) described in California Polytechnic State University (2009). The standard was developed by the aforementioned university in collaboration with Stanford University in order to reduce cost and development time of nano- and picosatellites. The CubeSTAR satellite consists of a back panel with five subsystems connected to it: (1) the electronic power system (EPS), (2) the attitude determination and control system (ADCS), (3) the on-board data handling (OBDH) system, (4) the communication system (COMM) and (5) the scientific payload. A picture of CubeSTAR is shown in Figure 1.1.

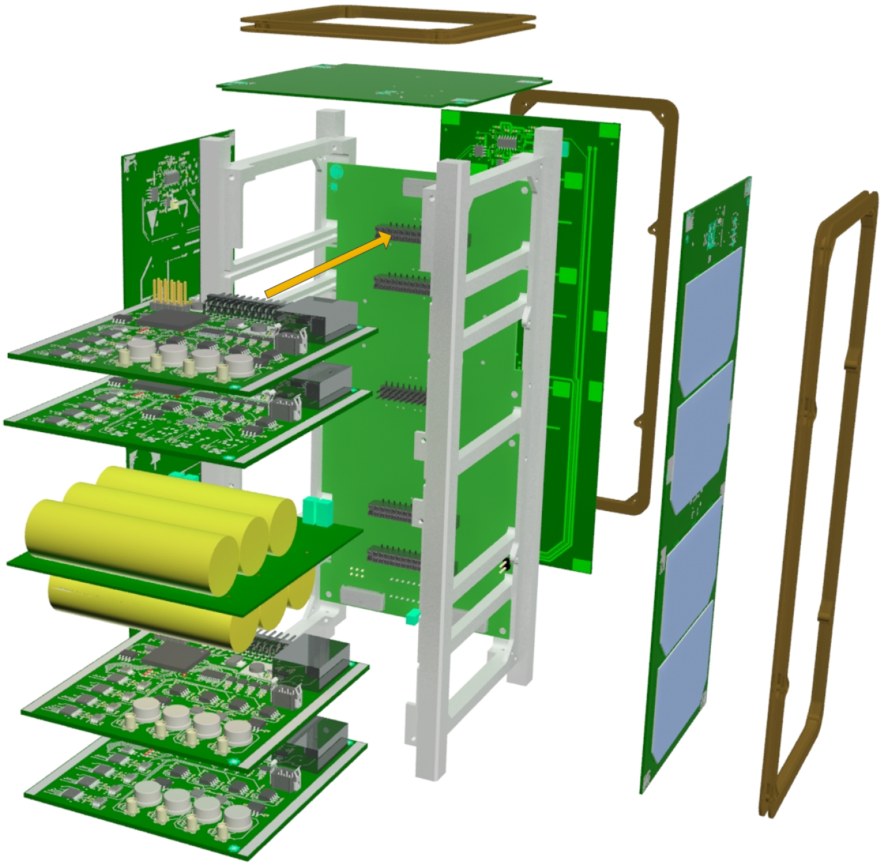

Figure 1.1: Shows CubeSTAR with its mechanical structure, back panel and subsystems. The scientific payload printed circuit board is placed in the top slot, and the EPS in the middle. The scientific payload printed circuit boards are duplicated for illustration purposes. By UiO (D.M. Bang).

Scientific Payload The scientific payload on CubeSTAR is a novel instrument invented at UiO for measuring the electron density in the ionospheric plasma. Electron clouds formed by ionization in the ionosphere disturb GPS signals and satellite communication, and better understanding of this phenomena can help resolve these issues. This new system, called the multi-Needle Langmuir Probe (m-NLP) system, achieves a spatial resolution down to sub-meter scale which is much lower than previously possible. The measurement principle was invented by Knut-Stanley Jacobsen while the instrument itself is being developed by PhD candidate Tore André Bekkeng. The m-NLP system has been verified in a plasma chamber as well as on sounding rockets with promising results.

Electronic power system The EPS provides continuous power to the satellite with an estimated orbital average power (OAP) of approximately 2 Watt according to Skyttemyr (2013). The EPS consists of triple junction photovoltaic cells covering most of the side panels, battery charges with integrated maximum power point tracking for full utilization of the energy harvested from the sun and Nanophosphate batteries for energy storage.

Attitude Determination and Control System The ADCS determines and controls the satellites attitude in space which is important to the scientific mission. The ADCS on CubeSTAR will be using a magnetometer, a gyroscope and sun sensors for attitude determination, and magnetourquer for control.

On-Board Data Handling The OBDH system includes a microcontroller which communicates with the different subsystems on the satellite using I^2C. It monitors and collects data, sends commands to the subsystems and maintains normal operation on the satellite autonomously.

Communication System The COMM uses a semi-duplex ultra high frequency transceiver for sending data to and receiving commands from the CubeSTAR ground station. It is also compatible with the GENSO network which increases the communication time with the satellite during orbit.

1.1.2 Mission Overview and Orbit

CubeSTAR will be deployed into orbit by a Poly Picosatellite Orbital Deployer (P-POD) together with several other CubeSats. As discussed above, the m-NLP system will be investigating the electron clouds in the ionosphere and choosing an orbit within the areas causing disturbances of GPS signals and satellite communication is important. The converging magnetic field lines at the north and south pole bring high energy particles to the auroral latitudes and contribute to ionizing the plasma. This is, together with the equatorial region, an interesting region for doing electron density measurements. The exact altitude and inclination of the orbit will be determined by the launch provider, however it is expected that CubeSTAR will have a low earth, polar orbit between 400-600 km at an inclination higher than 75°.

1.2 Goals of the Present Work

The main goal of this thesis is to provide active spacecraft potential control of the CubeSTAR nano-satellite. The focus will be on the development of an electron gun suitable for CubeSats, as this became the chosen method for potential control of CubeSTAR. Due to the lack of in-house knowledge, the prototype development of the electron gun is regarded as a pilot project. In addition, a measurement system needs to be built in order to characterise the performance of the electron gun. A method for rendering the surface of the satellite electrically conductive must furthermore be proposed. This involves a study on transparent conductive coatings, as it is important to keep the high efficiency of the photovoltaic cells covering most of the surface of the satellite. Laboratory testing at ESTEC and integration of the electron gun into CubeSTAR are the final goals.

1.3 Thesis Outline

In Chapter 2, the principles behind spacecraft charging is explained and methods for controlling the floating potential of a spacecraft are reviewed. This chapter results in the proposed method for actively controlling the spacecraft potential of CubeSTAR. The method involves having the surface of the satellite electrically conductive while an electron gun is used to dissipate electrons from the satellite's ground potential. From here the thesis naturally divides itself into two parts as explained next.

Chapter 3 reviews transparent conductive coatings necessary for rendering the solar cells' surfaces conductive. A literature study is presented alongside a short experimental study of one such coating.

Chapter 4 deals with the theory and design of electron guns, the foundation of the work to come. Chapter 5 discusses the design considerations for the electron gun, presents some solutions found in the literature and ends up with presenting the prototypes that were built. Chapter 5 mostly deals with the mechanical configuration of the prototypes, while the electrical configurations is derived through experiments and simulations presented in Chapter 7. The equipments used in the experiments and simulations are reviewed in Chapter 6.

Chapter 8 binds the two previously explained parts together in a system test performed in the plasma chamber at ESTEC - a proof of concept of the proposed method in Chapter 2.

Chapter 9 concludes the thesis and summarizes the work that remains.

Chapter 2

Spacecraft Potential Control

This chapter starts by describing the fundamentals of spacecraft charging and the effect it has on a spacecraft. The floating potential of CubeSTAR is then examined, which leads to the conclusion that an electron gun capable of emitting a current of 0.5 - 5 μA, or equivalent, is needed to control the potential. An overview of spacecraft charging mitigation methods is then given, together with the proposed method for CubeSTAR.

2.1 An Introduction to Spacecraft Charging

An object is said to be electrically charged when there is an imbalance between negative and positive charges, Q_i. The total electrical field strength at a point can be found by adding up the electrical field strength each point charge produces:

$$\vec{E} = \sum_{i=1}^{n} \frac{1}{4\pi\epsilon_0} \frac{Q_i}{r_i^2} \vec{u}_{ri} \quad (\frac{V}{m}) \tag{2.1}$$

where r_i is the distance to the point charge Q_i, $\mathrm{u}_{\vec{r}}$ is the unit vector and ϵ_0 the permittivity of free space. The potential difference between two points V_{AB} in an electric field can be found from the formula:

$$V_{AB} = \int_{A}^{R} \vec{E} \cdot d\vec{l} \quad (V) \tag{2.2}$$

In the field of spacecraft charging, the ambient space plasma potential, V_p, is usually defined as zero and the spacecraft potential, V_f, as floating relative to the plasma. Whenever the electrical charge of a spacecraft is different to that of the ambient plasma, the spacecraft potential is non-zero. This is illustrated in Figure 2.1.

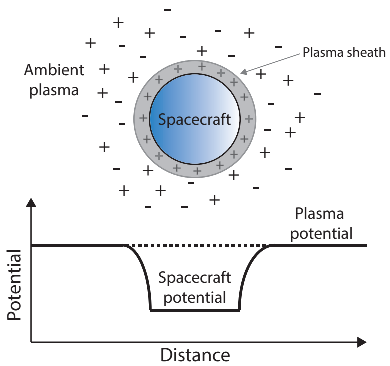

Figure 2.1: Shows the floating potential of a negatively charged spacecraft. It is seen that the potential of the spacecraft is negative, and the potential in the close proximity of the spacecraft surface is disturbed. Adapted from Lai (2012).

2.1.1 Types of Spacecraft Charging

There are different types of charging that can occur on a spacecraft. The type of charging that occurs depends on the environment around the spacecraft as well as on the spacecraft design and its orbit. The following terminology is used:

- **Absolute charging** describes the situation when the whole spacecraft is uniformly charged to one potential.
- **Differential charging** describes the situation when electrically separated surfaces charge to different potentials.
- **Surface charging** describes the charging that occurs on the surface, for instance on a conductive spacecraft.
- **Deep dielectric charging** describes the charging that occurs when high energetic particles penetrate into dielectrics.
- **Frame charging**, or structural charging, describes the charging of the connected conductive surfaces of a spacecraft.

In the most severe cases, spacecraft charging can lead to an electrostatic discharge which might disrupt or destroy onboard electronics. This happens when the potential difference and the resulting electrical field between two point becomes so high that ionization occurs, for instance due to differential charging. According to Lai (2012), severe spacecraft charging in the low earth orbit (LEO) is generally not of a concern. However, at higher latitudes more energetic particles can travel along the magnetic field lines and a spacecraft in polar earth orbit (PEO) may thus encounter more energetic plasma for a short period of time (Tribble 2003). It is stated by Lai that high-level surfaces charging can occur even at an altitude of 300 km at the auroral latitudes. The focus in this thesis will however be on the normal conditions encountered in the LEO environment.

2.1.2 The Current-Balance Equation

The floating potential of a spacecraft can be found by regarding Kirchhoff's current law (Lai 2012). Kirchhoff's current law states that the current, I_k, flowing into and out of a node in equilibrium must be equal:

$$\sum_{k=1}^{n} I_k = 0 \tag{2.3}$$

As a first approach, consider the surface charging of a stationary spacecraft in which only the electrons and the ions from the ambient plasma contributes to the current equation. Equilibrium will be reached when the current from the ions to the spacecraft is equal to the current from the electrons to the spacecraft. Kirchhoff's current law then becomes:

$$I_I + I_E = 0 \tag{2.4}$$

where I_I and I_E are the current from the ions and electrons to the spacecraft, respectively. This current-balance requirement will drive the spacecraft potential negative with respect to the plasma potential. The negative value of the equilibrium potential is explained by the difference in mass between the electrons and the ions. Due to the larger mass of the ions, and hence lower velocity, the electron flux to the spacecraft will be greater than the ion flux before equilibrium is reached. A charge build-up occurs which lowers the spacecraft potential. However, as the spacecraft potential gets lower, less electrons from the random electron population in the plasma will have enough kinetic energy to overcome the increasing retarding field from the spacecraft. When equilibrium is reached, only the higher energy part of the electron population contributes in the current-balance equation, and the current from the electrons to the spacecraft equals the current from the ions to the spacecraft. The overall current-balance equation for a given surface in equilibrium can be written as (Garrett and Whittlesey 2012):

$$I_T = I_E(V) - [I_I(V) + I_{SE}(V) + I_{SI}(V) + I_{BSE}(V) + I_{PH}(V) + I_B(V)] \tag{2.5}$$

V = spacecraft potential
I_E = incident electron current on spacecraft surface
I_I = incident ion current on spacecraft surface
I_{SE} = secondary electron current due to I_E
I_{SE} = secondary electron current due to I_I
I_{BSE} = backscattered electrons due to I_E
I_{PH} = photoelectron current
I_B = active current sources such as charged particle beams or ion thrusters
I_T = total current to spacecraft (at equilibrium, $I_T = 0$)

2.1.3 Plasma Sheath

A spacecraft, whose floating potential is different from the plasma potential, will attract charges of the opposite sign and repel those of the same sign. The result is a region outside the spacecraft with a lower density of the repelled charges and a higher density of the attracted charges. This is illustrated in Figure 2.1 where a negatively charged spacecraft has a plasma sheath with a surplus of positive charges. For spacecrafts doing measurements on the surrounding plasma, this means that the measurement object might be altered and erroneous measurements taken. The Debye length characterizes the scale length of the sheath. Spacecraft potentials in low earth orbit are effectively screened by the plasma sheath due to the high density of the plasma, and the Debye length is therefore typically around 1 cm.

2.1.4 Wake Region

A spacecraft in LEO has a *mesothermal* orbital velocity. The term mesothermal means that the spacecraft has a velocity between the lower-velocity ions and the higher-velocity electrons. As a result, the ions are collected only on the surface pointing in the direction of the spacecraft's orbital velocity, known as the ram side, while electrons can be collected on all sides. A region, known as the *wake* region, is formed behind the spacecraft which has a reduced ion density. This region acquires a negative charge, due to the lack of ions, which influences the collection of electrons on the wake-side of the spacecraft.

2.2 The multi-Needle Langmuir Probe System

The m-NLP system utilizes, as it's name implies, Langmuir probes for performing electron density measurements. A Langmuir probe is essentially a conductive body immersed in a plasma, and it experiences the same effects as recently explained. A Langmuir probe works by biasing the conductive body to a potential relative to the plasma potential, and measuring the collected current. For a Langmuir probe mounted on a spacecraft, the biasing voltage will be referenced to electrical ground, which is often connected to the frame. The floating potential of the probe will therefore acquire the same negative potential, V_f, with respect to the plasma potential, as the frame itself. This is seen in Figure 2.2 which shows a typical IV-curve for a Langmuir probe. At the plasma potential, V_p, there exists no sheath between the probe and the plasma. Electrons are attracted by the probe above this point while ions are repelled. Below this point, the opposite is true.

The m-NLP system consists of four cylindrical probes which are mounted on booms in the ram direction of the vessel it is situated. The booms shield the probes away from the plasma sheath caused by the vessel, so

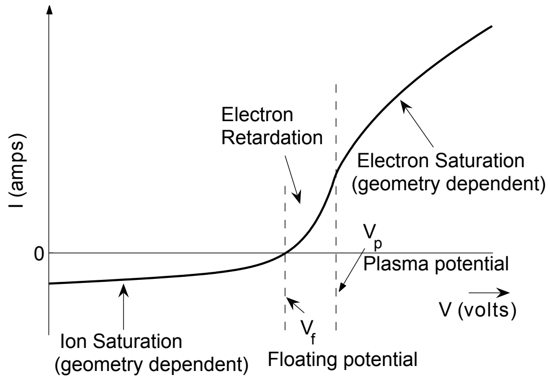

Figure 2.2: Shows the IV-curve of a Langmuir probe in a plasma. By Barjatya (2007).

the concern stated in Section 2.1.3 is no longer valid. A Langmuir probe can either operate on a fixed bias voltage, or it can be swept. The m-NLP system utilizes the latter, which is the key to its high spatial resolution (Bekkeng 2009). The probes are biased at different levels to obtain the IV-curve in the *electron saturation* region shown in Figure 2.2. The common logarithm of the current in this region will be a straight line as function of the applied voltage, and hence only two probes at different voltages are necessary to obtain the IV-characteristics. Having the electron saturation region characterized makes it possible to calculate both the electron density and the floating potential (Bekkeng et al. 2013).

The problem with the fixed bias technique is that the probes must be operated in the electron saturation region. Since the probes are biased with respect to the floating potential of the frame, the voltage of the probe with respect to the plasma potential will decrease if the floating potential of the frame decreases. At the point where the bias voltage of the probe is no longer greater than the difference between the plasma potential and the frame potential, erroneous measurements will be made. It is therefore essential to control the floating potential of CubeSTAR to ensure confident measurements of the electron density.

2.3 Floating Potential of CubeSTAR

The electron density in the expected orbit of CubeSTAR is in the range of 10^9 m^{-3} to 10^{12} m^{-3}. In the lowest electron density regions, photoemission of electrons will secure a stable and small negative potential on CubeSTAR in full sunlight. However, in reduced solar radiation regions, such as in eclipse, the potential will be driven to more negative values. Electron collects of the biased Langmuir probes contribute to further lowering the potential. A calculation of the expected floating potential of CubeSTAR in LEO is given in Appendix A. The details, which are omitted here, lead to the conclusion that an emitted electron gun current between 0.5 μA and 5 μA can control, and lock, the floating potential of CubeSTAR to a small negative value above -0.5 V, keeping the Langmuir probes in the electron saturation region.

2.4 Spacecraft Charging Mitigation Methods

The floating potential of CubeSTAR can be kept, as described in the previous section, at a comfortable level by ejecting an electron beam into the surrounding plasma. If the emitted beam exceeds the other current contributions in Eq. 2.5, it controls the spacecraft potential. Emitting a charged particle beam is characterized as being an active spacecraft charging mitigation method, and is just one of several other methods known today. A nice overview on spacecraft charging mitigation methods is given by Lai (2003), in which some of the information is being retold here.

The term active means that the level of spacecraft charging mitigation is controlled by commands. In contrast, a passive method does not need to be controlled. Spacecraft charging mitigation methods can further be divided into those that only mitigate frame charging, and those that can mitigate dielectric surface charging as well. Figure 2.3 illustrates this principle. In the figure to the left, conductive ground charges are being emitted by thermionic emission from a hot filament. This is characterized as an active method. A sharp spike, shown to the right, will emit conductive ground charges through field emission due to the high electrical field at the tip. This is characterized as a passive method. Since charges in dielectrics do not readily move, these methods can only mitigate charges from the frame. Emitting a beam of low energy ions and electrons, on the other hand, can mitigate dielectric surface charges in addition to frame charges. The positively charged ions will return to the spacecraft and neutralize charges on the surface regardless of the conductivity. The methods which only mitigate frame charging requires that as much of the satellite's surface is at least partially conductive, otherwise differential charging may ensue and it would be difficult to control the spacecraft floating potential.

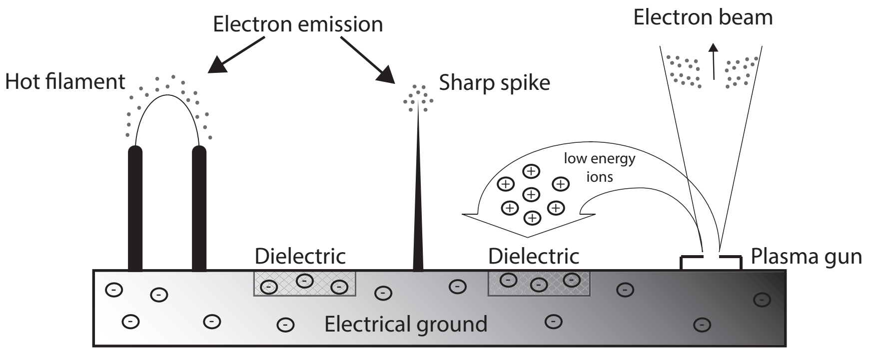

Figure 2.3: Shows three different spacecraft charging mitigation methods of negatively charged spacecrafts. The hot filament is an active method while the sharp spike is a passive method. Both can only mitigate negative charges from the frame. The plasma gun mitigates both dielectric charges, when the ions deposit on the surfaces, and conductive ground charges. Adapted from Lai (2003).

2.4.1 Proposed Method for CubeSTAR

The proposed spacecraft charging mitigation method for CubeSTAR is to emit a beam of electrons using an electron gun. An active approach is taken to have better control of the spacecraft potential. The hot filament method could have been used, but space charge effects tend to limit the emitted current from this method according to Lai (2003). In addition, the kinetic energy of the emitted electrons is low, and there are a greater risk of influencing the m-NLP measurements. Other mitigation methods such as the plasma gun will be too complicated and power consuming for the CubeSTAR project.

The electron gun is, as already mentioned, only capable of mitigating frame charging. It is therefore important to render as much of the satellite's surface conductive and tie it to the frame This will ensure a high degree of electrostatic cleanliness. It is seen in Figure 2.4 that the solar cells are covering most of the satellite's surface. Rendering the surfaces of the solar cells conductive is therefore a key point. To improve the conductivity coverage ratio, it is further recommended to leave a ground layer on the top electric for the PCBs which will be covering the unused space on the PCBs. The frame itself is made of aluminium, so it will be conductive. Hoever, CubeSTAR is built in accordance to the CubeSat Design Specification and must follow requirement 2.2.20 found in CDS rev.12. This requirement states that: "the CubeSat rails and standoff, which contact the P-POD rails and adjacent CubeSat standoff, shall be hard anodized aluminium...". It is recommended to investigate the possibilities of coating the hard anodized aluminium with a partially conductive material to render the surface of the frame conductive.

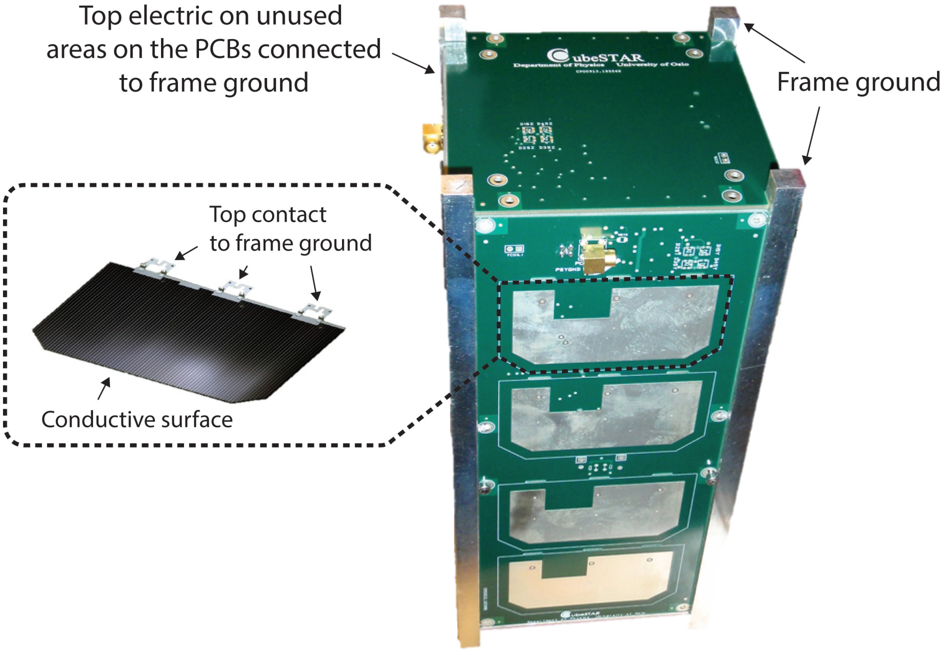

Figure 2.4: Shows the proposed method for rendering the surface of CubeSTAR conductive. Here shown with a preliminary engineering model of CubeSTAR. Rendering the surface of the solar cells conductive is a key point to achieving a high conductivity coverage ratio on the satellite.

Chapter 3

Transparent Conductive Coating

This chapter starts by presenting the PV cells chosen for CubeSTAR, followed by an introduction to the working principles of photovoltaic cells. Different transparent conductive coatings suitable for rendering the photovoltaic cells' surfaces conductive are then presented, together with the properties it should possess. An experimental investigation of one such coating deposited at MiNaLab is then presented.

3.1 Background and Theory

The photovoltaic cells which will be used on the CubeSTAR mission is the Ultra Triple Junction (UTJ) cell from Spectrolab. Spectrolab specialises in high-efficiency multijunction solar cells for spacecraft applications, and has many years of experience in the field. The UTJ PV-cell has an efficiency of 28.3 % (28°C, AM0) and an area of 26.62 cm^2. The solar cells used in the experiments presented later are the Improved Triple Junction (ITJ) solar cells from the same manufacturer. It is fairly similar to the UTJ cell, but has amongst others, a slightly lower efficiency. The ITJ solar cell is shown in Figure 3.1. The solar cell has an n/p design, which means that the electron flow is from the top contact to the bottom contact as discussed later.

Figure 3.1: Shows an image of the ITJ solar cell from Spectrolab.

A solar cell is essentially just a photodiode operated in its photovoltaic mode. A photodiode is furthermore simply a *p-n* junction which is built so that it can be exposed to light (Bogart et al. 2004). A p-n junction can be made from doping one side of a highly pure semiconductor material, like silicon, with atoms from the group 3A in the periodic table (p-doping), and the other side with atoms from the group 5A (n-doping). The p-doped side will have an abundance of holes, or lack of electrons, and the n-doped side will have an abundance of free electrons compared to the pure silicon. When these two regions come in contact with each other, a region called the depletion region is formed because electrons from the n-side recombine with holes from the p-side due to diffusion. This depletion region has no free charges and creates an electric field between the two regions due to the electrically charged ions. When light hits the solar cells, electrons are excited from the valence band to the conduction band if the energy, E, of the photon hitting it is higher than the bandgap, E_g. This situation is illustrated in Figure 3.2a. The electrons are pushed to the n-side, while the holes are pushed to the p-side due to the electric field of the depletion region. The pn-junction is shown in Figure 3.2b.

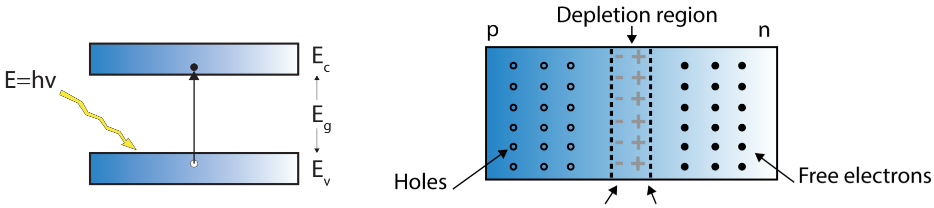

(a)

(b)

Figure 3.2: If a photon, with energy $E > E_g$, hits an electron in the valence band, the electron will be excited to the conduction band as seen in (a). The excited electrons flow to the p-side and the holes flow to the n-side in the pn-junction illustrated in (b). This separation of charges can constitute a current if an external path between the two regions is made.

Light from the Sun consists of electromagnetic waves with different frequencies, from UV light to infrared light. Since the atmosphere absorb some of the frequencies the solar irradiance on the Earth's surfaces is different from outside the atmosphere. The solar irradiance outside the atmosphere is defined by air mass zero (AM0), while the irradiance at the Earth's surface with the sun directly above is defined by AM1.0. The spectral irradiance is shown in Figure 3.3. It is seen that the spectrum of the sun is similar to the spectrum of a black body at roughly 5800 K, and the irradiance is highest at around 500 nm. The bandgap of PV cells are chosen to match this spectrum. The photons with higher energy than the bandgap convert some of the energy to electricity, while the rest is being thermalized (da Rosa

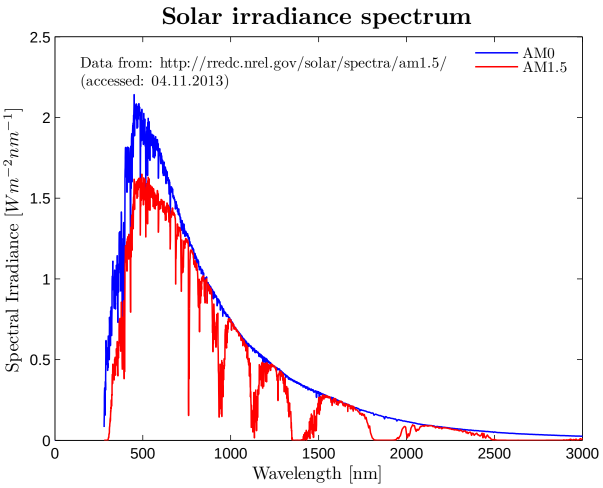

Figure 3.3: Shows the solar irradiance spectrum at the Earth's surface (AM1.5) and on top of the atmosphere (AM0).

2009). Photons with less energy than the bandgap does not interact with the material and the energy is not converted to electricity.

Multijunction solar cells are made to utilize the energy in the photons better by using p-n junctions with different bandgaps. The ITJ PV cell from Spectrolab consists of Germanium (Ge), Gallium Arsenide (GaAs) and Gallium Indium Phosphide ($GaInP_2$) as shown in Figure 3.4a. $GaInP_2$ has the largest bandgap and is therefore the top cell. This diode will absorb photons with energy greater than the bandgap of the cell, and it is transparent to those with less energy. The middle cell consists of GaAs and has lower bandgap than the top cell. This cell absorb photons that did not have enough energy for the top cell. The bottom cell, Ge, has the lowest bandgap and absorbs the lowest energy photons. As seen in Figure 3.4b this arrangement can convert photons with wavelengths up to 1800 nm, and with higher efficiency than with just a bare Ge cell.

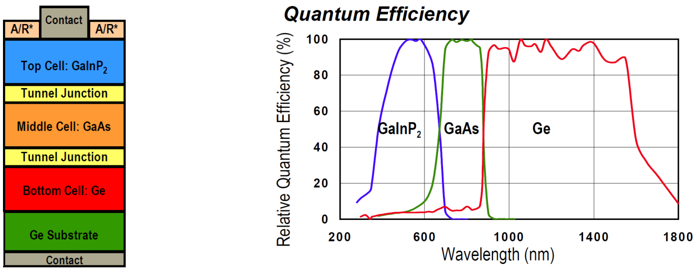

(a) (b)

Figure 3.4: (a) shows the design of the ITJ solar cell (Spectrolab a) while (b) shows the spectral response of a similar PV cell (Spectrolab b).

3.1.1 Some Desirable Properties of the Coating

There are many parameters that characterizes a PV cell, with the most important being the efficiency of the cell. The efficiency is the percentage amount of incoming solar energy that is being transformed to electrical energy. The transparent conductive coating which will cover the surface of the solar cell should be chosen such that the efficiency of the cell does not degrade too much, and it should have sufficient conductance. The coating should preserve its properties to a sufficient amount during the lifetime of CubeSTAR. The following paragraphs discuss some of the properties the coating should possess.

Stability in the low earth polar orbit The properties of the coating should not be degenerated by the low earth polar orbit CubeSTAR is planned to have. The environment associated this orbit possesses several threats to the coating. UV radiation and chemical interactions with atomic oxygen, molecular contamination due to outgassing and physical sputtering due to impact with neutral molecules are some of the hazards described by Tribble (2003). Thermal cycling is also a concern in LEO as the satellites orbital period is small.

Transmission properties The coating should have as high transmission as possible in the useful range of the photovoltaic cell, which is between 300 to 1800 nm. The solar irradiance spectrum for AM0 should also be taken into account when rating the transmission properties of the coating. In order to minimize the optical losses an anti-reflective (AR) coating is usually found on the top electrode of a solar cell. The AR coating is designed by choosing the refractive index and thickness of the coating in order to produce destructive interference of the reflected rays. The coating can further be improved by texturing the surface (Solanki 2009). To produce destructive interference for light at normal incidence the thickness, d, of the layer must be 1/4 of the wavelength in the new medium, λ/n, with refractive index n.

$$d = \frac{\frac{\lambda}{n}}{4} * m, m = 1, 3, 5, .. \tag{3.1}$$

The thickness of the layer should be chosen to produce an anti-reflective effect such that reflection is minimized. The material chosen as transparent conductive coating should not interfere with the, if any, surface texture of the solar cell.

Thermal properties The efficiency of a solar cell decreases with increased operating temperature. Infrared reflecting coatings is sometimes applied in order to reject part of the sunlight that would otherwise contribute to heat generation in the solar cell (Yoon et al.). The transparent conductive coating should not contribute to further heat generation.

Conductive properties In order for an electron emitter to be able to control the spacecraft potential, the entire spacecraft surface needs to be conductive (NASA 2011). Conductive coatings are also used on spacecraft surfaces as a way of preventing ESD-issues, and NASA has come with recommended requirements for the conductivity regarding this issue. These requirements are, however, not sufficient enough for space missions where control of the spacecraft potential is important. When this is the case the conductivity of the coating must be such that the maximum potential difference that can occur is below the requirements of the mission. An example is given in Kauder (2005) where a conductive coating is covering a non-conductive substrate and grounded at the edges. The maximum voltage potential occurs at the point furthest from the ground and is given by.

$$\Delta V = \frac{I}{2}R = \frac{Jh^2cos(\theta)}{2}(\frac{\rho}{t}) \tag{3.2}$$

where h is the length of the square covered by conductive coating, J is the incoming current density at angle θ and ρ/t is the sheet resistivity. As an example consider an incoming current of $1.5 \cdot 10^{-5}$ A to a 10 cm^2 surface. If the maximum allowable differential potential is 10 mV, the sheet resistivity of the coating must be less than $1.3 \cdot 10^3 \Omega/\Box$.

Work Function Since CubeSTAR is expected to gain a negative potential due to the high density plasma, a coating with a low work function is desirable. In the sunlight part of the orbit more electrons will be emitted from the satellite due to photo emission when the coating has a low work function.

3.2 Literature

Transparent conductive coatings have been used for many years, in both consumer products like touch-screen mobile phones and solar cells, and in more specialised fields like aerospace applications. Following is a literature study of transparent conductive coatings that were considered applicable to CubeSTAR.

3.2.1 Overview

Gordon gives a nice summary of transparent conductors (TCs) in his article "Criteria for Choosing Transparent Conductors". According to Gordon the best TC is dependent on its application and the production method. Optical and electrical properties of these films are of course important and he thus ranks different TCs after these two properties in one of his tables. Fluorine doped zinc oxide ranks highest, while aluminium doped zinc oxide and indium tin oxide is ranked at third and fourth place respectively. Cadmium stannate comes in at second place. When Gordon ranks the TCs solely after their transparency, fluorine doped zinc oxide and cadmium stannate comes in first. The work function of ITO and ZnO is 4.8 and 4.5 eV respectively, according to Gordon. A more in-depth study of some transparent conductive coatings, which also investigates the coatings ability to withstand the low earth orbit environment not treated in Gordon's article, is now given.

3.2.2 Indium Tin Oxide

Indium Tin Oxide (ITO) is a transparent conductive coating with good conductivity and transparency.. It has been recommended by Purvis et al. (1984) in "Design Guidelines for Assessing and Controlling Spacecraft Charging Effects" and it has been used to provide conductive spacecraft surfaces earlier with success. As an example ITO was used on the Cluster mission by ESA to cover the external surfaces including the solar arrays. The Cluster mission demanded a high degree of electrostatic cleanliness (Credland et al. 1997).

Properties of ITO films have been widely investigated in the past. In an article by Li-Jian Meng and M.P dos Santos properties of ITO films deposited on glass substrates by RF magnetron sputtering were investigated at different sputtering temperatures. The results showed that the film thickness, which were between 625 and 1000 nm, were dependent on the deposition temperature. The experiment showed further that the sheet resistance was lowest at the highest temperatures, and highest at the lowest temperatures. The sheet resistance was between 0.9 and 56 [$\Omega/\Box$]. The transmittance of the films, including the glass substrate on which they were deposited on, is shown in Figure 3.5. It is seen that the transmittance is roughly the same for all the film thickness's in the visible range. However, the transmittance at higher wavelengths decreases rapidly for the films deposited at the highest temperatures.

Even though ITO has been recommended and used earlier on electrostatic clean spacecraft, studies indicate that both transmission and conductivity of ITO degrades when exposed to the LEO environment (Perez-Davis et al. 1994). By adding MgF_2 Perez-Davis et al. achieved both resistance against atomic oxygen and higher transmission, but lower conductivity. Synowicki et al. (1993) investigated the low earth orbit effect on ITO and also compared this to common laboratory simulations. One set of 25 nm thick ITO films were flown on the space shuttle Atlantis on the EOIM III payload and accumulated atomic oxygen over 40 hours exposure in LEO. The results

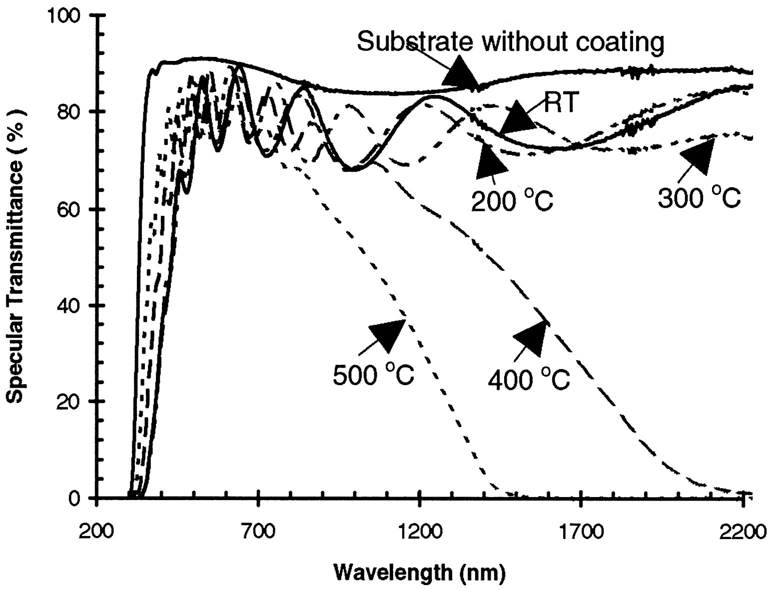

Figure 3.5: Transmittance of the different ITO thin films deposited by RF magnetron sputtering. By Li-jian Meng and M.P dos Santos (1998).

showed that there was an significant change in absorbance below 450 nm.

The effect of LEO exposure to ITO coated solar cells has been investigated in the "Solar Array Materials Passive LDEF Experiment" (SAMPLE). Numerous solar cells were covered by fused silica (SiO_2) coversheets with indium-tin-oxide conductive coatings and exposed to the LEO environment at an orbit of 476 to 332 km with a duration of 69 months. Unfortunately no measurements of the cells current-voltage characteristics were possible. The resistance of the coating increased by ~9 to ~175% (Hill and Rose 1994).

The Materials International Space Station Experiment (MISSE-6A and 6B), is an experiment conducted by NASA whose purpose is to investigate the durability of spacecraft materials in LEO. The materials were attached to the International Space Station in March 2008 and retrieved in September 2009. One of the experiments is the Indium Tin Oxide (ITO) Degradation Experiment, which investigated the change of optical and electrical properties of ITO when exposed to LEO (de Groh et al. 2008). At the time of writing no papers have been found showing the results from this experiment.

3.2.3 Zinc Oxide

Zinc Oxide (ZnO) is a good candidate to ITO as it, according to Lennon et al. (2008), possesses similar electrical and optical properties. In their study, films of AZO from the commercially available target compositions $ZnO:Al_2O_3$ (98:2 wt.%) and $ZnO:Al_2O_3:In$(87.3:2.7:10 wt.%) were deposited by radiofrequency (RF) magnetron sputtering. The purpose of the experiment was to determine the films suitability for spacecraft charging mitigation. Sustainability to the geostationary orbit environment was also investigated through stability tests conducted in laboratories. The results of the experiments showed that the films, ranging from 35 to 55 nm, had a sheet resistance which was greater than 10^4 $\Omega/\square$ for the Al-doped and $\sim 4 \cdot 10^3$ $\Omega/\square$ for the Al:In co-doped samples. A 30 min *ex situ* annealing procedure at 250°C in an N_2 atmosphere improved the electrical properties. The transmission of the films indicated an average transmittance greater than 80 % in the visible range. The resistance of the films after the geostationary orbit environment tests showed negligible change in the electrical properties as well as to the optical properties. The transmittance of the ZnO:Al_2O_3:In and ZnO:Al_2O_3 films deposited on fused quartz before and after the GEO stability testing are shown in Figure 3.6.

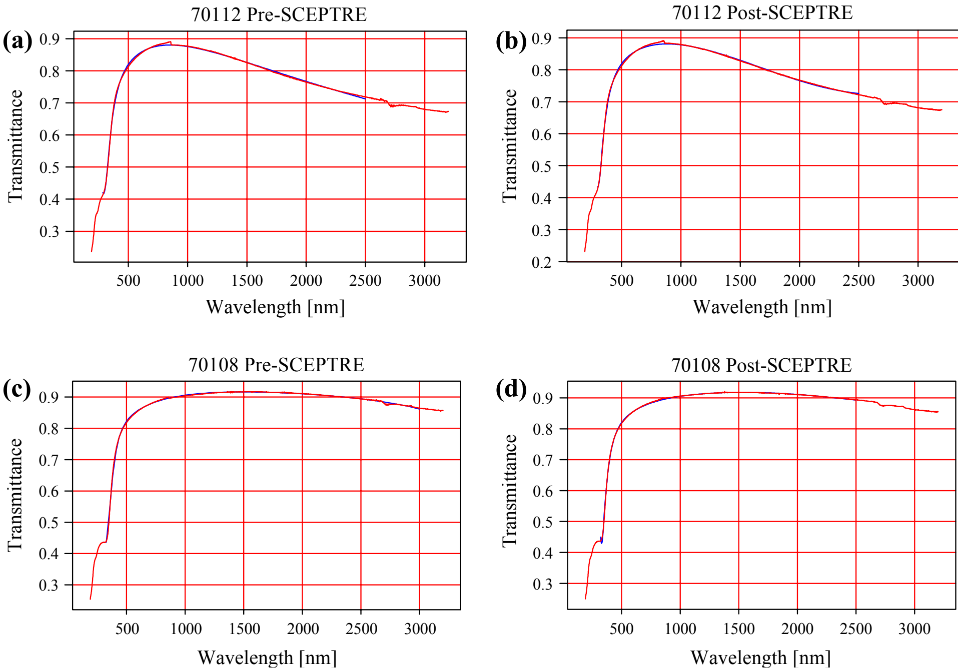

Figure 3.6: Transmittance of ZnO:Al_2O_3:In (a, b) and ZnO:Al_2O_3 (c, d) deposited by RF magnetron sputtering on fused quartz before and after GEO stability testing. By Lennon et al. (2008).

Lennon et al. showed that ZnO can be used as charging mitigation coating in geostationary orbit. However, the effect on low earth orbit environment exposure to the films has not yet been investigated, and they conclude that further investigations is necessary.

3.2.4 Gold

A very thin film in the order of 5-15 nm of gold (Au) was proposed as a transparent conductive coating for CubeSTAR. At this thickness Au becomes transparent to visible light. However, as it is seen in the articles by Lansåker et al. (2011) and Siegel et al. (2011), the resistance of the film rapidly increases as the thickness of the layer exceeds the value where the film becomes transparent. At around 2-3 nm the transparency of the au-thin film is somewhat comparable to that of the ITO film. The resistance is, however, too high.

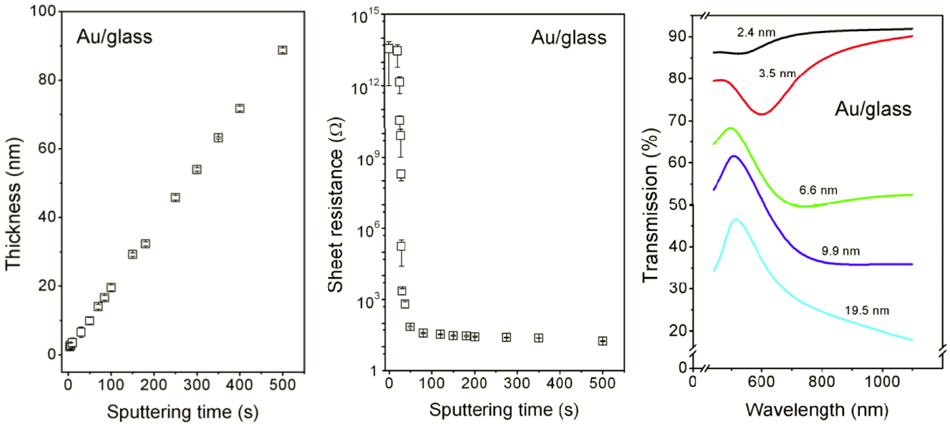

Figure 3.7: Shows transmittance, resistance and thickness of Au films deposited by Siegel et al. (2011). The resistance increases rapidly as the films gets transparent to visible light.

3.3 Experiments

The literature study reviled that Indium Tin Oxide and Zinc Oxide were both promising transparent conductive coatings for CubeSTAR. It was decided, however, that ITO was to be used in the experiments. More about this decision is giving in section 3.4. The experiments presented here were conducted to examine the effect a thin layer of ITO would have on the performance, and especially the efficiency, of the ITJ solar cells from Spectrolab. The resistivity was characterised to ensure it was sufficiently low for the CubeSTAR mission. The surface analysis of the solar cell was made by Anette Eleonora Gunnæs at the Department of Chemistry. Deposition and characterization of the ITO films were made by Esben Lund at the Department of Physics.

3.3.1 Surface Analysis

To gain more knowledge about the surface topology and material composition of the ITJ solar cell, both Scanning Electron Microscopy (SEM) and Energy Dispersive Spectrometry (EDS) analysis were performed on a B-graded sample. It was of interest to find out if the surface was textured to increase the efficiency. If it indeed had a textured surface, the thickness of the ITO layer should be thin enough to not alter the textures. The analysis were performed with a Hitachi TM3000 tabletop microscope.

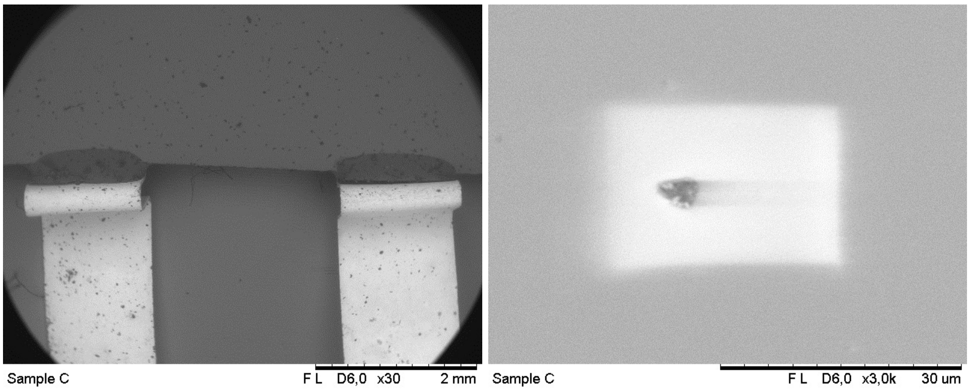

(a) (b)

Figure 3.8: Shows images from the SEM analysis: (a) shows a low magnification image of the solar cell near one of the terminal on the top conctact, while (b) shows a high magnification image on the solar cell surface.

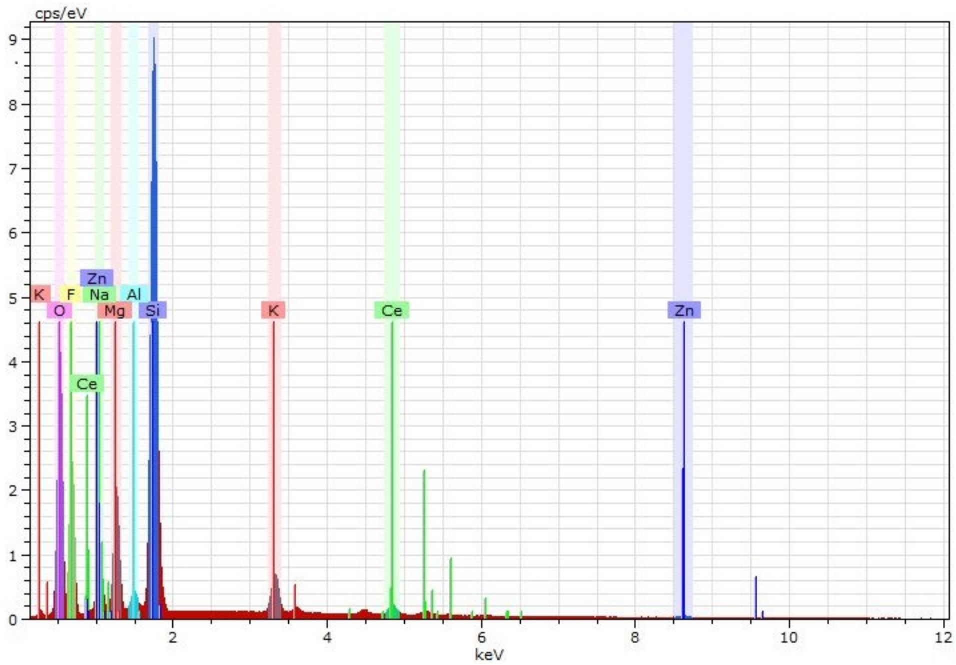

Figure 3.9: Shows the graph produced by EDS analysis of the ITJ solar cell.

As seen in Figure 3.8 the SEM analysis showed a very smooth surface with no apparent structures. The front contacts shown in Figure 3.4a could not be located either and the EDS analysis, shown in Figure 3.9, revealed materials common to those used in glass such as silicon (Si), oxygen (O) and sodium (Na).

3.3.2 ITO on Glass Substrates

Indium Tin Oxide was sputtered on four glass substrates using radiofrequency (RF) magnetron sputtering. The purpose was to investigating the effect of different deposition temperatures on transmission, conductivity and thickness. The glass substrates were covered by aluminium foil in one corner so that the thickness of the deposited film could be measured later on. The parameters used for the sputtering process are given in table 3.1. The distance between the target and the substrates were approximately 10 cm.

The sheet resistivity of the deposited films was measured with a four point probing-technique. Each DUT was measured five times at different locations on the substrate to obtain an average resistivity. The current was set to 100 μA, and the sheet resistivity was read from a Jandel RM3-AR with three digits, omitting the decimal numbers. To obtain the resistance of an object coated with the film one can use the equation

Table 3.1: Sputtering parameters used for the different DUTs

DUT	**RF Power** (W)	**Ar** (sccm)	**Base pressure** (10^{-6}T)	**Pressure** (mT)	**Temperature** (°C)	**Time** (min)
ITO1	150	15	0.5	4.2	RT†	15
ITO2	150	15	7.3	4.3	100	15
ITO3	150	15	6.6	4.3	200	15
ITO4	150	15	0.4	4.3	300	15

† RT = room temperature

$$R = \frac{\rho}{t}\frac{L}{W} = R_s\frac{L}{W} \tag{3.3}$$

where R is resistance, R_s is sheet resistance, ρ is resistivity, L is the length of the film and W the width of the film. The thickness of the layer was measured with a Dektak Surface Profilometer with reference to the covered corner on the substrate. The resistivity of the film were then calculated based upon the sheet resistivity and thickness measurements using the relationship

$$\rho = R_s t \tag{3.4}$$

Unfortunately there was a problem with the computer connected to the Dektak and only one film thickness was characterised. However, since the surfaces analysis did not show any textures, and the film thickness therefore was not important any more, the characterization of the thickness was not resumed. The measured sheet resistance and thickness is shown together with the calculated resistivity of the films in Table 3.2.

Table 3.2: Results from the resistivity and thickness measurements.

DUT	**Sheet resistance, R_s** [Ω/□]	**Thickness, t** [nm]	**Resistivity, ρ** [Ω-cm]
ITO1	226 ($\sigma = 2.6$)	220	$4.97\cdot10^{-3}$
ITO2	120 ($\sigma = 3.8$)	-	-
ITO3	145 ($\sigma = 3.1$)	-	-
ITO4	197 ($\sigma = 1.3$)	-	-

The transmittance of the ITO films were measured at different wavelengths with a UV-VIS-NIR Spectrophotometer using a bare glass substrate as reference. The DUTs were measured one at the time, and the results are shown in Figure 3.10.

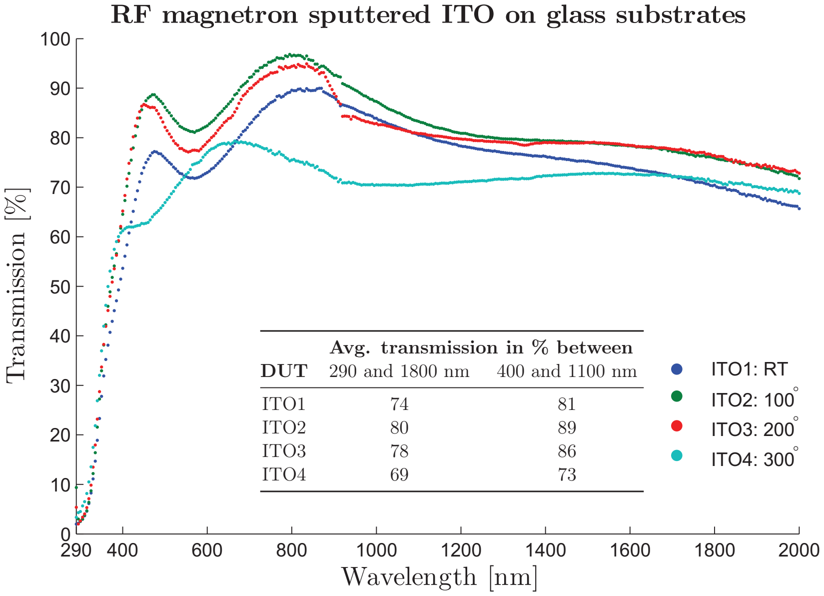

DUT	Avg. transmission in % between 290 and 1800 nm	400 and 1100 nm
ITO1	74	81
ITO2	80	89
ITO3	78	86
ITO4	69	73

Figure 3.10: Transmission of the different DUTs using a glass substrate as reference. The spectrophotometry instrument induced a lot of noise around 900 nm which is filtered out in this graph.

3.3.3 ITO on ITJ PV cell

A B-graded sample of an ITJ PV cell was characterised with respect to its IV-characteristics. The purpose was to characterise the cell before and after ITO deposition, and compare the results. Prior to deposition, the PV cell was placed inside a solar simulator and its IV characteristics were taken. The light source were set to output 1000 [W] with an AM1.5 filter installed. The results are shown in Figure 3.11.

The PV cell was then sputtered with ITO using the same parameters as for the DUT ITO2, with a sputtering temperature of 100°C. Unfortunately, the coating did not stick to the solar cell. The reason for this is thought to be that it was not properly cleaned before deposition.

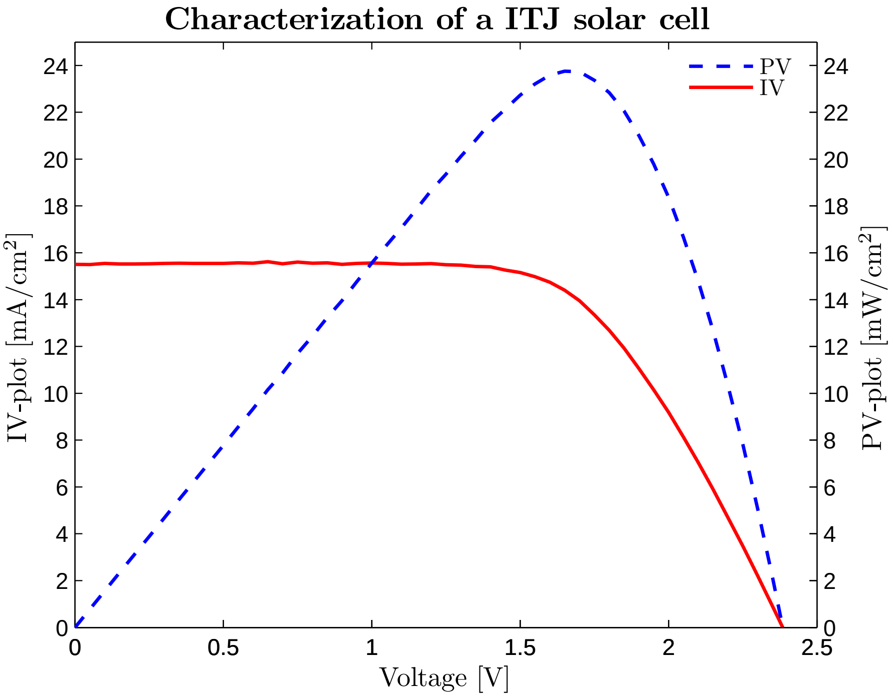

Figure 3.11: Characterization of a ITJ solar cell before ITO deposition.

3.4 Discussion

According to the article by Gordon it is clear that ZnO:F is the best coating for CubeSTAR of the discussed coatings. It has the highest transparency, the lowest work function and a sufficiently low resistivity. However, Zinc oxide and its various forms including fluorine doped zinc oxide and aluminium doped zinc oxide, have not been extensively used in spacecraft applications. It is therefore not known how they will respond to the environment associated with the low earth orbit. Studies indicate, however, that aluminium doped zinc oxide at least can withstand simulations of the geostationary earth orbit. If degradation of the coating is not of a concern for the CubeSTAR mission, since its lifetime is short, zinc oxide will be a better option. Indium Tin Oxide on the other hand is a more reliable choice for CubeSTAR, as it has been widely tested and used in spacecraft applications earlier with success. It is worth noting that ZnO possesses piezoelectric properties which is not found in ITO. Unfortunately, there are still some work needed to be done with the characterization of the transparent conductive coating. The LabVIEW program used for solar cell characterization at MiNaLab was erased prior to the second attempt of ITO deposition. This meant that a new program had to be created before characterization could be resumed. As a result, the work with the transparent conductive coatings was put on hold, as the development of the electron gun had a higher priority. However, as it turns out, there might be a solution except for coating the solar cells in-house.

3.4.1 Spectrolabs CIC Assembly

Spectrolab offers what they call a Solar Cell + Interconnects + Coverglass (CIC) assembly. According to the datasheet from Spectrolab, the ITJ PV cell does not have this option. However, it is lead to believe that the sample which was studied in this experiment still was a CIC assembly, as the experiments showed materials common to glass in combination with a smooth surface. The datasheet for the UTJ PV cell specifies that CIC assembly is available for this particular cell, with various coatings.

A mail correspondence with Spectrolab revealed that Spectrolab buys a lot of their coverglasses from Qioptiq[1]. Information available on Qioptiq's website states further that their coverglass is cerium doped, a material found in the surface analysis presented in Section 3.3.1. This supports the hypothesis that the solar cell used in the experiment was a CIC assembly. The datasheet for the coatings produced by Qioptiq, is given in Appendix E[2]. Of particular interest is the coverglasses they manufacture with conductive surfaces. Two front surface resistances are available: <5 kΩ and $<$ 10MΩ. The latter option has slightly higher transparency than the first option, but they are both very close in transparency to the coverglass without conductive surfaces. It is recommended to investigate further possibilities to obtain the ITJ solar cell with a conductive surface from Spectrolab, instead of deposit the coating in-house. The choice of resistance depends on the transmittance loss that is acceptable from the electrical power system. Higher electrical conductivity yields a more electrostatic clean spacecraft.

---

[1] http://www.qioptiq.com/

[2] Accessed September 2012

Chapter 4

Theory and Design of Electron Guns

This chapter will focus on the theory and design guidelines thought useful for a small electron gun capable of emitting a current in the μA-range. As the reader of this thesis probably will not be from the particle accelerator community, and as it is not necessary for understanding the rest of this thesis, the depth of the theory will be kept to a minimum whereas basic theory will be explained.

4.1 Introduction

An electron gun, also commonly called an electron emitter, is a device which forms and accelerates a beam of electrons, which in turn is ejected from the gun. To accomplish this there are at least two features that need to be in place, viz., (1) a source of electrons and (2) electrodes to extract and accelerate the electrons towards the exit of the gun. In addition it may be desirable to collimate and focus the electron beam. This could be achieved with electrostatic or magnetic lenses, in combination with the extraction stage or later in the electron gun. Figure 4.1 shows how an electron gun might look like with all the elements mentioned above present. The electrons are extracted and accelerated from the cathode by a positively biased electrode called the anode. A fraction of the electron beam gets through an aperture in the anode and forms the final electron beam which is then focused by a second set of electrodes. The theory on how this is done will be explained more thoroughly in the next sections. In this chapter the books by Chattopadhyay and Rakshit (2006), Bakish (1962), Pierce (1949) and Bijl (1920) have been used as source of information unless otherwise stated.

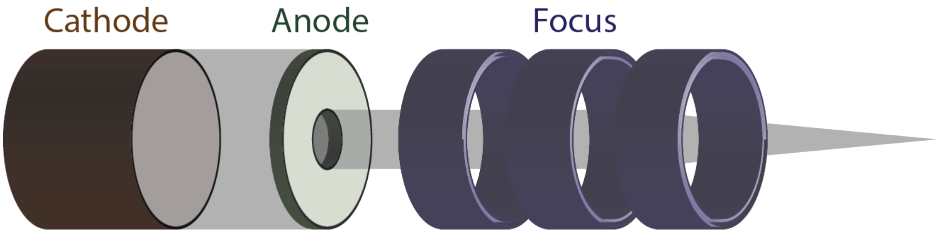

Figure 4.1: Shows a typical electron gun configuration with a cathode, which serves as the electron source, an anode to extract and accelerate the electrons and additional electrodes which focus the beam. The gray shadow illustrates the electron beam.

4.2 The Cathode

The cathode provides the source of electrons in an electron gun. This is achieved by electron emission from a solid metal[1], and the metal from which the electron emission occurs is referred to as the cathode. In a metal, the otherwise free-to-move conduction electrons are prevented from leaving the surface due to the attractive forces from the positively charged ions they try to leave behind. For electron emission to occur the electrons need to gain enough kinetic energy to overcome this surface potential barrier, which at absolute zero is denoted as the work function of the material. Energy can be provided externally in four different ways giving rise to four different modes of emission from a metal: (1) thermionic emission, (2) field emission, (3) photoelectric emission and (4) secondary emission. The focus in this thesis will be on thermionic emission, as it is the most feasible technique for the electron gun due to the limited project period.

4.2.1 Thermionic Emission

In thermionic emission the electrons gain enough kinetic energy to overcome the surface energy barrier through heating of the cathode. The current density of thermionic emission can be found through the work done by Richardson (1929) for which he was awarded the Nobel Prize in Physics in 1928:

$$J_0 = AT^2 e^{(-\frac{W}{k_b T})} \tag{4.1}$$

where A is a constant, T is the temperature, W is the work function and k_b is Boltzmann's constant. This is known as the Richardson's equation or Richardson-Duschman equation. It is seen from the equation that the current density is very sensitive to changes in temperature and that the ideal

---

[1] It should be noted that the cathode does not have to be made of metal, as is the case for the lanthanum hexaboride cathode which is a refractory ceramic.

cathode should have a low work function. To allow a high emission rate the cathode material must not evaporate considerately at high temperatures or be contaminated by residual gases.

The cathode can be either directly heated, usually in the form of a filament, or indirectly heated. In a directly heated cathode a current is passed through the cathode which in turn starts to emit electrons when the temperature is sufficiently high. In an indirectly heated cathode the cathode is placed in the vicinity of a heating source, for instance a current-carrying wire like the filament. This is illustrated in Figure 4.2. There are both pros and cons with the directly heated cathode compared to the indirectly heated as discussed by Chattopadhyay and Rakshit (2006):

pros:

- The power needed to heat the cathode is less, and the energy dissipated in the cathode is fully utilized.
- The desired cathode temperature is attained in a short time.

cons:

- The cathode is not an equipotential surface and the voltage drop across the filament may disrupt the electric field.
- Thermal expansion may cause the filament to touch a nearby electrode.
- The filament becomes mechanically weak at the operating temperature and should be supported by insulating supports.

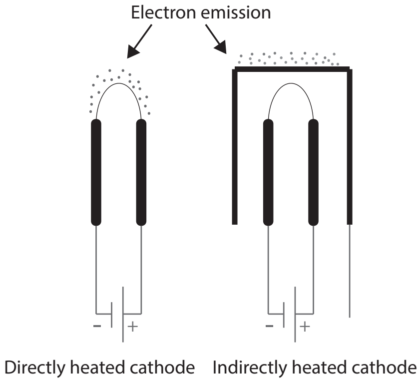

Figure 4.2: Shows emission from a directly heated cathode (left) and an indirectly heated cathode (right). The electric potential is independent of the heating source, and emission takes place at an equipotential surface in the indirectly heated cathode. The energy dissipated in the directly heated cathode is fully utilized.

Temperature Coefficient of Resistance

The temperature of a resistor can be estimated by exploiting the fact that both the resistivity and the dimensions of the resistor are functions of temperature. The change in resistivity, ρ, the length l and the cross-sectional area, A, will affect the overall resistance in the following term:

$$R = \rho \frac{l}{A} \tag{4.2}$$

The resistance of a thermal resistor is related to the temperature with the relationship:

$$R_T = R_0(1 + \alpha_R(T - T_0)) \tag{4.3}$$

where R_T and R_0 are the resistances of temperature T and T_0 respectively, while α is called the temperature coefficient of resistance (TCR). The temperature of a filament can thus be estimated by knowing the cold and hot resistance of the filament. This linear relationship is only valid over a moderate temperature range, and non-linear terms may be needed for higher ranges. The TCR of tungsten is 4500 (ppm). Liu (2006)

Both the directly heated cathode and the indirectly heated cathode come in different materials. The three main groups of cathodes are the refractory metal cathodes, the oxide coated cathodes and the dispenser cathodes. Choosing the correct cathode for a certain application depends upon the application. The general design requirements for a cathode, however, is that it:

- can supply enough emission current over the entire lifetime.
- has small power input (emission current per watt of heater power), which implies low work function, good thermal efficiency and small size.
- is able to operate in the working environment.
- is simple to construct.

Refractory Metal Cathodes

The refractory metal thermionic emitters have high work function, somewhere in between 4 and 5 eV, which means they have to burn at high temperatures for significant electron emission to occur. The power efficiency of these cathodes is low due to the fact that the main contributor to power loss in cathodes usually is radiation. These cathodes are usually a filament of tungsten, with materials such as thorium sometimes being added to lower the work function, or tantalum discs.

Oxide Coated Cathodes

The oxide coated cathodes consist of either a directly or indirectly heated metallic base supporting a coating of metal oxides. The cathodes must be activated under vacuum by a process prior to use, and once activated it should not be exposed to air. The oxide coated cathodes have a lower work function than the refractory metal cathodes yielding a higher power efficiency. The Richardson's emission equation for metals is also valid for oxide coated cathodes. (Herrmann and Wagener 1951)

Dispenser Cathodes

The modern dispenser cathodes consist of a refractory metal interspersed with an emitting material. The dispensed material, for instance barium, diffuses to the surface and provides a low work function surface. Cronin (1981)

4.3 The Anode

The most basic electron gun configuration consists of a cathode and an apertured anode, just like the two first stages shown in Figure 4.1. When omitting the aperture, this configuration is identical to the *thermionic diode* or the *vacuum tube*. Evidently, there is a lot of knowledge gainable through studying the thermionic diode which later on can be applied to the electron gun design process. As a result this section will begin by treating a simplified and ideal model of the thermionic diode, thus providing the reader with basic knowledge of the aforementioned electron gun.

The simplified and ideal thermionic diode is shown in Figure 4.3 and incorporates the following properties; The cathode and the anode are both plane and parallel, equipotential surfaces of infinite dimensions with respect to the distance, d, between the two electrodes. The cathode can be raised to a temperature, T, at which electrons are being emitted according to Richardson's equation. The emitted electrons are simply oozing out of the cathode, thus ignoring the initial speed they might have when leaving the surface. A known, controllable and constant potential difference, V_a, is applied between the two electrodes which draws the electrons towards the positively biased anode. The diode is situated in a vacuum environment with no residual gasses present. As it will be seen the current in such a diode is limited by something similar to resistance, and does not increase rapidly with voltage. It will be explained next that the current is limited by two factors and that the diode can operate in two different regions giving the IV-characteristics shown in Figure 4.4b and 4.4c.

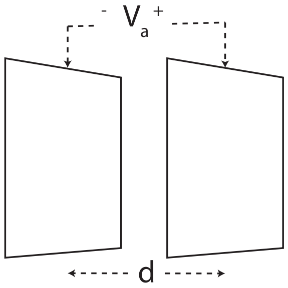

Figure 4.3: Shows the configuration of the ideal and simplified thermionic diode

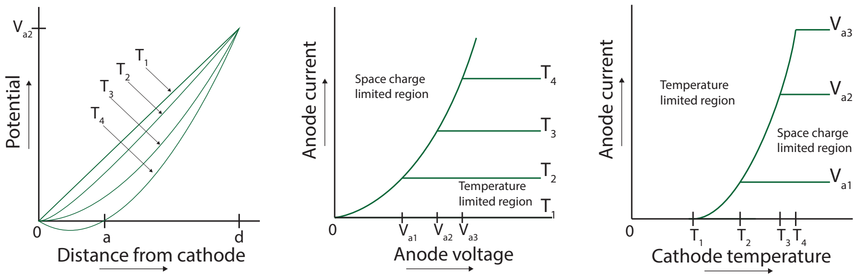

(a) (b) (c)

Figure 4.4: Figure (a) shows how the potential distribution is affected by the space charge in the interelectrode space. Figure (b) shows that the anode current varies as the three-halves power of the anode voltage, with fixed cathode temperature, until the temperature is not high enough and the current levels off. Figure (c) shows that the anode current follows Richardson's equation, with fixed anode voltage, until the anode voltage is not high enough and the current levels off. Adapted from Chattopadhyay and Rakshit (2006).

4.3.1 The Temperature Limited Region

In the temperature limited region the potential difference between the cathode and anode is raised in such an extent that all the electrons are drawn to, and collected by, the anode as fast as they are being emitted by the cathode. The anode current is solely limited by the emission rate, which for a thermionic diode is described by the Richardson's equation. This is the situation described in Figure 4.4b and 4.4c by the temperature T_2 together with an anode voltage greater than V_{a1}. The same yields for T_3 and V_{a2} and T_4 and V_{a3}. At T_1 the electron emission is negligible and the resultant anode current is therefore also negligible, as seen in Figure 4.4b and 4.4c. Increasing the voltage will not produce a higher current as there is no free electrons which can constitute the current. The electric field between the anode and the cathode is uniform and determined by the applied voltage, as indicated by the straight line in Figure 4.4a.

At the higher temperature, T_2, some electrons are being emitted by the cathode and the applied voltage accelerates the electrons towards the anode giving rise to an anode current. As seen in Figure 4.4b the applied voltage needs to be higher than V_{a1} for the diode to be in the temperature limited region. Increasing the voltage beyond V_{a1} will not results in a higher current[2] and the saturation current is reached for the temperature T_2. The volume between the electrodes, in which the electrons are being accelerated, are now filled with electrically charged particles. The charge density varies with the distance of course, as the current density must be constant whereas the speed of the electrons increases due to the acceleration of the electrical field between the electrodes. Since the electrons, that are being accumulated between the electrodes, carry a negative charge the volume also acquires a negative charge. The net electrical field produced by the particles in the region is called the *space charge.* As seen in Figure 4.4a the space charge will to some extent depress the potential in the interelectrode space, and the potential distribution will be slightly curved instead of a straight line.

4.3.2 The Space Charge Limited Region

In the space charge limited region, either the temperature of the cathode is increased, or the applied voltage decreased, in such a way that the amount of emitted electrons exceeds the amount of collected electrons at the anode. Both actions result in an accumulation of electrons in the interelectrode space. To continue the reasoning from the previous subsection, further increasing the temperature from T_2, with the applied voltage being V_{a2}, leads to higher and higher anode currents. As a result, the potential distribution-curve in Figure 4.4a will bend more and more as the space charge also increases. There comes a point where the slope of the potential distribution-curve, and thus the electrical field, is zero at the cathode. This is the situation described by the temperature T_3 in Figure 4.4a. At this point the emission rate equals that of the collection rate and the current goes from being temperature limited to space charge limited. Increasing the temperature of the cathode will not result in a higher anode current because the electrical field near the cathode is zero and the emitted electrons are therefore not accelerated towards the anode. This is illustrated in Figure 4.4c. The relationship between the space charge limited current and the anode voltage was first discovered by Child (1911):

$$J = \frac{4\epsilon_0}{9}\sqrt{\frac{2e}{m_e}}\frac{V_a^{3/2}}{d^2} \tag{4.4}$$

where J is current density, V_a is the applied voltage, d is the distance between the anode and the cathode, m_e is the mass of an electron and ϵ_0

---

[2] Strictly speaking, a higher voltage and hence stronger electric field would result in a slight increase in current due to the Schottky effect.

is the permittivity of free space. This is known as *Child's law* or *Child-Langmuir law* as Langmuir (1913) also investigated this phenomena. It is seen from the equation that the space charge limited current varies directly as the three-halves power of the anode voltage, V_a, and inversely as the square of the distance, d.

4.3.3 Deviations from the Ideal Diode

In practical applications there are no such thing as an ideal diode. This thesis will not go in further details on this topic, other than briefly explaining the effect initial velocity of the emitted electrons has on the characteristics.

Since the velocity of the emitted electrons follows the *Maxwell's distribution law*[3], some of the electrons will have more kinetic energy than necessary for escaping the surface. It therefore follows that further increasing the cathode temperature from T_2 in Figure 4.4, with the applied voltage still being V_{a2}, would increase the anode current. This increased current and space charge would establish a negative electric field near the cathode, and only those electrons with high enough initial speed will overcome the retarding field in the proximity of the cathode as seen in Figure 4.4a.

4.4 Motion of Charged Particles

The Lorentz force governs the force which is exerted on a point charge q in an electromagnetic field. The Lorentz force is given by:

$$\vec{F} = q(\vec{E} + \vec{v} \times \vec{B}) \tag{4.5}$$

where $\vec{v}$ is the velocity of the point charge, $\vec{E}$ is the electric field and $\vec{B}$ is the magnetic field. In pure electrostatic fields where the magnetic field is zero ($\vec{B} = 0$), the Lorentz force can be expressed as:

$$\vec{F} = q\vec{E} \tag{4.6}$$

The motion of a particle in the described field is determined by Newton's equation:

$$\frac{d\vec{P}}{dt} = \vec{F} \tag{4.7}$$

where $\vec{P}$ is the mechanical momentum of the particle. Only low kinetic energy particles is treated in this thesis and the momentum can be expressed using the non-relativistic relationship

$$\vec{P} = m\vec{v} \tag{4.8}$$

---

[3] More precisely the Fermi-Dirac distribution (Kittel 2005)

The equation of motion thus becomes

$$m\frac{d\vec{v}}{dt} = q\vec{E} \tag{4.9}$$

In an electrostatic field, where the electric field does not vary with time, the gradient of the scalar potential can be used to express the electric field

$$\vec{E} = -\nabla V \quad or \quad V = -\int \vec{E} \cdot d\vec{l} \tag{4.10}$$

The equation of motion then takes the form

$$m\frac{d\vec{v}}{dt} = -q \cdot \nabla V \tag{4.11}$$

Having these formulas in mind one can immediately get an understanding of a particle's trajectory through an electrostatic field. A common way to illustrate electrostatic fields is by an equipotential contour plot. A contour plot is shown in Figure 4.5 together with the direction and magnitude of the electrical field illustrated by arrows. Since the charge of an electron is -*e*, with e being the elementary charge with value $1.6 \cdot 10^{-19}C$, the Lorentz force vector will be pointing in the opposite way as the electric field, and the particle will accelerate in that direction. An electron moving in the field shown in Figure 4.5 will be accelerated towards the top electrode.

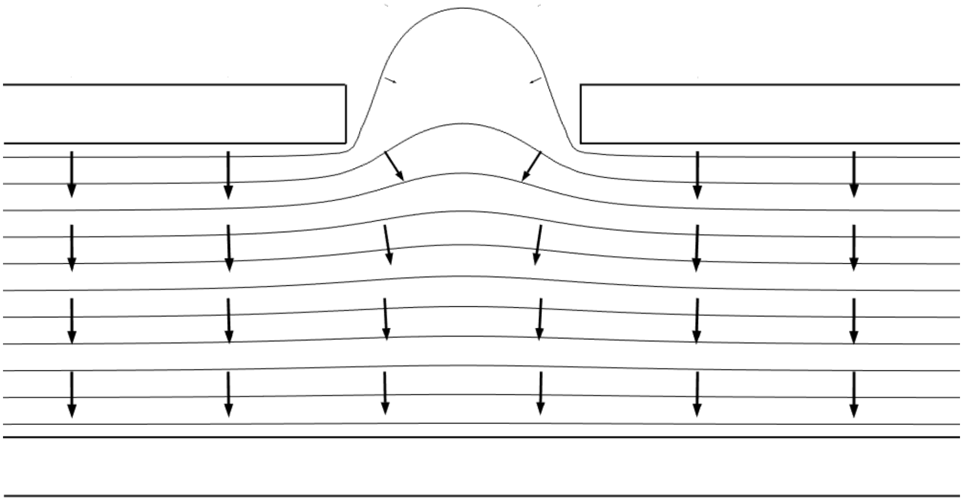

Figure 4.5: Shows an equipotential contour plot of two parallel plates with an aperture in the top electrode. The electrical field is illustrated with arrows, which are perpendicular to the equipotential contours.

Effect of the Aperture

A simple electron gun can be made from the two first parts in Figure 4.1, as previously described. If the cathode and the anode were planar, and infinitely large compared to the aperture and the gap between the electrodes, there would only exist an electric field between the electrodes. The region outside would be field free, except for in the close proximity of the aperture where the equipotential surfaces would bulge through. This is the situation illustrated in figure 4.5. It is seen that the equipotential surfaces near the aperture bulge outwards and the electric field points towards the centre. For an electron this means that the Lorentz force vector will be pointing outwards and the aperture would therefore act as a diverging lens.

Figure 4.6 (a) and (b) show COMSOL simulations of an electron trajectory between two parallel electrodes with finite dimensions. It is seen that the aperture has a diverging effect on the electron trajectory. For the situation shown in (b), the electron is drawn into the anode while in (a) the diverging effect of the aperture is not that severe due to the longer distance between the electrodes. Another effect of the aperture is shown in Figure 4.6 (c) and (d), where the aperture lowers the electric field in the close proximity.

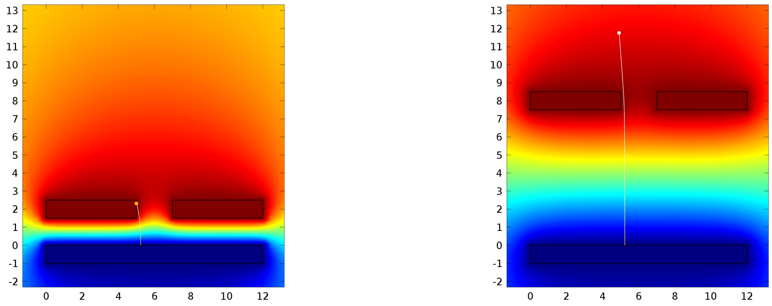

(a) 1.5 mm. **(b)** 7.5 mm.

(c) Without aperture. **(d)** With aperture.

Figure 4.6: Shows some effects of the aperture in an electrode. (a) and (b) show COMSOL simulations of the trajectory of an electron between two parallel plane electrodes measuring 12 mm in width and 1 mm in heigh, and placed (a) 1.5 mm and (b) 7.5 mm from each other. The colour indicates the electric potential distribution. The bottom electrode is at +0 V indicated by blue colour, while the top electrode is at +30 V indicated by red colour. The electron is marked with a circle and its path with a line. (c) and (d) show the electric field between the electrodes without an aperture in (a) and with an aperture in (b). The colour range goes from blue to red, with blue indicating 0 $\frac{V}{m}$

Motion of Charged Particles in a Magnetic Field

The magnetic force component of Eq. 4.5 will, in the presence of a magnetic field, act upon a charged particle in the perpendicular direction of the particle's velocity. This means that the magnetic force can only change the direction of the velocity and not its magnitude. The motion of a particle that moves perpendicular to a magnetic field will be a circle with radius

$$R = \frac{mv}{|q|B} \tag{4.12}$$

This is known as the gyroradius. The equation is also valid for particles which do not travel perpendicular to the magnetic field. Then the perpendicular velocity component with respect to the magnetic field must be used.

4.5 Common Electron Gun Designs

The Wehnelt Cylinder

The Wehnelt cylinder has the shape of a hollow cylinder which is open in the back end, and with an aperture in the front end. The cathode, for instance a filament, is placed inside the cylinder with the tip of the filament pointing towards the centre of the aperture. When the Wehnelt cylinder is biased negatively with respect to the filament, it suppresses electron emission from the filament and thus serves as a control grid for the beam current. Biased less negative and emission will start to take place. The Wehnelt cylinder is shown in Figure 4.7a.

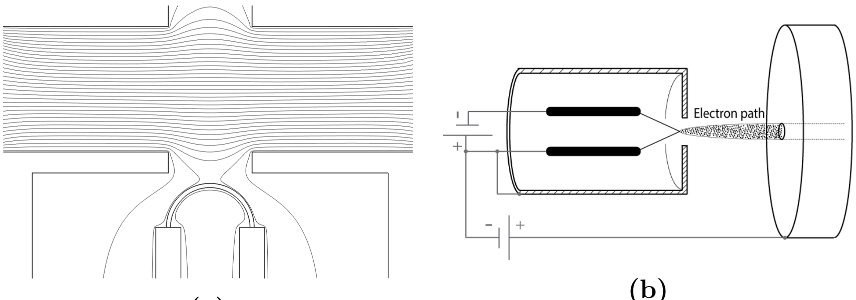

(a)

(b)

Figure 4.7: Shows the Wehnelt cylinder. (a) shows an equipotential contour plot obtained from a simulation performed in COMSOL, while (b) shows the design of a simple electron gun using this design. Figure (b) is adapted from Pierce (1949).

It is seen in Figure 4.7a that the contour lines from the anode reaches only the tip of the filament in the Wehnelt cylinder. It is only here that electron emission will take place. The negative bias of the cylinder, and the curved equipotentials near the filament, will furthermore provide initial focusing of the electrons that are emitted slightly off the symmetry axis. A simple electron gun using this design is described by Pierce (1949) and shown in Figure 4.7b. Here, the cylinder is connected to the positive terminal of the filament and the control action of the cylinder is therefore lost.

Pierce-Type Electron Gun

The Pierce-type electron gun uses angled electrodes which produce a transverse electric field near the cathode. The angles can be chosen such that the transverse electric field exactly cancels the space-charge force, which would otherwise diverge the electron beam. The angles can also be chosen to obtain a converging beam. A COMSOL simulation of a pierce-typed electron gun is shown in Figure 4.8.

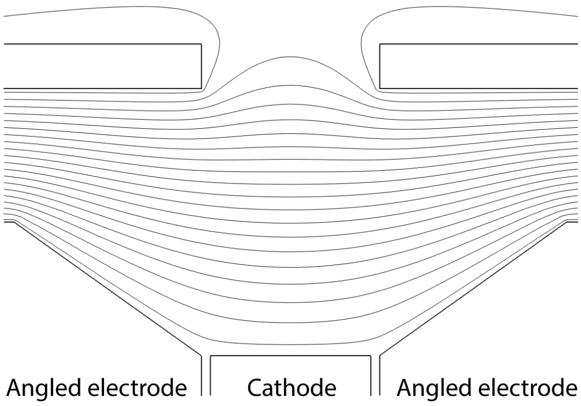

Figure 4.8: Shows a COMSOL simulation of a pierce-typed electron gun. The equipotential contour plot shows that the angles of the cathode provide initial focusing of the beam.

Einzel Lens

An Einzel lens is a converging lens which consist of three hollow cylinders, or apertured electrodes, with the outer two cylinders being at the same potential. The middle cylinder could be either at a higher voltage or a lower voltage than the other two. Figure 4.9 shows a COMSOL simulation of one such configuration with the equipotential curves shown in grey and the trajectory of two electrons shown in black. The background colour shows the potential distribution. The potential distribution in (a) is illustrated with black being the lowest potential and white the highest potential, while in (b) the colours are reversed.

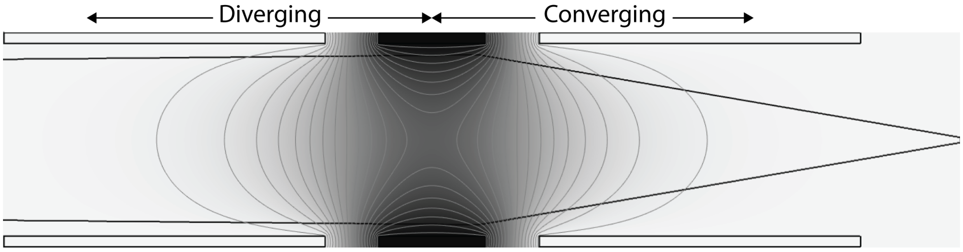

(a) Black indicating a lower potential than white

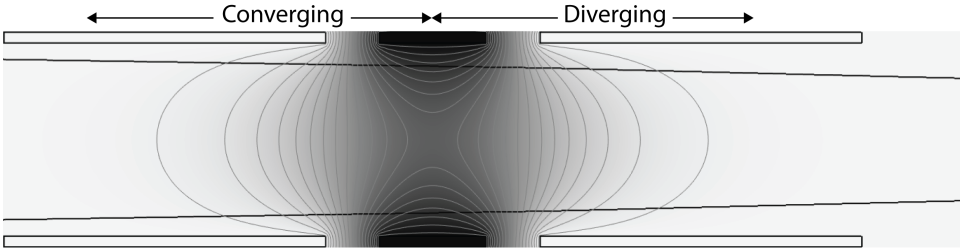

(b) Black indicating a higher potential than white

Figure 4.9: Shows a COMSOL simulation of an einzel lens with (a) the middle electrode being at a lower potential than the other two, and (b) the middle electrode at a higher potential than the other two. The black lines indicate the electron trajectories.

The middle cylinder in Figure 4.9a is at a negative potential with respect to the other two. The electrons are therefore losing some of their velocity while moving through the first part of the lens. The equipotential contours reveal that this region will have a diverging effect on the trajectory, while the second part of the lens will have an converging effect. Since the electrons are moving slower in the second part than they did in the first part, the inwards velocity they gain in the second part will be greater than the outwards velocity they gained through the first part. Hence, the cylinders will act as a converging lens.

The middle cylinder in Figure 4.9b is at a positive potential with respect to the other two. The magnitude of the potential difference between the electrodes, however, is exactly the same as in Figure 4.9a. In this situation the first part will act as a converging lens in addition to speeding up the electrons, while the second part will act as a diverging lens in addition to slowing down the electrons. Since the electrons have a higher speed in the second part, the outwards velocity they gain here will be less than the inwards velocity they gained through the first part. As seen in the figures, having the middle cylinder at a lower potential will give a stronger focusing effect.

Chapter 5

Design of the Miniaturized Electron Gun

Electron guns have been used for spacecraft potential control on larger satellite and rocket missions such as the ISEE-1 satellite and the P119H rocket payload. There are however, to our knowledge, not been conducted much work in designing electron guns for nano- and picosatellites such as CubeSats, where the requirements for size and power consumption are more difficult to meet. This chapter addresses the requirements and needs for such an electron gun, and ends up with a variety of concepts and prototypes used in the experiments presented in chapter 7.

5.1 Design Considerations

When designing a new instrument it is important to identify the needs and requirements which it has to fulfil. This should be done to ensure that, amongst other reasons, no critical parameters is being forgotten and that effort is being made to accommodate the most important ones. Hopefully no major design reviews have to be taken at a later stage in the development process. Following is a list and description of the most important requirements. The design considerations are summarized in Table 5.1 where each entry has been weighted as to identify which requirement should be paid most attention.

Size and Placement The electron gun needs to be designed with a small form factor, low weight and easy mounting to accommodate the CubeSat standard. Ideally, it should be placed facing the opposite direction of the ram-side. This minimizes the risk of the electron beam disturbing the electron density measurements. The placement options on the satellite were however limited, as the electron gun development process was initiated late in the CubeSTAR project. The only real option was to mount the electron gun on the top panel, with electrical connection to the scientific payload subsystem placed about 2-3 cm behind the top panel as seen in Figure 1.1 in Chapter 1. Furthermore the electron gun needs to be placed such that the exit of the gun goes straight to the outside plasma without any object blocking the electron path. Due to the stringent requirements on the dimensions on CubeSats to fit inside the P-POD, no parts can be above the structural poles. This implies that most probably the electron gun has to be mounted inside CubeSTAR with the exit of the gun mounted on the backside of the top panel. This leaves about 2-3 cm in height for the electron gun.

Power Consumption Even though CubeSTAR incorporates high efficiency triple junction photovoltaic cells, the miniature size of the satellite limits the power to about 2 W. This puts a tough requirement on the electron gun, as most commercially available electron guns and cathodes are designed to use several watts of power. It was decided that the electron gun should preferably use less than 100 mW.

Electron Gun Performance The electron gun has to, as explained in Chapter 2, emit a current in the order of 0.5 - 5 μA to be able to control the spacecraft potential. It is of interest to have a high kinetic energy of the emitted beam, as higher kinetic energy will give a lower charge density, and the beam is therefore less prone to disturb the electron density measurements. The beam angle should be kept as small as possible, but as long as the electron beam does not disturb the m-NLP measurements or goes back to the satellite body, it will not pose a problem.

Biasing Electrodes To extract and accelerate the electrons, a biased electrode with respect to the cathode is necessary. The biased electrodes should not interfere with the plasma, and not contribute to collecting more electrons to the spacecraft body. Collecting more electrons to the spacecraft body means the current balance equation is altered, and the electron gun needs to emit a higher current.

Disturbance of other Instruments There are a couple of ways the electron gun might disturb various instruments on CubeSTAR. The first concern, which has already been mentioned, is that the emitted beam disturbs the electron density measurements. The next concern is that, if it is mounted on the outside, it might cast shadows which affects optical instruments like sun sensors and solar cells. A third concern is that if the materials used in the electron gun outgas significantly the material might deposit on optical instruments which will degrade their performances over time. This is probably not an issue for CubeSTAR since the lifetime is rather short. Another concern is that noise might be introduced to the CubeSTAR electrical system if high potentials are necessary, for instance by switching regulators.

Outgassing Outgassing is the process in which gasses are released from a material. This may lead to higher pressure which can affect the electron beam or contaminate the cathode, in addition to the concern stated above.

Laws and Standards The electron gun is intended for CubeSTAR which is a 2U CubeSat. The electron gun therefore has to be built in accordance to the CubeSat Design Specification. Listed below is the requirements found in CDS rev.12 thought most important for the electron gun:

1. CubeSat materials shall satisfy the following low out-gassing criterion to prevent contamination of other spacecraft during integration, testing, and launch. (2.1.7)
    (a) Total Mass Loss (TML) shall be ≤ 1.0 %. (2.1.7.1)
    (b) Collected Volatile Condensable Material (CVCM) shall be ≤ 0.1 %. (2.1.7.2)
2. All components shall not exceed 6.5 mm normal to the surface of the 100.0 mm cube. (2.2.6)
3. Random vibration testing shall be performed as defined by LV provider, or if unknown, GSDC-STD-7000. (3.1)
4. Thermal vacuum bakeout shall be performed to ensure proper outgassinf of components. The test cycle and duration will be outlined by LV provider, or i unknown, GSFC-STD-7000. (3.2)

Table 5.1: Summary of the requirements weighted between one and four, with four being the most important.

Nr.	Needs and requirements	Desired value	Weighting
	The electron gun mitigates spacecraft charging		
1	- the emitted current is of a sufficient value	5μA (min)	****
	The electron gun does not disturb instruments		
3	- the electron gun does not cast shadows		***
4	- the electron gun has no exposed biased electrodes		***
5	- the electron gun does not create electrical noise		***
6	- the electron gun does not outgas significantly		**
7	- the diameter of the emitted beam is small		**
8	- the beam angle is small		**
	The electron gun is functional throughout the mission		
9	- the electron gun can withstand launch		****
10	- the electron gun can withstand the LEO environment	8 weeks (min)	****
	The electron gun is easily integrated into CubeSTAR		
11	- the electron gun use standard mounting techniques		**
12	- the electron gun is lightweight		***
	- the electron gun has a small form-factor		****
13	- the electron gun can operate on available voltages		*
14	- the electron gun consume a small amount of power	100 mW (max)	****
	The electron gun can be controlled		
15	- the emitted current does not vary with time		***
16	- the emitted current is adjustable		**
17	- the kinetic energy of the beam can be varied		**

5.2 Investigation of Existing Solutions

A lot of knowledge can be gained through studying existing solutions. However, as mentioned in the beginning of this chapter, no existing solutions either commercially available or in the literature was found which could be directly used for CubeSTAR. A small selection of the various gun designs that were studied is briefly given below.

Commercially Available Solutions The closest, commercially available electron gun found is the RA-2X1-2 electron gun from Kimball Physics shown in Figure 5.1. With its size of 13 mm in diameter and 17 mm in height it could mechanically fit inside CubeSTAR. The beam current is from 1 nA to 400 μA with energies ranging from 5 to 1000 eV, which means the performance of the gun is more than enough. To achieve this current, it uses a cathode power of about 2.4 W. Lowering the cathode temperature has a severe effect on the emission current, as discussed in the theory section, and it would probably not emit enough current at 100 mW.

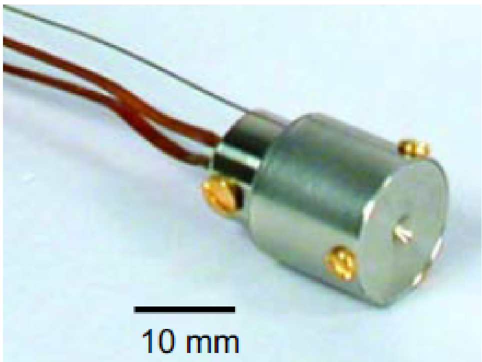

Figure 5.1: Shows an image of the commercially available electron gun RA-2X1-2 from Kimball Physics. Its mechanical properties fits CubeSTAR, but the power consumption is too high.

The P119H Rocket Payload The electron gun used in the P119H rocket payload, described in the article by Polychronopulos and Goodall (1973), consisted of a commercially available light bulb with the glass envelope removed, and a fine, high transparency, stainless-steel grid to accelerate the electrons. The filament, which was rated for 0.5 A at 6 V, was slightly overrun and was capable of ejecting about 0.2 mA of current with an accelerating bias of 10 V when the pressure was 10^{-4} torr. To reduce the angular width of the beam to about 80° they implemented an insulating hood. This was done to avoid the emitted electrons to be collected by the Langmuir probes which would result in errors in the measurements. Attention was paid to make a simple mechanical design, which consisted of 9 mechanical parts excluding the screws.

Field Emission Electron guns based on field emission are widely common. A big advantage of this technology is that the amount of power used is kept to a very minimum, as the cathode does not need to be heated. The only power that theoretically is lost is due to the emitted beam itself, which makes the output power to input power ratio equal to one. A disadvantage with field emission is that it demands a very high electrical field. However, as it is seen in the articles by Milanovic et al. (2001) and Koohsorkhi and Mohajerzadeh (2013), micro- and nanotechnology paves the way for ultra low power field emission devices with really compact design. An electron gun of this type is definitely suited for CubeSTAR, or other CubeSats.

Low Energy Electron Guns The available voltages on CubeSats, such as CubeSTAR, are usually limited to a few volts depending on the electrical power system. This limitation of biasing voltage is not the case for electron guns designed for laboratory equipments down on the Earth, which not uncommonly use voltages in the kilovolt-range. Higher voltages can of course be generated on satellites too, by for instances using boost converters, but not without adding complexity to the design. There are several low energy electron guns found in the literature. Erdman and Zipf (1982), for instance, describes the design of a low voltage, high current electron gun which was used in the laboratory as well as on sounding rockets. They used sapphire balls to electrically and mechanically separate the electron gun elements which were made of axially cylindrical sections of gold-plated copper. The elements were compressed together with 4 screws. They used both tungsten (W) and rhenium (Re) filaments, but preferred Re-filaments on the sounding rockets as they do not become brittle after heating, are less susceptible to poisoning and survives longer in an oxygen environment. The article does not include information about the filament power. A similar electron gun is also described by Raj and Sarma (2004).

Mechanical designs For the electron guns using thermionic emissions, there are two mechanical solutions that recur. The first solution is seen in the articles referred to in the last paragraph, where it is the mechanical housing itself that sets up the electrical field inside the gun. The other solution uses apertured lenses in the form of plane metal plates. The apertured lenses are then separated from each other by, for instance, having the electrodes sported by a non-conductive base, such as Macor ceramic, or by insulating the conducive electrodes from each other by sapphire balls as in the gun described by Ciccacci et al. (1991).

5.3 Clarifying the Problem

Before proceeding to the concept proposals and the actual prototypes that were built during this thesis, a statement made by Pierce (1949) is shared to the reader:

> *"If one wishes to spray a surface with a weak electron beam it is usually foolish to design an electron gun to do this. A tungsten filament and an accelerating grid or apertured plate will do well enough."*

Clearly, the electron gun does not have to be as sophisticated as those used in, for instance, scanning electron microscopes. The main problem becomes how to make the electron gun small enough, light enough and low-powered enough for CubeSTAR and other small CubeSats.

5.4 The Cathode

Thermionic emission was chosen for the electron gun instead of field emission because of design simplicity, whereas secondary and photoelectric emission was not considered at all. Field emission is, as described earlier, an excellent alternative to thermionic emission in CubeSats applications. Making a field emission electron gun is, however, outside the scope of this thesis. As it turned out, thermionic cathodes designed for common electron gun applications, such as in scanning electron microscopes, usually use several watts of power which is unacceptable for small CubeSats with limited power-budgets[1]. Using such a cathode, and running it at a lower power, makes no sense because of the rapid decrease in emission current with temperature as described by Richardson's law. This effectively ruled out the oxide coated cathodes and the dispenser cathodes, which are the most power efficient. A directly heated refractory metal cathode, in the form of a filament, was therefore harvested from a commercially available light bulb in lack of a better alternative, and used as a starting point for the prototypes which were to be built.

5.4.1 Incandescent Wire Terminal Lamps

The incandescent light bulb that were chosen is a miniaturized wire terminal lamp commercially available from Elfa Distrelec. The available information regarding the lamp is limited, as Elfa is in the resale business, however the filament itself is thought to be made of tungsten, either with a work-function lowering coating or not. It should be fairly easy to find a replacement for the lamp later on, if necessary, as the lamp uses wire terminals for connection and has a T 3/4 bulb size. The filament is rated for 17 mA at 3 V, although the current was measured to be 20 mA. This gives a power consumption of only 60 mW, which is well below the desired value stated earlier. The light bulb with the glass envelope intact measures 4.75 mm in length with the diameter of the bulb being only 2.39 mm. The tip of the glass envelope is effectively removed by manually grinding the glass envelope with a diamond whetstone. During the experiments presented in Chapter 7 the distance between the tip of the filament and the edge of the glass bulb were made as small as possible, without destroying the filament. Only the light bulbs with the best centred filaments were used in the experiments. Figure 5.2 shows the light bulb with the tip of the glass envelope removed with a fairly centred filament.

---

[1] During the course of this thesis three companies (Energy Beam Sciences, Inc., Semicon Associates and Kimball Physics) were contacted regarding low power cathodes. The only positive response were from Kimball Physics who was designing such a cathode at the time being. Six months later the development had unfortunately not progressed further

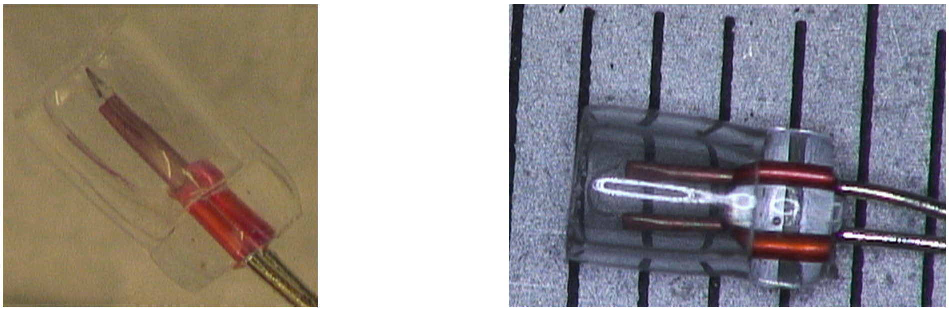

(a) (b)

Figure 5.2: Figure (a) shows the incandescent light bulb with the glass envelope removed from the side, while (b) is taken from the top. The dimensions on the ruler is in millimetre.

5.5 Prototypes and Concept Proposals

This section describes the two latest, of in total four prototypes that were built during the work with this thesis. The two first prototypes that were built are presented in Appendix D together with two other concept proposals that were generated. Initial experiments were performed with these first prototypes while the experimental setup was under development. As no new information was collected from theses tests[2] the results from those tests are not presented in this thesis. The prototypes are presented in chronological order with the earliest prototype built being presented first. The process of concept generation and prototype building became an iterative process, as the test described in Chapter 8 originally was scheduled to be relatively early in the project. The prototypes were designed to be flexible in the sense that multiple electrode configurations could be tested, but they should also be built to accommodate the requirements stated in Section 5.1. It is the mechanical design that is presented here as details about aperture size and electrode configurations were derived through the experiments presented in Chapter 7.

5.5.1 3D Printing and Autodesk Inventor

Many of the concept proposals includes a mechanical housing machined out in the space approved material polyether ether ketone (PEEK). PEEK has low outgassing characteristics and high electrical resistance, and it can therefore serve to electrically and mechanically separate the electrodes. Instead of machining out the housing in PEEK during the prototyping, it

---

[2] The configuration of prototype 0.2 was made to replicate the configuration shown in Figure 4.7b. The result was no measurable beam current with acceleration voltages of up to 30V, implying that the apertures in the cylinder and anode of 1.0 mm and 0.5 mm were too small.

was decided to fabricate the housing in ABS plastic using 3D printing, also known as additive manufacturing. One concern about this method is the high outgassing characteristics of ABS plastic. Outgassing might increase the pressure locally in the electron gun and affect the performance of the gun itself, in addition to the risk of contaminating the vacuum chamber [3]. However, it was believed that the local pressure near the plastic were within a power of ten of the global pressure in the vacuum chamber.

---

[3] Permission was granted to use plastic in the vacuum chamber.

5.5.2 Prototype 1

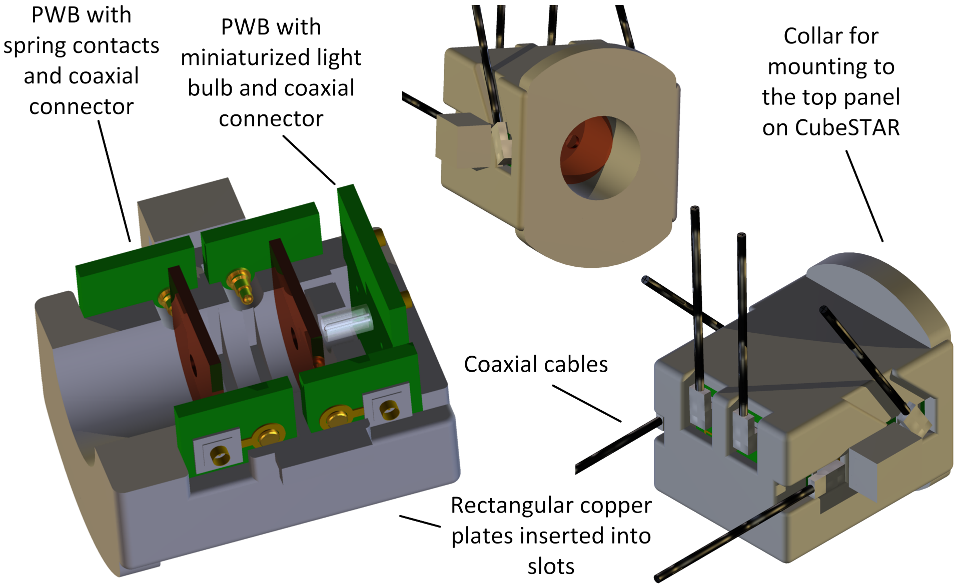

Cathode	Electrodes	Mechanical housing	Focusing
$\boxed{\text{Thermionic}}$	$\boxed{\text{Metal plates}}$	$\boxed{\text{PEEK house}}$	$\boxed{\text{Wehnelt}}$
Field	Embedded in housing	Supporting rods	Pierce type
	Plated through-holes	Aluminium house	$\boxed{\text{Einzel lens}}$
			Magnetic lens
			$\boxed{\text{None}}$

Figure 5.3: Shows an illustration of the concept for prototype 1. The table indicates the different options that were considered for each element, with the framed boxes indicating the applicable ones.

This concept involves embedding the electrodes into slots in a mechanical housing machined out in PEEK. The electrodes are made of copper plates with apertures drilled into the centre. A spring loaded connector is soldered onto a printed wiring board (PWB), which is inserted into slots in the side-walls of the housing, together with a coaxial connector. Electrical contacts to the electrodes are thus made without the need to solder wires directly onto the copper plates, which is difficult to do due to the heat loss. Furthermore, it will be easier to change the electrodes in between the experiments, and there is no stress applied to the electrodes from the wire. Coaxial connectors and cables were chosen to minimize noise during measurements on the electrode currents, and leakage current can be minimized by using guarding on the shield. The wires going to the electrodes are lead away from the electron path to avoid disturbance of the electrical field. The miniaturized light bulb is soldered onto a PWB placed in the back of the housing.

Prototype Realization

The mechanical drawings for the housing were made using Autodesk Inventor, and fabricated using the aforementioned 3D printer. Details about the prototype are given in Section D.4 in Appendix D, and photographs are presented later in Chapter 7. Dimensions which are not affecting the positioning of the electron gun elements are omitted from the mechanical drawings, as it is not important in this context.

There are some deviations from the mechanical drawings to the actual prototype that was built, which will now be explained. Due to the miniaturized size of the coaxial cables, it was difficult to solder the wires onto the vacuum feedthrough. The AMC (Amphenol Micro Coaxial) connector and cables, which were originally intended, were therefore omitted and PTFE insulated wires were instead soldered directly onto the pads on the PWBs. The copperplate marked with the number 4 in the appendix were designed to be 0.5 mm thick. A 0.7 mm thick plate was used instead, as the 0.5 mm thick plates no longer were available during the prototype building. This particular slot had to be made wider manually so that the 0.7 mm thick plate could be inserted. The printed wiring boards were furthermore 0.1 mm thicker than the slots in the mechanical housing, and had to be grinded down to fit. The relatively coarse tolerance of the 3D printer, the cutting of the printed wiring boards and the copperplates required some minor adoptions to the parts to get everything to fit nicely.

A second prototype was built to have as a spare during the testing presented in Chapter 8. In this prototype, the issues previously explained was resolved. However, as the test was postponed and the prototype presented in the next section was built, there was not conducted any experiments with this new version. Mechanical drawings and PWB layout is therefore omitted.

5.5.3 Prototype 2

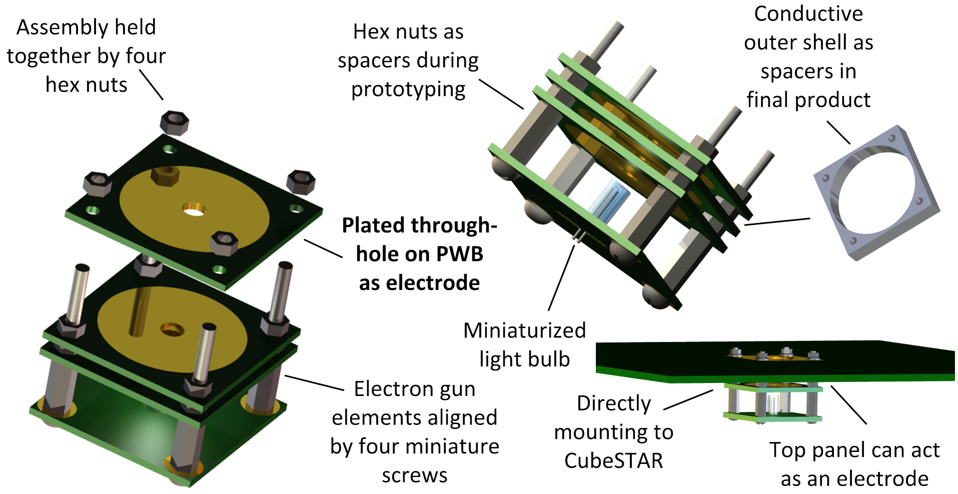

Cathode	Electrodes	Mechanical housing	Focusing
$\boxed{\text{Thermionic}}$	Metal plates	PEEK house	$\boxed{\text{Wehnelt}}$
Field	Embedded in housing	$\boxed{\text{Supporting rods}}$	$\boxed{\text{Pierce type}}$
	$\boxed{\text{Plated through-holes}}$	$\boxed{\text{Aluminium house}}$	$\boxed{\text{Einzel lens}}$
			$\boxed{\text{Magnetic lens}}$
			$\boxed{\text{None}}$

Figure 5.4: Shows an illustration of the concept for prototype 2. The table indicates the different options that were considered for each element, with the framed boxes indicating the applicable ones.

This concept involves having apertured electrodes stacked on top of each other. To avoid having excess mechanical parts such as insulating ceramic bases or sapphire balls, this concept uses plated through-holes on printed wiring boards as the apertured electrodes. Having the electrodes already supported by an insulating material reduces mechanical parts and making it less fragile and space-consuming. The electrodes are supported and aligned by four metal screws through the insulating part of the printed wiring boards. The electron gun will be mounted directly to the top panel using the metal screws, which also can act as one of the electrodes. The miniaturized light bulb is soldered onto the base printed circuit board (PCB), together with wires from the electrode PWBs. Hex nuts will be used as spacers, which is a more flexible solution during experimentation than prototype 1. There will also be very easy to manufacture various electrode shapes in large quantities with very little effort. Insulating parts visible to the electron beam is also minimized.

Prototype Realization

The PWB layout for the electrodes was made in CADSTAR, and the board etched out by the electrical workshop without the possibility for plated through-holes. Both 1.00 mm thick PCBs and 0.50 mm thick PCBs were manufactured and used in the experiments. The apertures and the holes for the screws were drilled out manually which may have lead to poor alignment of the electrodes in the electron gun. The diameter of the electrodes/pads are 12 mm. As the through-hole via's are not plated there will be insulating parts inside the apertures after drilling, and also risk of copper traces sticking out, possibly creating higher electric field in the near proximity. Miniaturized metal screws, hex nuts and washers were ordered from Hilco[4] with a screw diameter of 1.16 mm, and lengths of up to 20 mm. The light weight of the electron gun allows such small mechanical dimensions. Details about the prototype are given in Section D.5 in Appendix D, and photographs are presented later in Chapter 7.

The issues present in the prototype realization vanishes when the electrodes are produced by companies specialised in PCB production, such as Elprint and Printline[5]. The alignment of the electrodes will then be determined by the producers manufacturing specification, whereupon Printline have, according to their website, a positioning accuracy of ± 0.05 mm. Their aspect ratio on through holes, expressed as the ratio between PCB thickness and diameter of hole, is 1:8. This means that a PCB with 1.0 mm thickness can have apertures of up to 8.0 mm in diameter. The circuit board can further be made of different materials including polyimide, and the copper traces can be plated.

---

[4] www.hilco.com

[5] http://elprint.no/ and http://printline.dk/ - Accessed 24.11.2013

Chapter 6

Equipment and Method

This chapter describes the equipment and method used to derive the electrode configuration of the electron gun. The methodology used is visualized through the flowchart in Figure 6.1. An electrode configuration is assembled into one of the prototypes described in Chapter 5. The choice of electrode configuration is based upon theory, electrode configurations found in the literature and on previous experiences. This new configuration is then characterized through both simulations and experiments. It is then decided whether or not the configuration meets the needs and requirements stated in Section 5 - if not, the process is repeated. The experimental setup and the simulation tool used is described in the following sections.

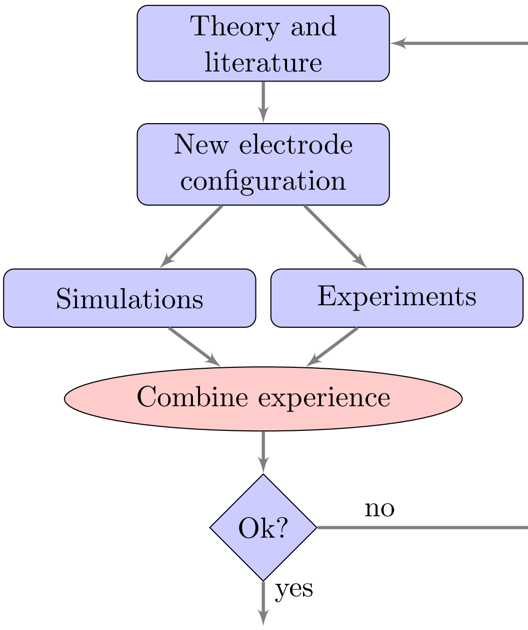

Figure 6.1: Flowchart of the methodology used to derive the electrode configuration of the electron gun.

6.1 Experimental Setup

The experiments presented in this thesis were conducted inside the clean-room laboratory at MiNaLAB in Oslo. To characterize the performance of the prototypes and the different electrode configurations, a measurement system running a set of automatic test procedures was made and used throughout the experimentations. The system consisted of a laptop running a LabVIEW program, which were controlling both a precision power supply (PS) and a high resolution source measurement unit (SMU) via GPIB, and a vacuum chamber where the electron gun and a mechanical test fixture were situated. A connection board was made, and used, to ease the rewiring of the electrical connection between the instruments and the device under test (DUT). The system is illustrated in Figure 6.2, and each subsystem is explained in detail in the following subsections.

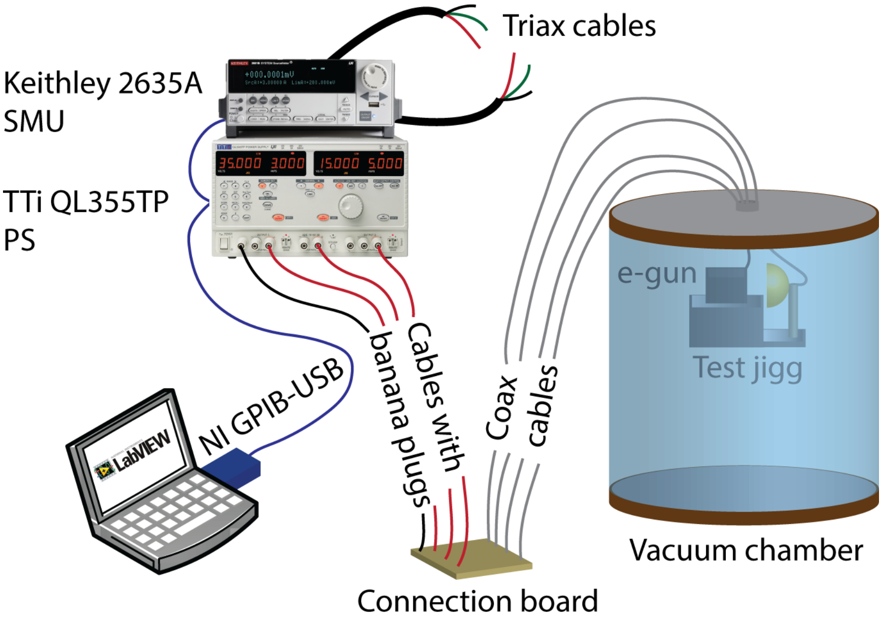

Figure 6.2: Shows an overview of the experimental setup. A LabVIEW program running on a laptop was used to run a predefined test procedure using a source measurement unit and a power supply which were programmed via GPIB. The connection board served as an interface between the instruments and the electron gun situated inside the vacuum chamber to ease electrical wiring. The electron beam was collected by a Faraday cup mounted on a mechanical test fixture in front of the electron gun.

6.1.1 LabVIEW program

As described in the theory section, the current from a thermionic electron gun depends on both the filament temperature and the electrode potentials. It was therefore of interest to test each DUT for multiple filament voltages and electrode voltages. Two test procedures were defined: (1) filament sweep and (2) anode sweep. These procedures could be carried out manually, by operating the knobs on the instruments and record the voltage and current. However, this method is prone to human errors. The time between each new set of voltages and measurements would in addition be highly variably, which is undesirable if, for instance, the process has a hysteresis. It was therefore decided to implement the test procedures in a software to extract the characteristics of the different DUTs.

Filament Sweep

The purpose of the filament sweep is to produce a plot similar to the one shown in Figure 4.4c in chapter 4. The main features of this test procedure can be summarized as follows:

1. Set the desired electrode voltages including the anode voltage
2. Set filament voltage to a predefined start voltage.
3. Stepwise increase the filament voltage with ΔV.
4. Record voltages and currents.
5. If maximum filament voltage is reached proceed to step 6, otherwise go back to step 3.
6. If selected, go back to step 2 and repeat the process with decreasing filament voltages to check for hysteresis.

This test will typically be repeated for several anode voltages, which could have been implemented as step 7. The procedure is especially suited for characterising the emission current of the filaments.

Anode Sweep

The purpose of the anode sweep is to produce a plot similar to the one shown in Figure 4.4b in chapter 4. The main features of this test procedure can be summarized as follows:

1. Slowly increase the filament voltage to a predefined start voltage.
2. Wait 30 seconds to reach thermal equilibrium.
3. Stepwise increase filament voltage (if first iteration, use start voltage).
4. Wait 10 seconds to reach thermal equilibrium.
5. Set electrode voltages to a desired value and the anode voltage to the start voltage.

6. Stepwise increase the anode voltage with ΔV.
7. Record voltages and currents.
8. If maximum anode voltage is reached proceed to step 9, otherwise go back to step 6.
9. If maximum filament voltage is reached proceed to step 10, otherwise go back to step 3.
10. If selected, go back to step 3 and repeat the process with decreasing filament voltages back to the start voltage to check for hysteresis.

This procedure will give knowledge about how the DUT respond to small changes in anode voltage, for different filament voltages.

The LabVIEW environment

LabVIEW$^{\text{TM}}$ 2011 from National Instruments was chosen as the software platform for the measurement system. LabVIEW is widely used for measurement, test and control systems as it amongst other reasons provides easy integration with a wast amount of hardware devices. As an example, software drivers for both the SMU and the PS were available from the producers, making the programming of the instruments almost plug-and-play. LabVIEW programs are called virtual instruments (VIs), and a VI may consist of several smaller VIs which is then referred to as SubVIs. A VI is used as a subVI in the block diagram of another VI with the use of the connector pane. The programmer of a VI sees the front panel which is the graphical user interface (GUI), and the block diagram which is the dataflow diagram for the VI. The diagram is programmed with the graphical programming langugage G, which is based upon as already mentioned, dataflow rather than the conventional control flow.

The Electron Gun Measurement System Virtual Instrument

The VI presented in this thesis is called the *ElectronGunMeasurementSystem* (EGMS), and it is the final version EGMSv4.061.vi, hereby referred to as EGMS.vi, that is presented. The LabVIEW code are shown in section B.1 in Appendix B, while the main structure of the VI is explained here. To save pages, only a subset of the code is included in the Appendix.

Front panel The front panel of the EGMS.vi is organized into four pages. Page one is the settings page which is the default page. When the program is started, the operator sets the GPIB addresses to the instruments and chooses the desired DUT connection in a pop-up window. This information is then written to the settings page as information to the operator, and cannot be changed when the program is running. The DUT connection gives the program information about which instrument and output is connected to the different electron gun elements. This hides the electrical configurations for the operator and enables him to, for instance, ask for a sweep on the filament voltage rather than asking for a sweep on output 1 on the PS. Page two contains the controllers and indicators which enable the operator to program the instruments with simple commands. Page four contains the controllers and indicators for performing continuous data acquisition with changeable voltages. The first page together with the pop-up window, page two and page four is shown in Figure B.1, B.2 and B.3 respectively in Appendix B. The third page is the most important, and contains the controllers and indicators necessary to perform the previously mentioned test procedures. This page is shown in Figure 6.3.

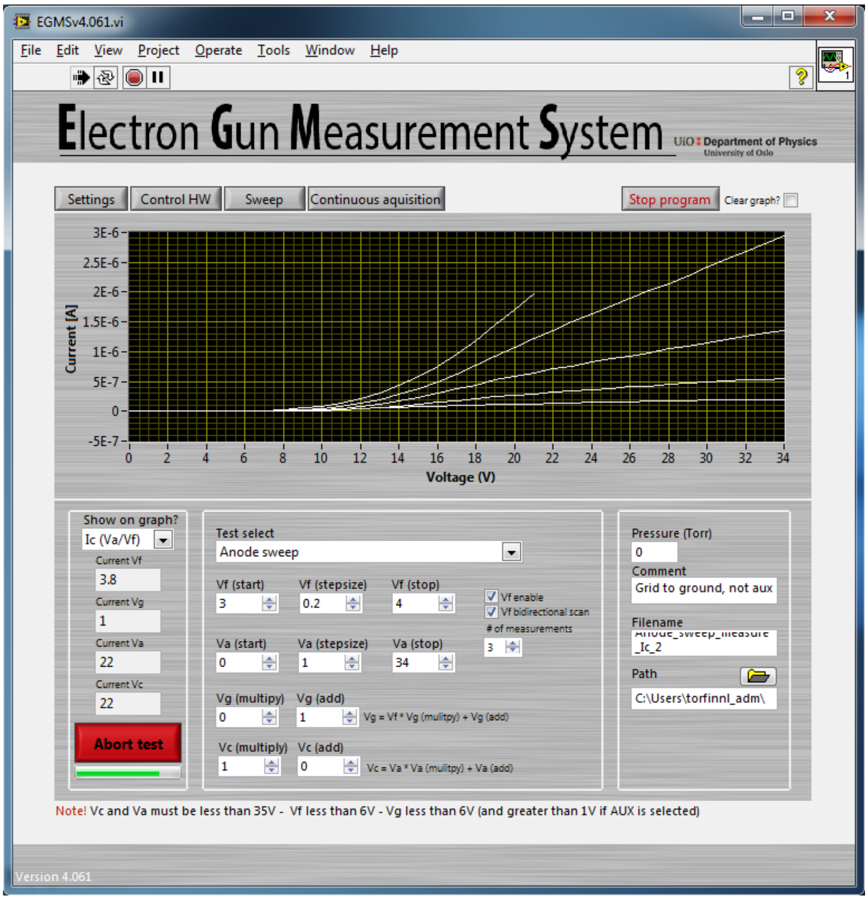

Show on graph?: Ic (Va/Vf)

Current Vf: 3.8

Current Vg: 1

Current Va: 22

Current Vc: 22

Test select: Anode sweep

Vf (start): 3

Vf (stepsize): 0.2

Vf (stop): 4

☑ Vf enable

☑ Vf bidirectional scan

# of measurements: 3

Va (start): 0

Va (stepsize): 1

Va (stop): 34

Vg (multipy): 0

Vg (add): 1

Vg = Vf * Vg (mulitpy) + Vg (add)

Vc (multiply): 1

Vc (add): 0

Vc = Va * Va (mulitpy) + Va (add)

Pressure (Torr): 0

Comment: Grid to ground, not aux

Filename: _Ic_2

Path: C:\Users\torfinnl_adm\

Note! Vc and Va must be less than 35V - Vf less than 6V - Vg less than 6V (and greater than 1V if AUX is selected)

Figure 6.3: Shows page three of the EGMS.vi during an anode sweep. The controllers set the parameters used in the test sequence as described in section 6.1.1. As indicated by the checkbox, a bidirectional scan was requested which means that anode sweeps for decreasing filament voltages was performed after completing the 4V-filament voltage sweep. An option to clear the graph was also implemented.

Block diagram The design pattern used in the block diagram is the producer/consumer architecture. This is a commonly used design pattern in data acquisition systems, as it is based on multiple loops running at different rates. The producer loop typically will do the data acquisition at a high rate, and the data is then sent to the consumer loop through a queue which serves as a buffer. Slow processes such as graphical representations of the acquired data and write-to-file operations are performed here. By doing this the data acquisition in the producer loop will not be slowed down by the time-consuming processes in the consumer loop. In the EGMS.vi the producer/consumer architecture is used as a GUI event handler, as there is no need for high speed data acquisition. In this way the code for the GUI is separated from the rest of the code. The basic architecture of the EGMS.vi is shown in Figure 6.4.

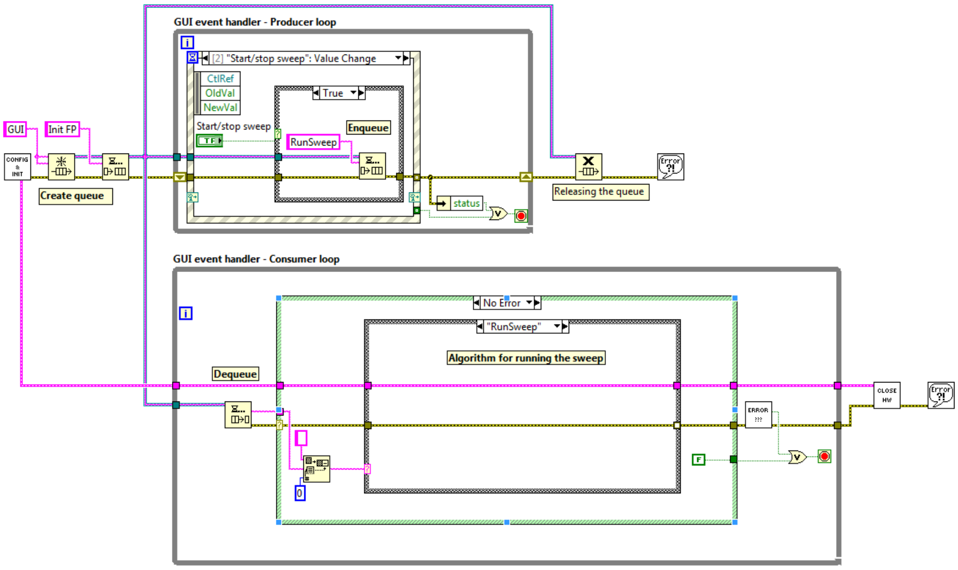

Figure 6.4: The prodcuer/consumer architecture was used as a GUI event handler in the EGMS.vi. This serves to separate the code for the GUI events from the rest of the code, and increases the user interface responsiveness.

The producer loop sleeps until an event triggers the event structure inside the loop. The event case are triggered by controllers on the front panel, for instance by the *Start/stop sweep* button. If this button is pushed, the event case corresponding to that controller is triggered and the while loop iterates once. In the Start/stop sweep button case, the text string *RunSweep* is enqueued. The text string is dequeued in the consumer loop using the first-in, first-out principle, which in turn is interpreted by the inner case structure. In the RunSweep-case the code for the anode sweep and filament sweep are implemented as a state machine.

The anode sweep and filament sweep could have been implemented with a set of for loops as the test sequence and number of iterations are well defined, and does not change once the test has started. This was done in the earliest version of the software. However, as the test sequences include several wait states it was decided that a state machine would be a more comprehensible solution. For instance, there is a 1 second delay between each time a new voltage is set. This is to ensure that the outputs of the PS, with a settling time of 600 ms with no load, have reach its final value before measurements are being performed. As it can be difficult to read the code for the state machine, a state machine diagram has been drawn and included in Section B.1 in Appendix B.

Each performed test is written to two separate files, one containing the settings and the other containing the actual measurements. It is the read-back voltages from the outputs that are written, and not the programmed ones. The currents from the corresponding outputs are measured and written to the file as well. However, as the resolution of the PS is quite coarse, it is the SMU output together with the output used to power the filament that is of main interest. Figure 6.5 shows a section from one of the measurement files. A matlab script for reading and plotting the results from the sweeps was made and used for most of the plots presented in chapter 7. The matlab scripts for loading and plotting the files from the anode sweep are given in section B.2 in Appendix B. The script for reading and plotting the results from the filament sweep is fairly similar and thus omitted.

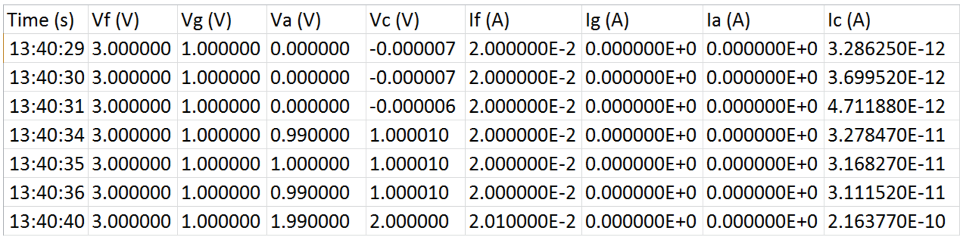

Time (s)	Vf (V)	Vg (V)	Va (V)	Vc (V)	If (A)	Ig (A)	Ia (A)	Ic (A)
13:40:29	3.000000	1.000000	0.000000	-0.000007	2.000000E-2	0.000000E+0	0.000000E+0	3.286250E-12
13:40:30	3.000000	1.000000	0.000000	-0.000007	2.000000E-2	0.000000E+0	0.000000E+0	3.699520E-12
13:40:31	3.000000	1.000000	0.000000	-0.000006	2.000000E-2	0.000000E+0	0.000000E+0	4.711880E-12
13:40:34	3.000000	1.000000	0.990000	1.000010	2.000000E-2	0.000000E+0	0.000000E+0	3.278470E-11
13:40:35	3.000000	1.000000	1.000000	1.000010	2.000000E-2	0.000000E+0	0.000000E+0	3.168270E-11
13:40:36	3.000000	1.000000	0.990000	1.000010	2.000000E-2	0.000000E+0	0.000000E+0	3.111520E-11
13:40:40	3.000000	1.000000	1.990000	2.000000	2.010000E-2	0.000000E+0	0.000000E+0	2.163770E-10

Figure 6.5: Shows a section from one of the measurement files obtained during one of the experiments. The headers are marked with the name of the gun element instead of the output being connected. Information regarding the actual outputs used and the electrical configuration is found in the settings file.

6.1.2 The Instruments

Keithley 2635 To measure the current from the Faraday cup, as well as from the electrodes in the DUT, a Keithley model 2635 single-channel source measurement unit was used. A source measurement unit has the possibility to both source and measure at the same time, so the Ketihley 2635 could be used for providing biasing voltage while measuring the current with high accuracy. The test leads used was the 237-ALG-2 triax cable, which is terminated with a 3-slot triax connector on one end and alligator clips on the other end. The cables are only rated for voltages less than 42 V, which limits the voltage a DUT could be tested. The LO connection terminal is connected to ground through the power supply to avoid ground loops and avoid potential differences. Since the SMU is single channel it had to be physically rewired, and the test repeated, in order to measure the current from the different electrodes and the Faraday cup.

QL355TP To power the filament and biasing the electrodes, a TTi Series II model QL355TP power supply was used. The PS has two main outputs with an operating range of, amongst others, 0V to 35V/0.1mA to 500mA. In addition to the main outputs it has an auxiliary output with voltage range from 1V to 6V with poorer resolution and accuracy. The outputs of the power supply are fully floating and can thus be used in series to provide higher voltages.

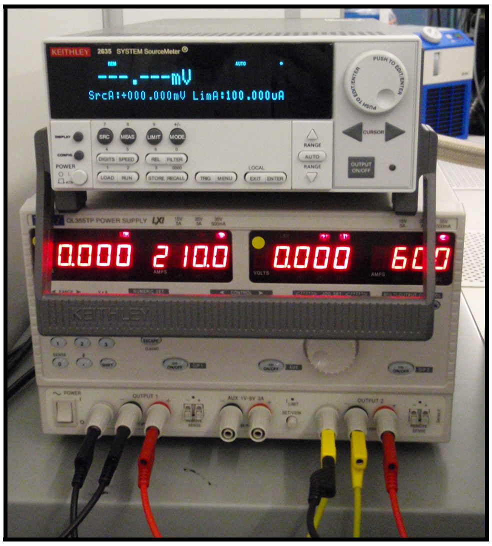

Figure 6.6: Shows a photograph of the instruments used in the experiments. The top instrument is the Keithley 2635 SMU, and the bottom instrument is the TTi QL355TP PS.

6.1.3 Connection Board

The connection board serves as an interface between the instruments on the atmosphere side of the vacuum chamber and the DUT on the inside. The connection board is shown in Figure 6.7a while a modified figure of the PCB layout is shown in Figure 6.7b. The schematic for this PCB is omitted from the thesis due to its simplicity.

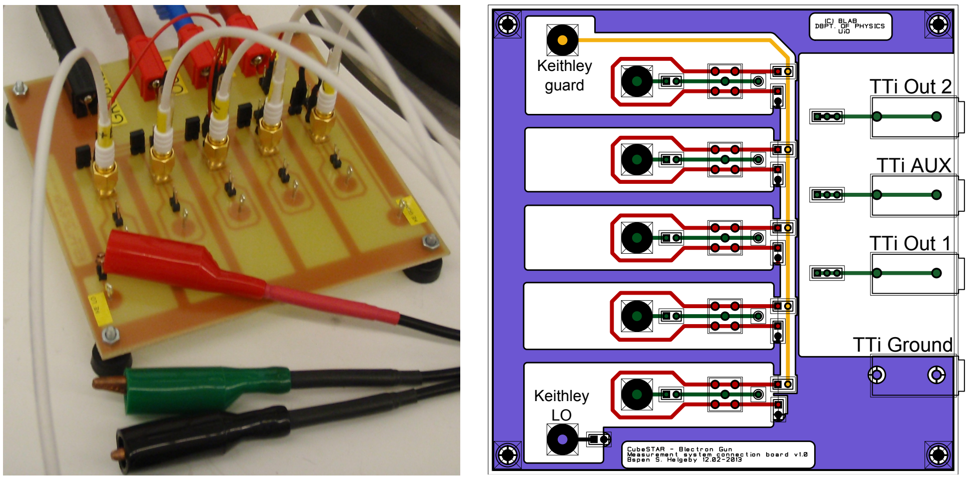

(a) (b)

Figure 6.7: Shows the connection board used in the experiments, where (a) shoes the physical board and (b) shows the PCB layout.

The outputs from the PS are connected to the connection board via banana plugs. From here the different outputs can be connected to any of the centre conductor of the coaxial cables through jumpers. The green coloured lines in Figure 6.7b show the position of the connectors, jumpers and copper traces providing these features on the connection board. The coax cables lead up to the vacuum chamber where the centre conductors are soldered to pins on the electrical feedthrough. The LO connection terminal from the SMU is connected to TTi ground with the crocodile clip of the 237-ALG-2 attached to a test point on the connection board. The copper traces and the test points providing this feature are shown in purple in Figure 6.7b. The shield of the coaxial cable can be connected to either ground or the guard terminal of the SMU to minimize leakage current. A guard trace is incorporated in the PCB to avoid leakage currents here too. This is probably not necessary as the PCB is quite spacious. The copper traces, jumpers and test point providing this feature are shown in yellow colour in Figure 6.7b. Care should be taken when floating the shield on coax cables to high voltages. To measure the current from the electrodes with the SMU, the HI terminal can be connected via the test points on the board coloured in green.

6.1.4 Vacuum System

The vacuum system was evacuated in two stages, first by a Varian roughing pump then by a Pfeiffer turbo pump. The pressure obtainable during testing was around 10^{-6} torr depending on the pump-down time. This corresponds to a mean free path of about 50 m based on the simple formula $\lambda = 5 \cdot 10^{-3}/p$ given by Roth (1976). The vacuum envelope itself had to be replaced and a custom built endplate in aluminium had to be fabricated, as the original vacuum envelope did not include electrical feedthroughs. The electrical feedthrough mounted in the new endplate has 10 connection points with solder cup termination. The vacuum chamber is roughly 32 cm in diameter and about 38 cm in height, and the available space inside the chamber is limited as seen in Figure 6.8. Effort was made to avoid materials with high outgassing such as PVC isolation found on regular wires and shrink tubes[1].

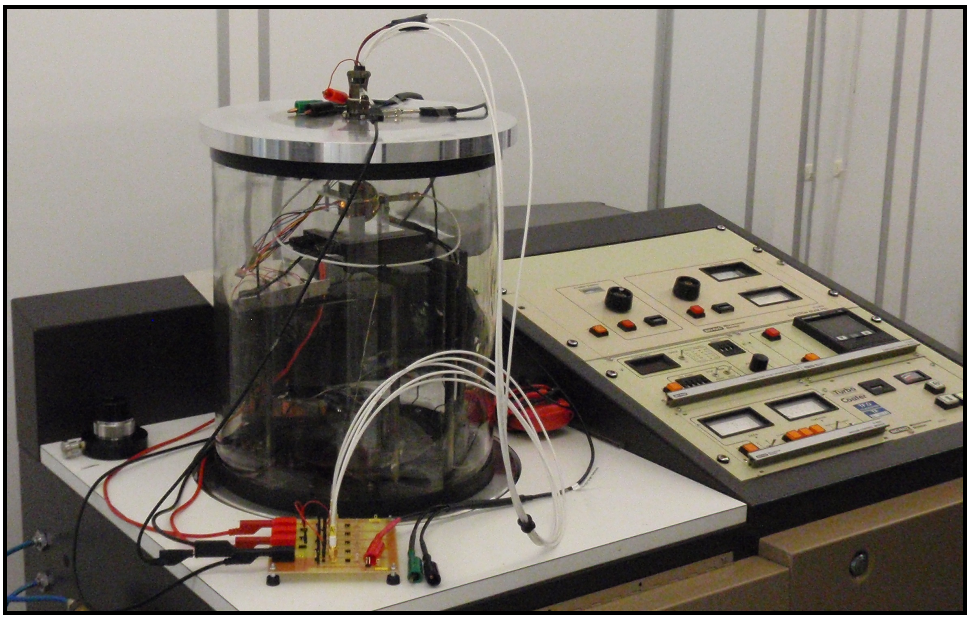

Figure 6.8: Shows a photograph of the vacuum chamber used in the experimental setup. The chamber was originally used for material deposition so adjustments and adaptations had to be taken.

---

[1] For more information on outgassing data, see: http://outgassing.nasa.gov/ or http://nepp.nasa.gov/npsl/wire/insulation_guide.htm

6.1.5 Mechanical Test Fixture

The purpose of the mechanical test fixture is to hold, and align, the electron gun so that the exit of the gun is pointed towards the center of the Faraday cup. The test fixture is fabricated in aluminium, while the Faraday cup is made of a titanium nitride (TiN) coated Langmuir probe which is cut in half. The Faraday cup is mounted on the tip of an isolating boom with coaxial connection at the other end. The boom is attached to the fixture using two screws. The purpose of the Faraday cup is to collect the electrons emitted from the gun. The current which is produced when the electrons dissipates into ground can then be measured with a measurement unit. The fixture was originally designed to align the first prototype, described in Section D.1 in Appendix D, with the centre point of the cup, but due to minor variations in dimension between the prototypes the fixture was not adapted to each prototype. The mechanical test fixture with the Faraday cup mounted is shown in Figure 6.9. The fixture was made to fit on top of the stand which was already integrated into the vacuum system as shown in Figure 6.9c. The stand was connected to earth ground through the vacuum system.

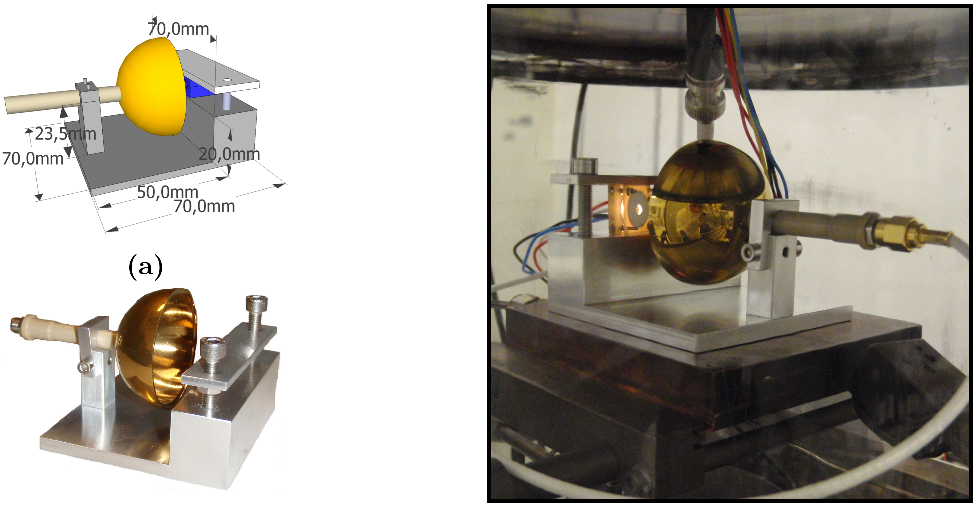

(a)

(b)

(c)

Figure 6.9: Figure (a) shows the sketch of the mechanical test fixtures with dimensions added, (b) shows the actual fixture made by the mechanical workshop, and (c) shows the fixture placed inside the vacuum chamber during testing.

6.1.6 Uncertainty Analysis

This section will briefly investigate two quantities in the measurement model of the system that will affect the accuracy of the results. There has not been made an attempt to set up the entire measurement model, as this is not necessary for the initial parts of the electron gun development process. The accuracy of the Keithley instrument is given to be ±0.15 % of the reading + 240 fA. For a measurement of 1μA, this gives an accuracy of ±1.0 nA. More details about the resolution and accuracy of the instruments can be found in the datasheets.

Leakage Current

During the experiments presented in Chapter 7, the leakage current was measured from time to time. The leakage current was measured by performing an anode sweep with the filament-output disabled. In Figure 6.10 the measured leakage current from the Faraday cup and the electrodes obtained during some of the experiments are presented. The shield on the coax cables was grounded, as it was during the experiments. The current is presented on the y-axis and the voltage on the x-axis, and hence the slope of the linear fit will directly give the leakage resistance.

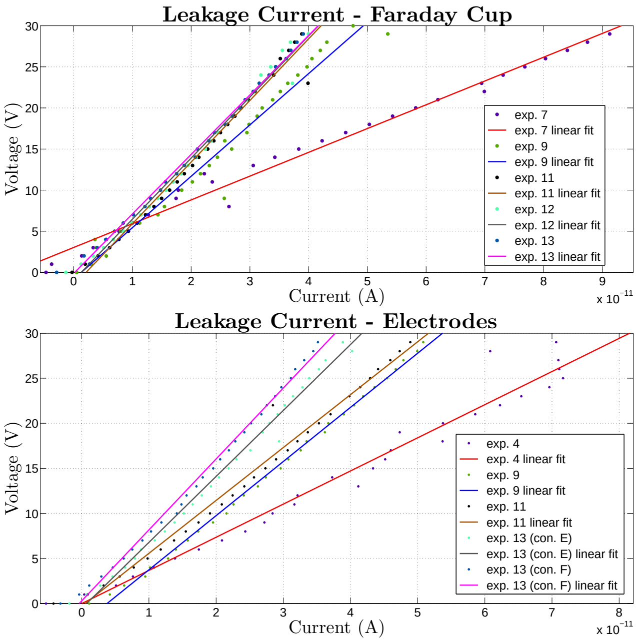

Figure 6.10: Shows the measured leakage current in the measurement system.

As seen in the figures, the leakage current in the system is small. The average of the slopes of the linear fits gives a mean leakage resistance of 626 GΩ for the Faraday cup, and 615 GΩ for the electrodes. This gives a leakage current, when the voltage is +42 V, of 0.06 nA and 0.07 nA respectively. The leakage current is most likely dominated by the resistance in the vacuum feedthrough. The leakage current in the system is small enough to be neglected for the purposes of the experiments performed during this thesis. There is no need to use guarding on the coax shields.

Wire Resistance

The measured filament voltage includes the voltage drop over the wire resistances from the instrument to the DUT. This can be corrected by measuring the wire resistances as illustrated in Figure 6.11. The voltage drop over the wires can be neglected for the Faraday cup and the electrodes as the current here is small.

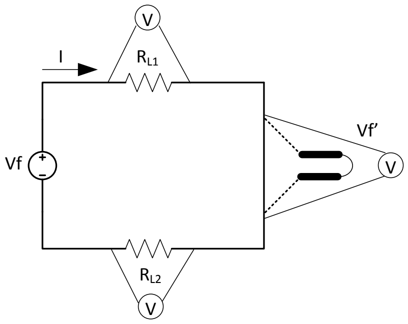

Figure 6.11: Shows the voltage drop that occur over the wire resistances to the DUT. The true voltage over the filament can be found by correcting for this.

The true voltage drop over the filament is given by:

$$Vf' = Vf - IR_L, \quad R_L = R_{L1} + R_{L2} \tag{6.1}$$

The wire resistances were measured by replacing the filament from the experimental setup with a short wire. For the configuration when the filament was powered by the PS, the banana plugs were connected directly to a UNI-T UT33D digital multimeter and the total wire resistance was measured. For the configuration when the filament was powered by the SMU, the triax cables were connected as it was during testing and the total wire resistance was measured directly with the SMU. As there is not introduced any new wires to the experimental setup, there is no need to use four-terminal sensing. The total wire resistance for the PS-connection was measured to be between 0.6 and 0.8 Ω depending on which connectors was used on the connection board and which output was used. The total wire resistance for the SMU-connection was measured to be 1.5 and 1.8 Ω, depending on which two connectors for powering the filament was used.

6.2 Computer Simulations

Computer simulations can be an important tool when designing electron guns. Configurations can be tested with minute amount of time spent once the model is properly set up, without having to physically build and test them. This is convenient if the design phase includes many different configurations. The visualization of the electron trajectories and the electric and magnetic fields that are affecting them, as seen in Figure 6.12, may also help explain the observations made in experiments.

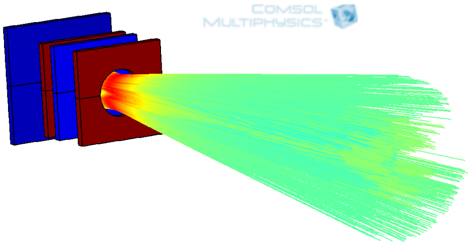

Figure 6.12: Shows a simulation of the particle trajectories in one of the models that were built during the thesis.

6.2.1 The COMSOL Environment

COMSOL Multiphysics 4.3a[2] was used throughout this thesis for computer simulations. This software can handle conventional models of one type of physics as well as multiphysics models that involve coupled physics phenomena - without requiring the user to have in-depth knowledge of mathematics and numerical analysis. COMSOL uses the *finite element method* (FEM) to solve a model. The model is broken down to subdomains, defined by the *mesh*, and the differential equations are solved at each node of the mesh.

6.2.2 The COMSOL Model

The primary reason for creating COMSOL models was to visualize the potential distribution in the electron gun. To do so the *Electrostatics (es)* study type in the *AC/DC* module was solved for stationary solutions[3]. The geometry of the model was built using parameters, which made it easy to change the configurations and even do parametric sweeps. Mostly, full 3D-models were created to capture the effect of the filament shape. The electrodes, which are symmetrical around the centre of the aperture, could have been modelled in 2D to save computational time.

---

[2] www.comsol.com - information taken from the user's guide.

[3] In some of the models the study type electric currents were used to embed the voltage drop over the filament. This, however, created some side-effects that were not resolved.

The next step after creating the geometry is to assign materials to the geometry, and properties like electric potential to the es study type. To define the finite elements, a mesh must be created. This can be done more or less automatically by the *Physics-controlled mesh*, or by the *User-controlled mesh*. The latter type was often used to create more dense mesh near the electron path, and regions with fast varying electric potential, as seen in Figure 6.13.

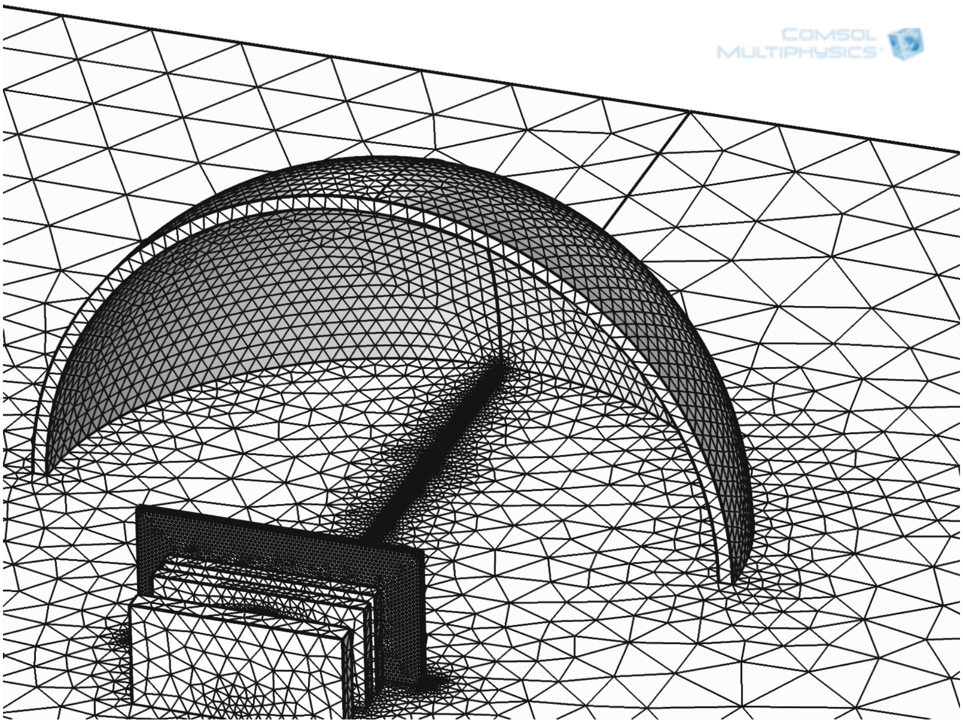

Figure 6.13: Shows variations in the meshing of one of the COMSOL models.

The *Charged Particle Tracing (cpt)* study type was used to simulate the particle trajectories. The only force that was added to the model was the *Electric Force*, which is specified by the electric potential previously solved for in the es-study type. The magnetic part of the Lorentz was omitted. It is possible to add other effects to the model, such as space charge effects and particle-particle interaction, but this was omitted. The electrons were released from the filament and the particle trajectories were calculated at discrete time steps.

Chapter 7

Experiments and Simulations

This chapter goes through the experiments and computer simulations conducted during the thesis, and presents the most important results. The experiments were thoroughly recorded in a laboratory journal which might contain information, results, simulations and pictures showing the alignment of the gun elements omitted here. The experiments are presented in chronological order with the title being the same experiment number as used in the laboratory journal. As this chapter is quite extensive the reader who is in a hurry might consider only reading Section 7.2, 7.6, 7.7 and 7.9.

All the experiments were conducted with the filament described in Chapter 5, unless otherwise stated. The filament was usually replaced with a fresh filament between each experiment as the filament characteristics changed during testing. This could lead to differences in the electron gun performance due to variation in the filament production. If not otherwise stated, the voltage on the Faraday cup was set to follow the voltage on the last electrode to avoid creating an electric field between the gun and the Faraday cup. The dimensions given are approximate numbers taken with a microscope and a ruler. Positive bias polarity was used in most of the experiments as this would be more convenient to implement in the electronics for CubeSTAR.

7.1 Filament Characteristics

Introduction

The purpose of this experiment was to characterise the filament IV-curve, and estimate the filament temperature.

Experimental Methods

The IV-curve presented here was measured from the filament assembled in prototype 2c during experiment no. 13. The filament voltage was swept from 0 to 4 V with a step-size of 0.1 V to obtain the curve. A sweep was also performed from 0 to 20 mV with a step-size of 1 mV to obtain a detailed view of this region. If these points fit on a linear curve, it will give the room temperature resistance of the filament. The temperature of the filament is estimated by using Equation 4.3 in Chapter 4. It is assumed that the filament is pure tungsten with a Temperature Coefficient of Resistance of 4500 (ppm). It is furthermore assumed a linear relationship between the temperature and the change in resistance. The temperature of the filament for the voltages below 20 mV is assumed to be 20 °C, and the resistance at room temperature is given by the resistance of the filament in this region.

Results

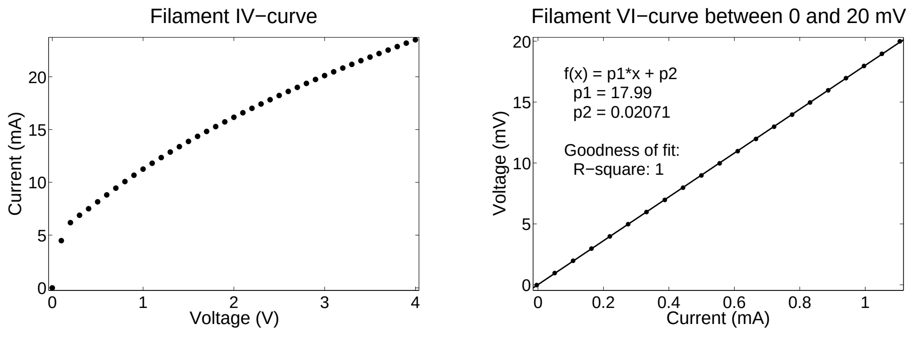

(a) **(b)**

Figure 7.1: Shows the characteristics of the filament used in experiment no. 13. The same type of filament was used for the other experiments as well. Figure (a) shows the IV-curve of the filament while (b) shows a detailed view of the IV-curve close to 0V

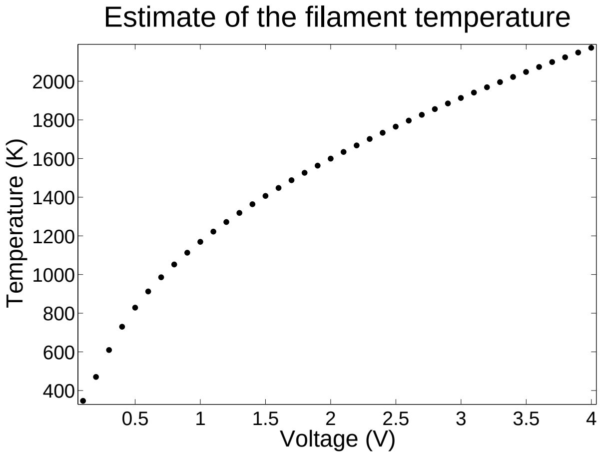

Figure 7.2: Shows an estimate of the filament temperature based on the results obtained in Figure 7.1.

Discussion

It is seen in Figure 7.1 that the room temperature resistance of the filament is 18 Ω, and that the change in resistance is non-linear especially in the low temperature region. At higher voltages, and hence temperatures, the IV-curve becomes more linear. There is a large uncertainty associated with the estimate of the filament temperature, and this result should only be regarded as a rough estimate. Since the material used in the filament is not known, the TCR of 4500 (ppm) might be wrong and, as stated in the theory chapter, the linear relationship between temperature and change in resistance might also not be valid at the higher temperatures. In addition to this comes the uncertainties associated with the measurements of the IV-curve, including test lead resistances. According to the rough estimate performed here the temperature of the filament is about 1900 K during nominal operation at 3 V. At 4 V the temperature has increased to about 2200 K.

7.2 Experiment no. 1 - Emission Current

Introduction

The purpose of this experiment was to investigate the emission current of the filament with the front-facing side of the anode placed 1.5 mm in front of the filament. By emission current we mean the total amount of current that is emitted from the filament. The reason for characterizing the emission current is to determine the maximum current the electron gun can deliver, as some current will be collected by the various gun elements like the electrodes. The emission current can be compared to the overall beam current and electrode currents in later experiments. By beam current we mean the current that constitute the beam after exiting the gun and is collected by the Faraday cup.

Experimental Method

The device under test consisted of an apertureless anode, placed in the second position in prototype 1, together with a fresh filament. This configuration leaves about 1.5 mm between the front-facing side of the anode and the tip of the filament. The pressure during the experiment was approximately $1 \cdot 10^{-6}$ torr. Three measurements were taken at each anode voltage during the anode sweep and averaged to obtained the measurements in Figure 7.4.

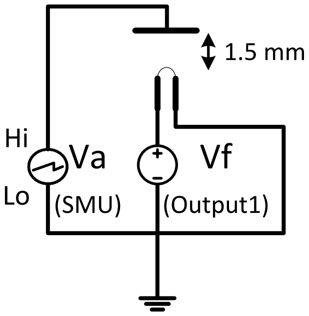

Figure 7.3: Shows the setup of experiment no. 1. The anode was connected to the SMU in the experiment, while output 1 on the PS powered the filament.

Results

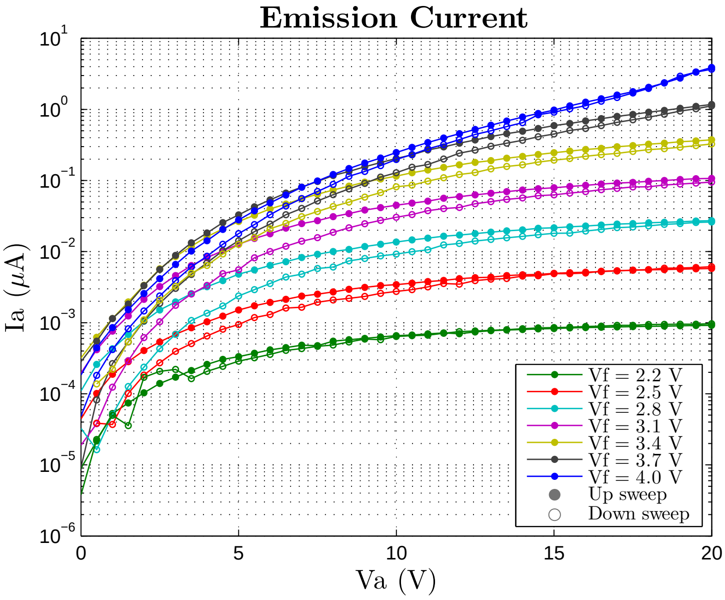

Figure 7.4: Shows the emission current as a function of anode voltage for different filament voltages.

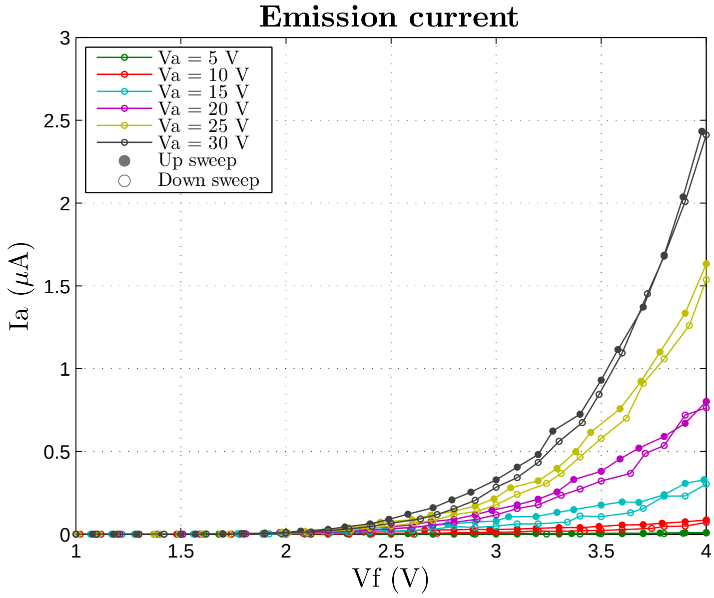

Figure 7.5: Shows the emission current as a function of filament voltage for different anode voltages.

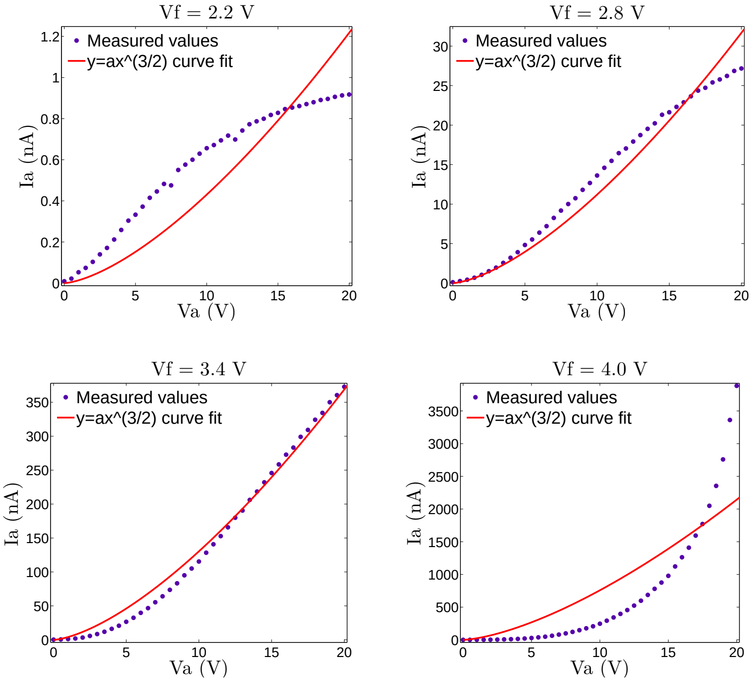

Figure 7.6: Shows the emission current for a selected number of filament voltages, with a curve fit on the form of Child's law.

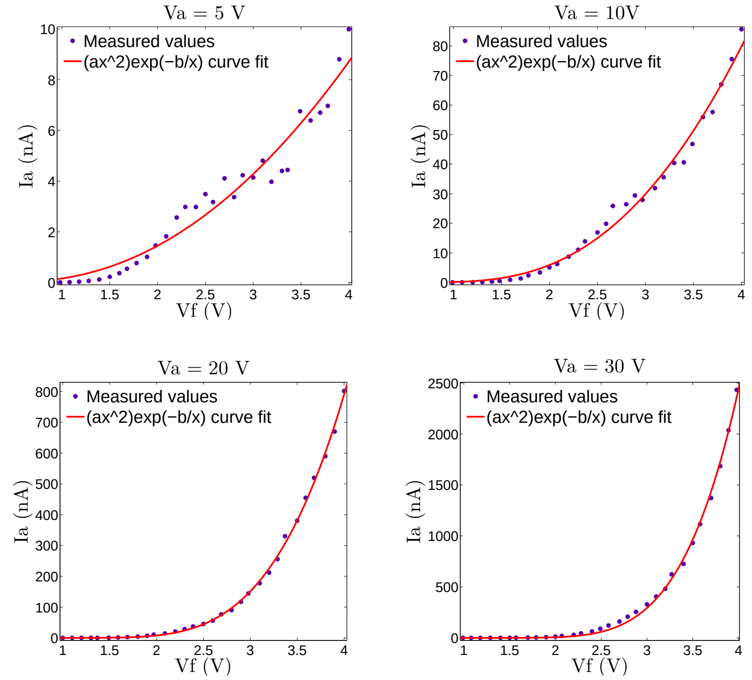

Figure 7.7: Shows the emission current for a selected number of anode voltages, with a curve fit on the form of Richardon's equation.

Discussion

It is seen in Figure 7.4 and Figure 7.5 that the emission current depends on both the filament voltage and the anode voltage, as expected. The total emission current from the filament at its normal rating is however, below what is necessary to control the spacecraft potential of CubeSTAR. By increasing the filament voltage to 4 V, with a power consumption just below 100 mW, an emission current in the desirable 0.5 - 5 μA range is obtained. Increasing the filament voltage above its ratings drastically reduces the lifetime of the filament, and the filament is clearly not optimal. It was decided to use the filament further in the experimental process in lack of a better alternative at that moment. Clearly, emission from the entire filament must be utilized to achieve the desired beam current with such low power consumption, in contrast to many electron gun designs which only uses emission from the very tip of the filament.

A noticeable decrease in emission current is seen by comparing the value for Va = 20 V and Vf = 4 V in Figure 7.4 and Figure 7.5. The measurements in the latter figure was obtained 1.5 hours later into the testing than those obtained in the first figure. This trend was also observed for later anode sweeps taken during the experiments which is not presented here.

In Figure 7.6 a curve on the form $y = ax^{3/2}$ has been fitted to the graphs using Matlab's curve fitting tool. This is a simplified equation of Child's law with all the different constants embedded into one. It is seen in the upper figures that for a small filament voltage, and hence low emission current, the current seems to saturate for high anode voltages and the diode enters the temperature limited region[1]. At Vf = 3.4 V the measured currents seem to vary as the three-halves power of the anode voltage. For the higher emission current at Vf = 4.0 V the measured currents follows a more exponential curve. The deviations from Child's law can be explained with the fact that this is not at all an ideal diode as described in the theory section. It is not an infinite, parallel diode. In fact, the anode is a square plate with finite dimensions, while the cathode has the shape of a thin, curved cylinder. Only one side of the filament is faced towards the anode, which means that emission from the rear-facing side happens in the opposite direction of the anode. Higher electric fields are then necessary to draw these electrons in the correct direction.

In Figure 7.7 a curve on the form $y = ax^2e^{-b/x}$ has been fitted to the graphs using Matlab's curve fitting tool. This is a simplified equation of Richardson's equation, with the temperature being replaced by the filament voltage. It is seen that the measured values follows the fitted curve quite

---

[1] The behavior of an ideal diode is shown in Figure 4.4b

well, especially for the higher anode voltages. It is not seen, however, that the diode enters the space charge limited region for smaller anode voltages and higher filament voltages as one might expect[2]. This could be due to the increasing initial velocities of the electrons for higher filament voltages, and hence higher temperatures. The curve fitting should be applied to the temperature rather than the voltage. However, as Figure 7.2 shows, the relationship between the voltage and the temperature is close to linear. The curve fit of the current as a function of voltage will therefore give an approximation to Richardson's law.

The testing left a mark in the centre of the copperplate, as seen in Figure 7.8. This mark was not noticed prior to the test. Whether the mark is due to the electron beam itself or the heat is not known.

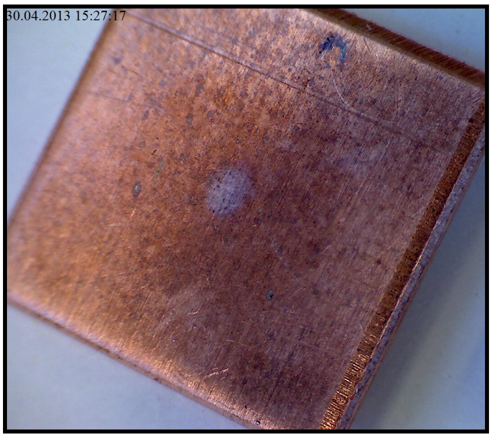

Figure 7.8: Shows a mark in the anode which was not noticed prior to the test. It is not known if was the electron beam or the heat from the filament that caused the mark.

---

[2] The behavior of an ideal diode is shown in Figure 4.4c

7.3 Experiment no. 2, 3 and 4 - Diode e-gun

Introduction

The purpose of these experiments was to test a very simplified electron gun, consisting of only the filament and an apertured anode.

Experimental Method

These experiments took place over three vacuum pump-downs, and the vacuum pressure during those tests was between $2 \cdot 10^{-6}$ torr and $7 \cdot 10^{-7}$ torr. An aperture with a diameter of 2 mm, which is about twice width of the distance between the filament joints[3], was drilled in the centre of the anode in an attempt to utilize the entire emission current. The thickness of the copper electrode was 1 mm. The electrical configuration of the experiments when the beam current was measured is shown in Figure 7.9c. To measure the anode current, the position of the SMU and OUT2 was switched and the test-sweeps repeated. Figure 7.9b and Figure 7.9a show the electron gun mounted with the anode placed 1.5 mm in front of the filament.

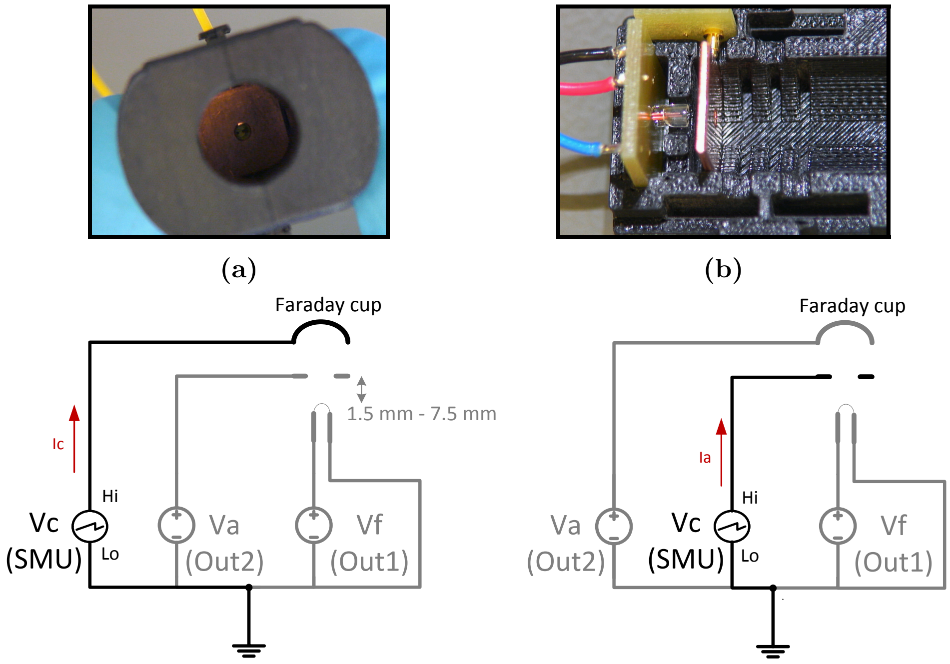

(a) (b)

(c)

Figure 7.9: Shows the DUT in (a) and (b), while (c) shows the setup of the experiment. Due to lack of measurement equipment the beam current and anode current had to be measured in two separate test-runs.

---

[3] See Figure 5.2 for the dimensions of the filament

Experiment no. 2 was conducted with the same filament used in experiment no. 1, and the anode placed at the same position leaving a gap of 1.5 mm between the anode and filament. In this experiment the prototype was placed on the back of the ledge in the test fixture and the Faraday cup was placed a distance apart from the ledge. This is shown in Figure 7.10.

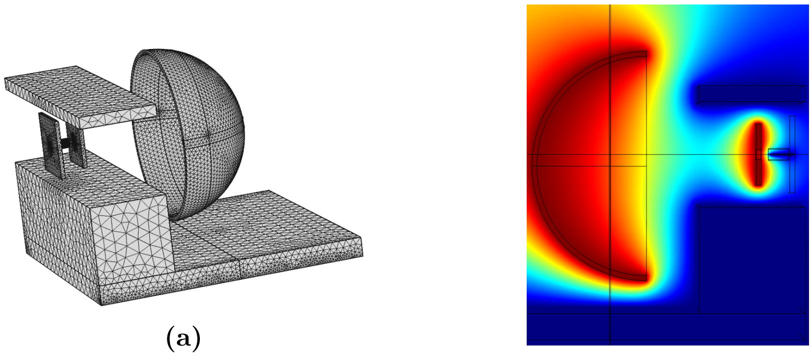

(a)

(b)

Figure 7.10: Shows a COMSOL simulation of the setup in experiment no. 2. (a) shows the geometry of the setup, while (b) shows the potential distribution in one plane. The test fixture and the filament was at 0V, while the anode and the Faraday cup was biased to +30 V as indicated by the red colour.

Experiment no. 3 was conducted with a fresh filament and the anode kept at the same position. The electron gun was placed on the front of the ledge in the test fixture and the Faraday cup was placed close to the ledge. This is shown in Figure 7.11.

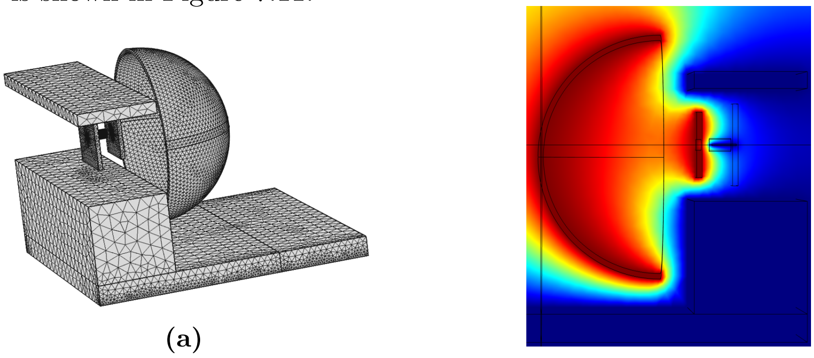

(a)

(b)

Figure 7.11: Shows a COMSOL simulation of the setup in experiment no. 3. (a) shows the geometry of the setup while (b) shows the potential distribution in one plane. The test fixture and the filament was at 0V, while the anode and the Faraday cup was biased to +30 V as indicated by the red colour.

Experiment no. 4 was conducted with the same filament as in experiment no. 3, but with the anode placed in the fourth position in prototype 1 leaving a gap of 7.5 mm. The electron gun was placed in a similar way as in Figure 7.11.

Results

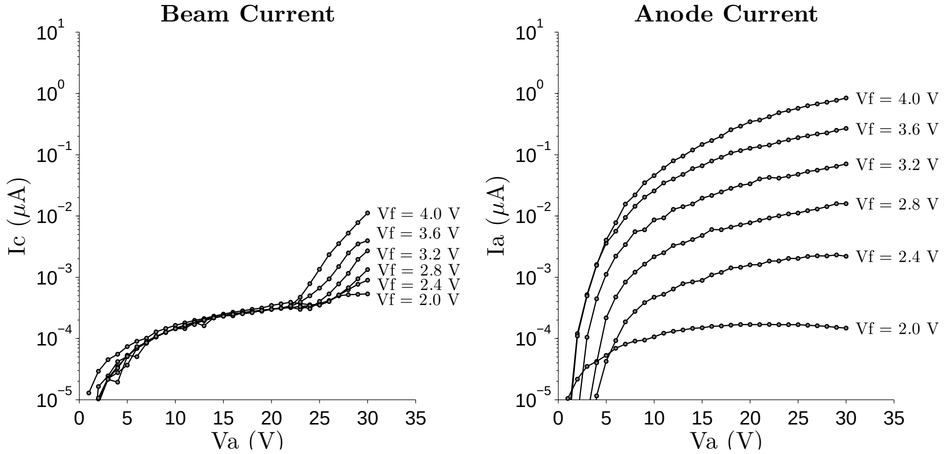

(a) Experiment no. 2 - 1.5 mm between filament and anode.

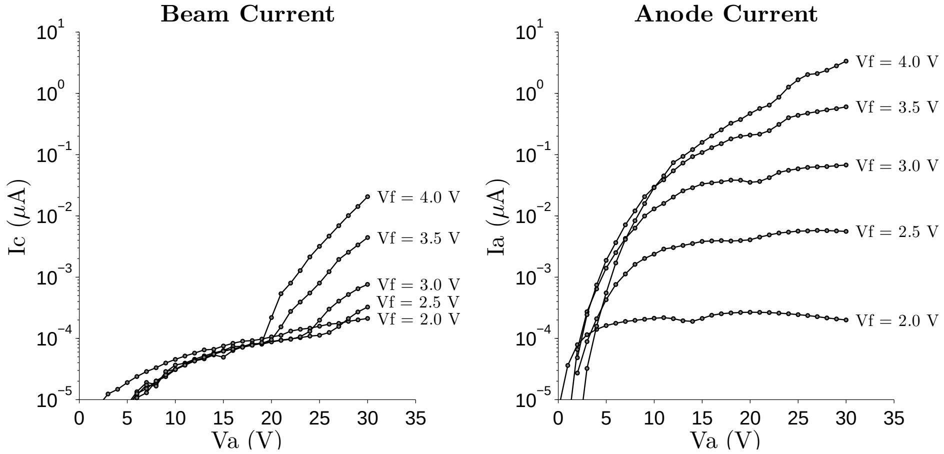

(b) Experiment no. 3 - 1.5 mm between filament and anode.

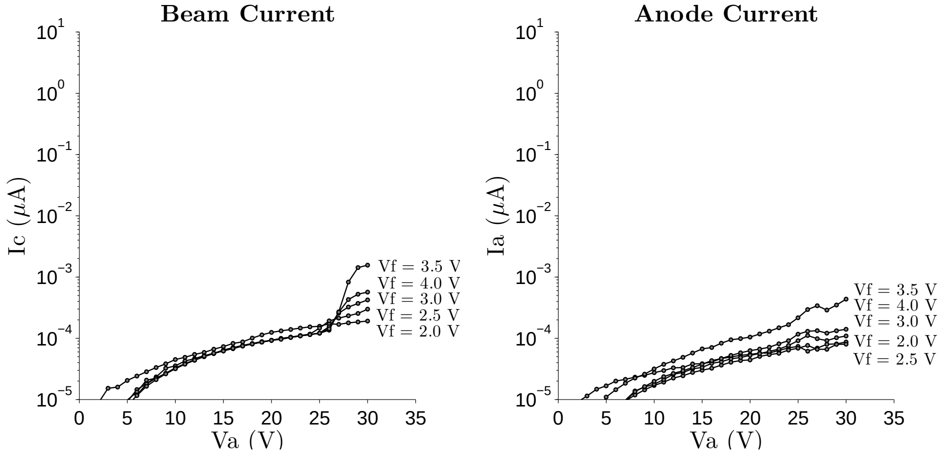

(c) Experiment no. 4 - 7.5 mm between filament and anode.

Figure 7.12: Shows the measured current from the Faraday cup, denoted as the beam current, and the current collected from the anode, denoted as the anode current. Three measurements were taken at each anode voltage and averaged to obtain the graph in (a), while five measurements were take to obtained the graphs in (b) and (c).

Discussion

It is seen in Figure 7.12a and Figure 7.12b that almost all the current was collected at the anode when the distance between the anode and filament was 1.5 mm. The current measured by the Faraday cup was zero for low acceleration voltages, but increased for higher voltages. The next observation that is made is that the overall measured current in Figure 7.12a is less than the emission current presented in Section 7.2. The overall current at Vf = 4.0 V and Va = 20 V is ten times less than the emission current shown in Figure 7.4 and slightly less than the current shown in Figure 7.5. The loss in overall measured current with respect to the emission current from experiment no. 1 could be due to:

- Lowered electrical field near the cathode due to the aperture. This is illustrated in Figure 4.6 in Chapter 4 where in (d) the electric field strength is lowered due to the aperture.
- The filament had degenerated even more since the last experiment. It was observed in experiment no. 1 that the emission current was lower after the electron gun had been run for a while.
- Some of the electrons had diverged into the non-conductive housing before reaching the Faraday cup.
- The electrical field caused by the test fixture prevented the beam from reaching the Faraday cup, as seen in Figure 7.10.

It was therefore decided to repeat the experiment with a fresh filament, and placing the electron gun closer to the Faraday cup as seen in Figure 7.11. The polarity of the biasing voltage could also have been switched, to avoid disturbance of the electrical field by the fixture. It is seen in Figure 7.12b that the overall current is now slightly higher at Vf = 4.0 V and Va = 20 V, but the beam current is still very low. All the electrons diverge into the anode. It is seen in Figure 4.6 (a) and (b) in Chapter 4 that the diverging effect of the aperture has more effect on the electron trajectory when the anode is placed closer to the cathode. It was therefore decided to repeat the experiment, but placing the anode 7.5 mm in front of the anode instead of 1.5 mm. Poorly alignment of the filament and the aperture could also be the reason why the electrons was collected at the anode. However, optical inspections of the electron gun showed fairly good alignment.

It is seen in Figure 7.12c that the overall current is now even lower than for the two previous experiments. There is no measurable current at the anode, and the beam current is barely measurable at the highest anode voltages. The reason for this is likely due to the lower electric field strength caused by the increased distance between the electrodes. Influence of the potential of the test fixture or influence by the Earh's magnetic field could be another explanation.

7.4 Experiment no. 5 and 6 - Triode e-gun

Introduction

These experiments were conducted in an attempt to prevent the beam from being collected at the anode, by creating an initial focusing of the electron beam. The approach was to insert a control electrode, similar to the Wehnelt cylinder described in Section 4.5.

Experimental Method

These experiments took place over 2 vacuum pump-downs, and the vacuum pressure was roughly $7 \cdot 10^{-7}$ torr for both experiments. A 0.7 mm thick copperplate with an aperture measuring 2 mm in diameter was placed in the first position in prototype 1. The anode, still with an aperture measuring 2 mm in diameter, was placed in the second position. This configuration leaves a gap of 0.8 mm between the front-facing side of the control electrode and the rear-facing side of the anode. The distance between the filament and the first electrode is ideally 0 mm. The experimental setup is shown in Figure 7.13.

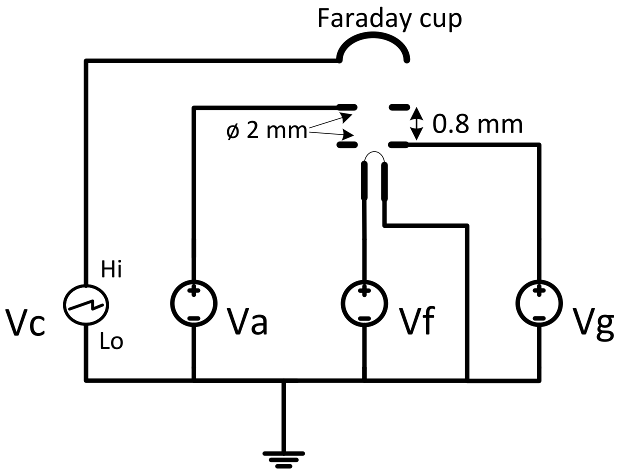

Figure 7.13: Shows the setup of experiment no. 5 when the beam current was measured. The setup was similar for experiment no. 6, expect for the Faraday cup which was replaced with a copper electrode. The beam current and anode current had to be obtained in different test-runs as illustrated in Figure 7.9c.

Experiment 5 was conducted with the electron gun placed on the front of the ledge in the test fixture. The beam current was measured from the Faraday cup which was placed close to the ledge. This was done to minimize the influence of the test fixture's ground potential, as described in Section 7.3. The DUT used in this experiment is shown in Figure 7.14. A fresh filament was used, and care was taken to align it with the apertures in the electrodes, as seen in Figure 7.14b.

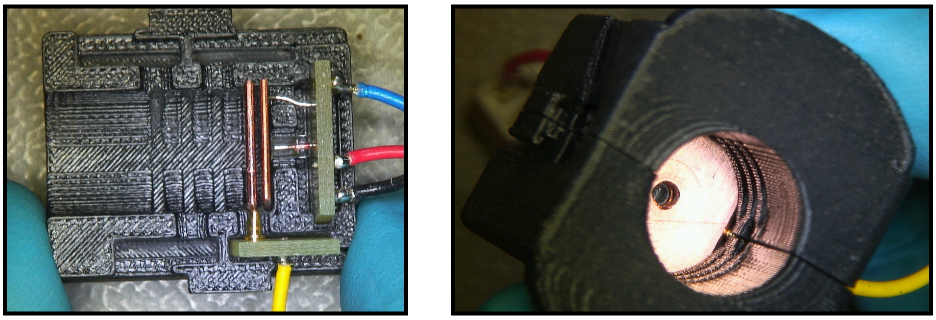

(a) **(b)**

Figure 7.14: Shows the DUT used in experiment no. 5.

Exsperiment 6 was conducted with the beam current being measured from an apertureless electrode placed in the third position in the prototype. This configuration leaves a gap of 2 mm between the anode and the electrode referred to as the collector plate. The DUT used in experiment no. 6 is shown in Figure 7.15 (a) with a 2D plot of the equipotential contours near the filament obtained with COMSOL shown in (b). The filament which was used was the same filament from experiment no. 5.

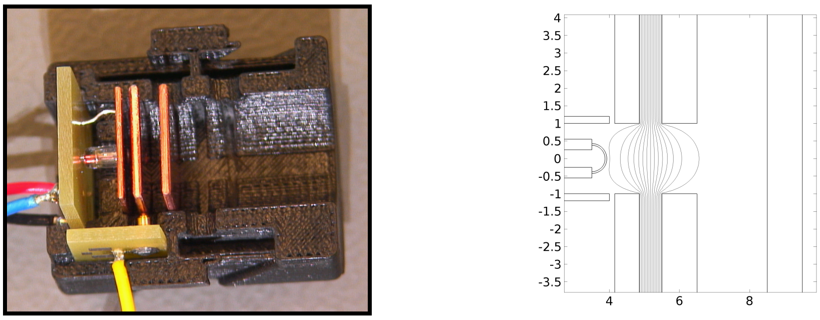

(a) **(b)**

Figure 7.15: Shows the DUT used in experiment no. 6. The spring connector to the collector plate is not mounted in figure (a). A 2D equipotential contour plot of a COMSOL simulation is shown in (b) where the geometry was made to be in accordance to the physical DUT shown in (a). In (b) the filament is at 0V, while the anode and collector plate is at +30 V.

Results

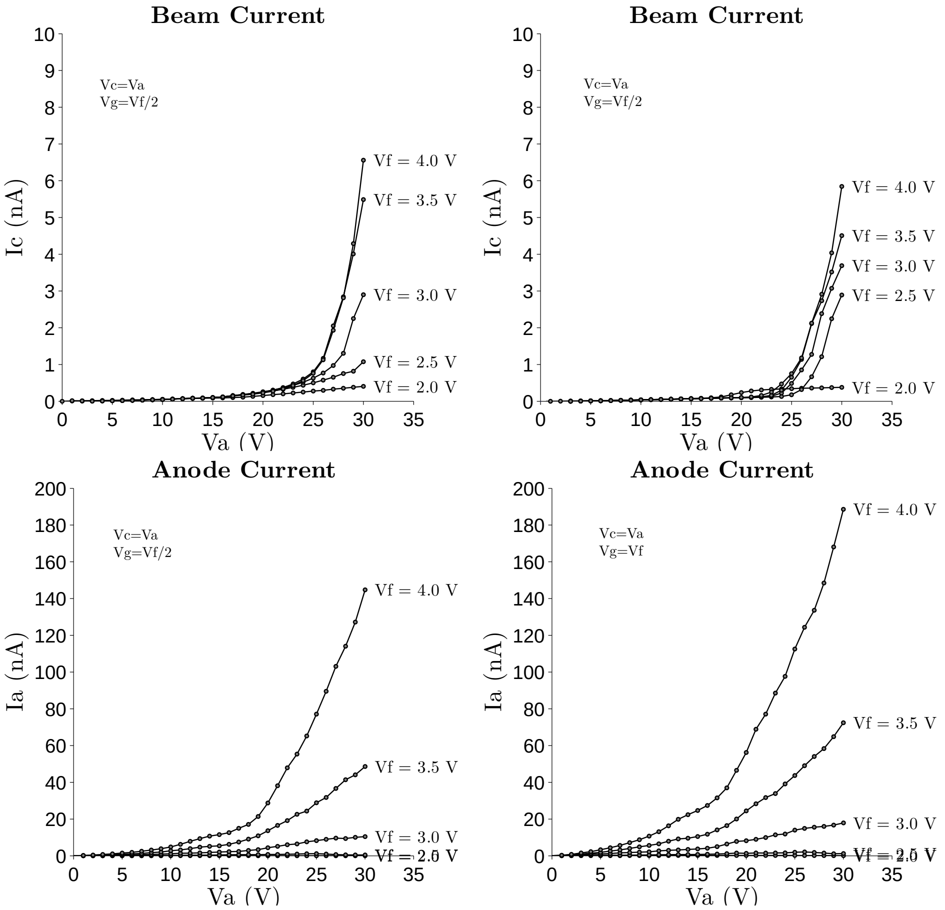

(a) Experiment no. 5.

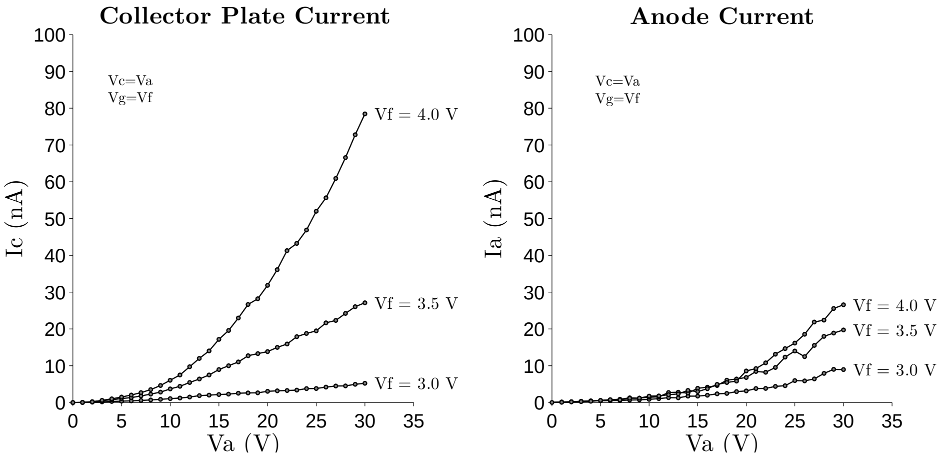

(b) Experiment no. 6.

Figure 7.16: Shows measured current from experiment no. 5 and 6. Three measurements were taken and averaged at each anode voltage to obtain the graphs. The lower right figure were obtained with only one measurement at each voltage.

Discussion

It is seen in Figure 7.16a that the overall measured current in experiment no. 5 is much lower than in the previous experiments. By overall current we mean the current from both the Faraday cup and the anode. This can be explained by the lowered electrical field at the filament due to the insertion of the control electrode, as seen in Figure 7.15b. It is observed that the anode current is slightly higher for Vg = Vf than it is for Vg = Vf/2. The current from the control electrode was measured in experiment no. 5, with a maximum value of 3 nA at Vf = 4 V, Vg = Vf and Va = 30 V.

It is seen in Figure 7.16b that the overall measured current in experiment no. 6 is about 50 nA lower than it was measured for the same parameters in experiment no. 5. This could be due to degeneration of the filament as observed earlier. It is further seen that less current is collected at the anode, and more collected at the collector plate. A reason for this might be that the collector plate, which was at the same potential as the anode, prevents the beam from diverging into the aperture.

Due to the low bias voltages available, it was concluded that a design similar to the Wehnelt cylinder was inappropriate for the electron gun. Too much current of the available emission current is not utilized. In one of the sweeps, whose results are omitted here, Vg was set to be Vf+1V. This resulted in a slightly higher Faraday cup current of roughly 26 nA at Vc = Va, Vf = 4 V and Va = 30 V. However, it was led to believe that this would increase the diverging of the beam as well, and hence another approach was taken.

7.5 Experiment no. 7 and 8 - Focus e-gun

Introduction

These experiments were conducted in an attempt to prevent the beam from being collected at the anode, by increasing the aperture in the anode.

Experimental Method

The experiments took place over 2 vacuum pump-downs. It is only experiment no. 7 that is presented here, as the results from experiment no. 8 was not saved. Experiment no. 8 was furthermore only a repetition of experiment no. 7. The vacuum pressure in experiment no. 7 was roughly $5.5 \cdot 10^{-7}$ torr. An aperture with a diameter of 3 mm was drilled in the centre of the anode, and placed in the second position of prototype 1. To prevent the beam from diverging into the non-conductive housing behind the anode, an electrode configuration similar to the Einzel lens was implemented. Two copper plates, both having an aperture with a diameter of 6 mm, was placed in the third and fifth position respectively. The electrical configuration as well as the mechanical configuration for the experiment is shown in Figure 7.17. A fresh filament was used, in addition to a new printed wiring board (PWB) where the filament was mounted. This could lead to a different alignment of the filament, as the PWBs were manually adapted to the slots in the prototype. The DUT is shown in Figure 7.18 while a COMSOL simulation of the potential distribution and the particle trajectory is shown in 7.19. It is seen in Figure 7.19a that the particles diverge after the aperture in the anode, but the einzel lens configuration focuses the beam back towards the symmetry axis.

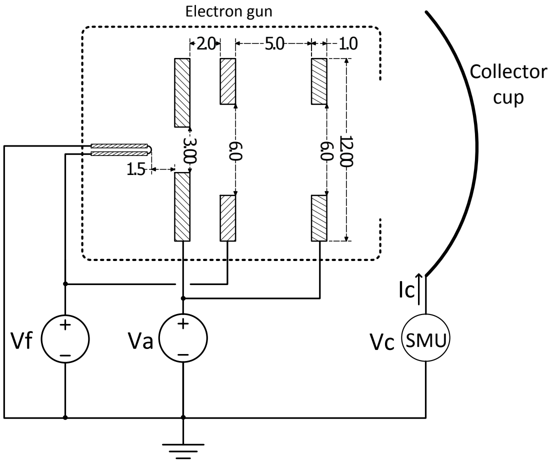

Figure 7.17: Shows the electrical and the mechanical configuration of experiment no. 7 and 8. The dimensions of the gun elements are given in mm.

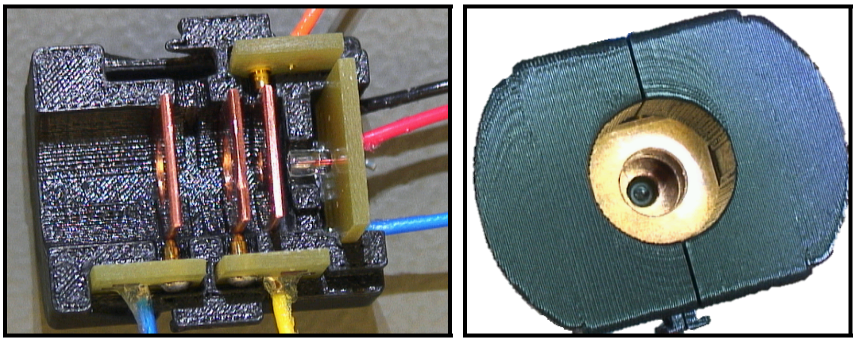

(a) (b)

Figure 7.18: Shows the DUT used in experiment no. 7 and 8.

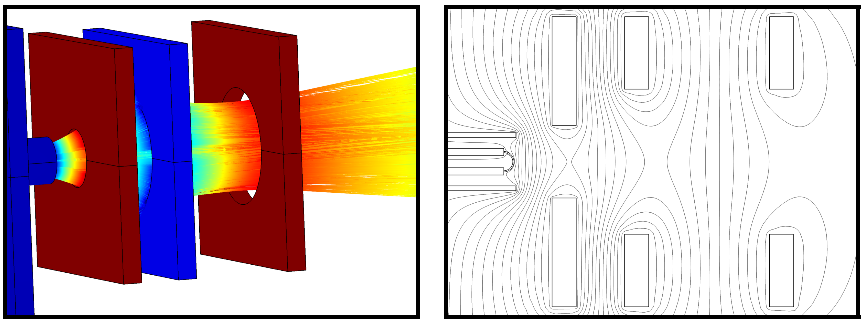

(a) (b)

Figure 7.19: Shows a COMSOL simulation of the electrode configuration. In (a) ten thousand particles are released from the filament with zero initial kinetic energy and tracked with the particle tracing module. It should be noted that the electric current module was used to incorporate the potential drop over the filament. As it is seen in the equipotential contour plot in (b) and also in (a), this resulted in a 0V potential on the insulating PWB and glass bulb which is not correct. The filament is at 0 V and +4 V, the middle electrode is at +4 V, while the two other electrodes are at +40 V.

Results

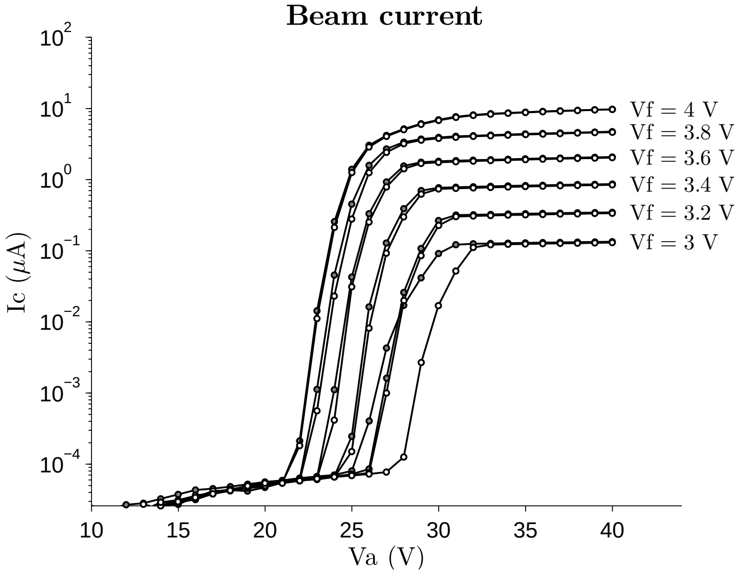

Figure 7.20: Shows the measured beam current as a function of anode voltage for different filament voltages. Five measurements were taken and averaged at each anode voltage to obtain the graphs. The filled circles indicate the up sweep measurements while unfilled circles indicates the down sweep measurements.

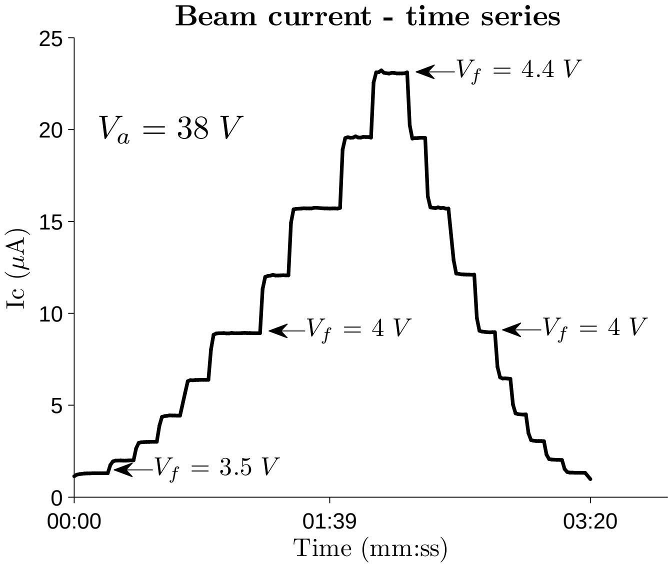

Figure 7.21: Shows the measured beam current as a function of different discrete changes in filament voltage. A measurement was taken every second.

Discussion

It is seen in Figure 7.20 that, similar to experiments 2 to 5, there are no significant current measured at the collector cup for lower voltages. However, at above roughly 20 V, depending on the filament voltage, the beam current drastically increases until it reaches a value similar to the emission current obtained earlier. The reason for this sudden increase in current is thought to be either due to the diverging effect of the aperture as discussed in the theory section, deformation of the filament or insertion of the two electrodes behind the anode. By referring to Figure 4.6 in the theory chapter it might be that increasing the anode voltage, and hence the kinetic energy of the electrons before the effect of the aperture takes place, is enough for the electrons to avoid being drawn into the anode. This will result in a rapid increase in current which might imply that, if higher anode voltages were used in the previous experiments, the beam current would have increased rapidly there too. Figure 7.21 shows that the beam current can be varied in discrete steps by adjusting the filament voltage. The dynamic range of the electron gun is, however, not good if it is to be controlled with the anode voltage.

7.6 Experiment no. 9 - Test of Prototype 2

Introduction

The purpose of this experiment was to test prototype 2, and investigate whether or not it is possible to accelerate electrons through vias in printed wiring boards. The results are to be compared to those obtained during the last experiments.

Experimental Method

This experiment took place over two vacuum pump-downs. The pressure was not known, as the vacuum gauge was missing, however it should be similar to those obtained earlier. Two electron guns were assembled and tested for each pump-down. In the first pump-down, prototype 2a was connected with an anode with an aperture of 3 mm in diameter, while prototype 2b was connected with an apertureless anode. Both with fresh filaments. In the second pump-down the anodes were switched, and the filaments kept. By doing so, both prototypes were tested for the emission current as well as the beam current. Both prototypes were assembled with an electrode, referred to as the supporting electrode. The aperture of this supporting electrode is 2.5 mm in diameter, which is 0.1 mm wider than the diameter of the glass bulb. Its purpose is to align the filament with the symmetry axis of the electron gun, and to mechanically protect the glass bulb and filament. The supporting electrode is placed such that the filament is protruding out of the electrode, and the electrical field strength is therefore not lowered as it was in experiment no. 5 and 6. A hypothesis is that the presence of the ground potential on the supporting electrode will make a more uniform electric field between the filament and the anode. The setup for the experiment is shown in Figure 7.22.

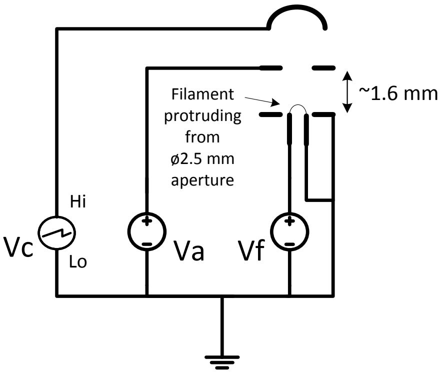

Figure 7.22: Shows the setup of experiment no. 9. The beam current and anode current had to be obtained in different test-runs as illustrated in Figure 7.9c.

Prototype 2a is shown in Figure 7.23, where in (a) the DUT is configured with an apertureless anode and in (b) with an apertured anode with a diameter of 3 mm. It is seen in (a) that the filament is protruding out of the supporting electrode. The distance between the supporting electrode and the anode is roughly 1.6 mm, while the distance between the tip of the filament and the anode is roughly 1.0 mm.

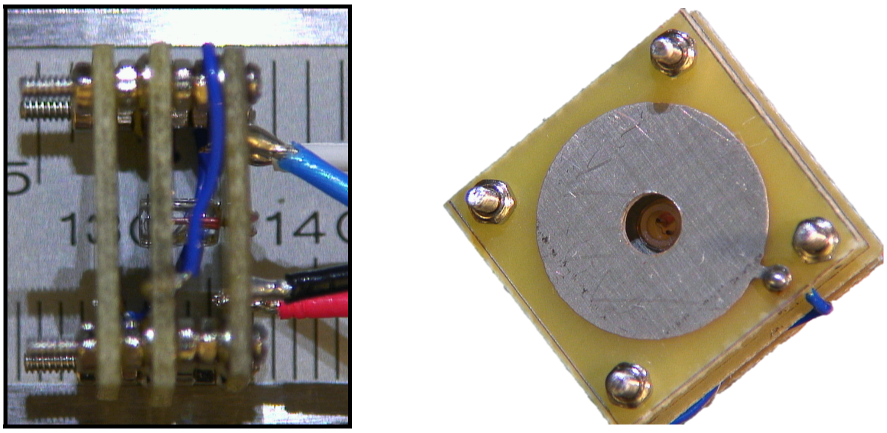

(a) **(b)**

Figure 7.23: Shows prototype 2a configured as a diode in (a) and as an electron gun in (b). The electrodes are manufactured from printed wiring boards (PWBs).

A COMSOL simulation of the electron gun configuration is shown in Figure 7.24. In (a), one thousand particles were released from the filament with zero initial velocity and accelerated by the electric potential shown in (b). One half of the filament is at 0 V while the other half is at +4 V to approximate the potential drop. The supporting electrode is at 0 V, and the anode at +35 V. The copper layers are in the simulation 100 μm thick instead of 35 μm, as it is in the DUT.

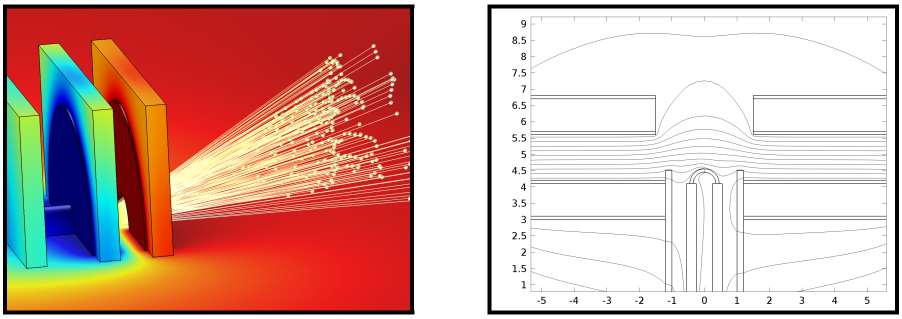

(a) **(b)**

Figure 7.24: Shows the particle trajectories in (a), while (b) shows an equipotential contour plot of the COMSOL simulation.

Results

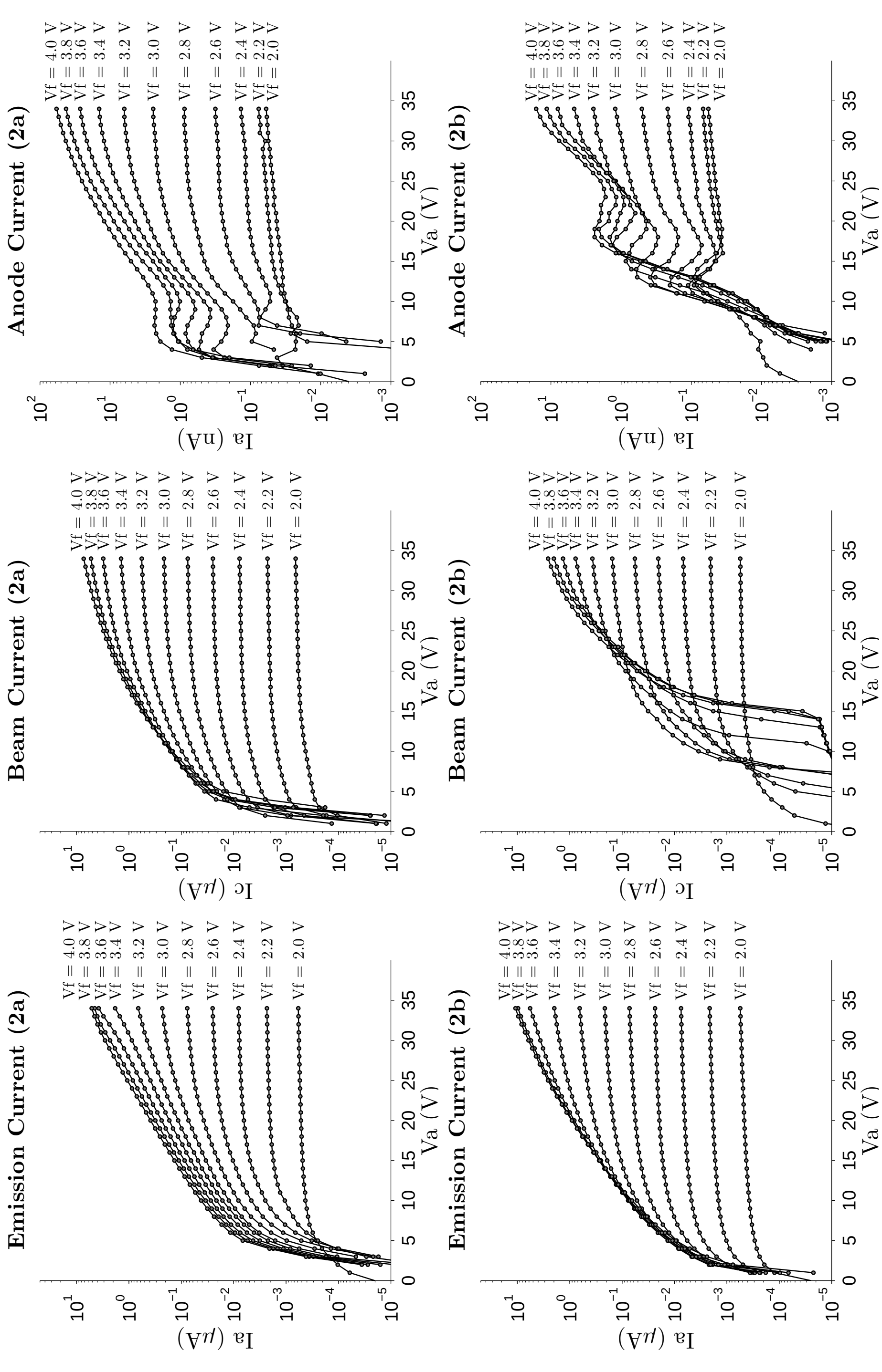

Figure 7.25: Shows the measured current from experiment no. 9. Three measurements were taken and averaged at each anode voltage to obtain the graphs. The emission current for 2b was obtained during the first pump-down, while the beam- and anode current was obtained during the second pump-down. 2a followed the reversed order.

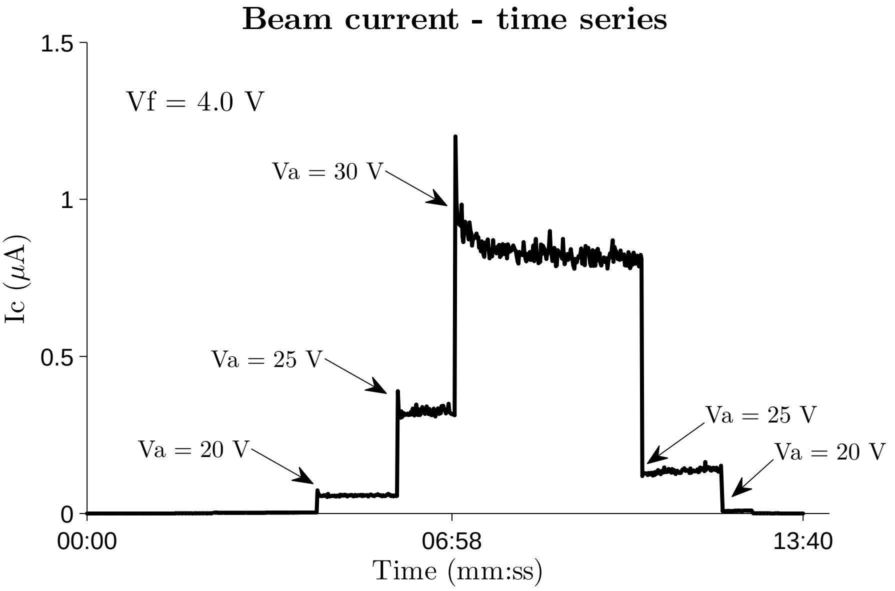

Figure 7.26: Shows the measured beam current as response to various discrete changes in anode voltages for prototype 2b.

Discussions

This experiment has shown that it is possible to accelerate electrons through vias in printed wiring boards, despite having non-plated through-holes and coarse accuracy on the positioning of the apertures. It is seen in Figure 7.25 that the dynamic range of prototype 2a is much better than the dynamic range obtained in experiment no. 7 presented in Section 7.5. The reason for this was thought to be (1) the supporting electrode created a more uniform electric field between the anode and the filament or (2) the einzel lens used in experiment no. 7 may have suppressed the beam current at lower voltages.

However, as it is seen in the graph in Figure 7.25 with the title *(2b) Beam Current*, the dynamic range of prototype 2b suddenly gets worse for higher filament voltages during the anode sweep. The dynamic range for these highest filament voltages is similar, albeit not that low, to those obtained in experiment no. 7. It is further seen that the overall current measured for prototype 2b, that is both the beam current and the anode current, is lower than the obtained emission current. This is most likely because the emission current was obtained during the first pump-down while the overall current was obtained during the second pump-down. The current from the supporting electrode was measured to be below 0.1 nA, and can thus be ignored.

A trend that was seen throughout all the experiments was that the filament got deformed when operated in the vacuum chamber. A close up of the filament used in prototype 2a before and after testing is shown in Figure 7.27 (a) and (b) respectively. It is seen that the filament has been deformed, but most part of the filament is, however, still protruding out of the supporting electrode. The filament in prototype 2b had sagged even more into the aperture than prototype 2a.

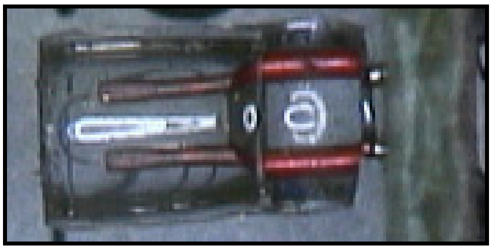

(a) Before the experiment.

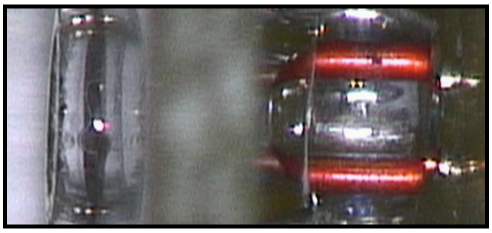

(b) After the experiment.

Figure 7.27: Shows the filament used in prototype 2a before the test in (a), and after the test in (b). The testing causes the filament to deform and sag into the aperture.

It is seen in Figure 7.26 that the measured beam current has a sharp spike during transition from a low anode voltage to a high anode voltage. It is furthermore seen that the current, when the anode voltage is decreased, is lower than it was when the anode voltage was increased. The current, however, seems to creep back to the same value that was measured during the up steps in anode voltage. This behavior was observed in later experiments as well with varying degrees of severity. The reason for this is thought to be charging of the insulating parts in the electron gun or a capacitive effect.

Another interesting observation is the wave-like shape of the anode current. This is thought to be due to the diverging effect of the aperture in the anode as explained previously. At lower anode voltages the electrons have lower kinetic energy when passing the anode, and hence they are more affected by the diverging effect of the aperture which causes a higher anode current. At higher voltages the electrons, which was previously drawn into the anode, have sufficient kinetic energy to get through the aperture.

7.7 Experiment no. 10 - Bias Polarity

Introduction

It was stated in Section 5.1 that the biasing electrodes of the electron gun should not interfere with the plasma, and not contribute to collecting more electrons to the spacecraft body. It was furthermore stated that the emitted electrons should have high kinetic energy. As it is more convenient electronically to operate the electron gun with positive voltages rather than negative voltages, this experiment was conducted to investigate whether or not the electron gun could operate on positive bias voltages on CubeSTAR, without affecting these parameters.

Integration to CubeSTAR The electron gun will be mounted to the top-panel on CubeSTAR using the four metal screws as illustrated in Figure 5.4 in Chapter 5. Two scenarios are possible:

- **The electron gun uses negative polarity.** This means that the electrons are accelerated from a negatively biased filament, with respect to frame ground, towards the anode which is connected directly to frame ground. Having the anode at the floating potential of the satellite means there will be no electric field between the anode and the CubeSTAR surfaces which is connected to frame ground.
- **The electron gun uses positive polarity.** This means that the electrons are accelerated from the filament, which is connected to frame ground, towards the anode which is biased positively with respect to the filament and frame ground. Having the anode at a higher potential than frame ground means there will be an electric field between the anode and the CubeSTAR surfaces connected to frame ground. This may potentially affect the electron beam.

If positive bias polarity is to be used, the positive bias of the anode should be shielded from the surrounding plasma. If not, the anode will act as Langmuir probe, and electrons will be collected to the spacecraft frame ground. As a result, the floating potential of the spacecraft will be lowered and a higher emitted electron beam current is necessary to counterbalance this effect. If the positive bias is shielded however, an electric field is created between the anode and the shield which may affect the electron gun performance, and there will be a compromise between the effect of the shield and the influence on the electron beam.

Experimental Method

Prototype 2a, with the same specifications as in the last experiment, was mounted on a 0.5 mm thick PWB whose purpose was to act as the CubeSTAR top panel. The layout for this top panel PWB is seen in Figure D.7 in Appendix D marked with the letter *a*. The PWB measures 40 × 40 mm and it has an aperture of 3 mm in the centre. The top electric is filled with a copper layer, which is connected to ground in the experimental setup. This ground layer will then act to shield out the positive potential on the anode, in addition to simulate the desired conductive surface on CubeSTAR. On the bottom electric there is an electrode similar to the electrodes in the electron gun. This electrode is connected to the anode voltage source. By doing so, there will only be a 0.50 mm gap between the anode and the CubeSTAR top panel acting as the shield. The electron gun mounted to the top panel is seen from various angles in Figure 7.28. The experimental setup is illustrated in Figure 7.29, where the thickness of the copper traces have been exaggerated for illustration purposes. The figure in (a) shows the configuration used for testing negative bias voltages, while the figure in (b) shows the configuration for positive bias voltages.

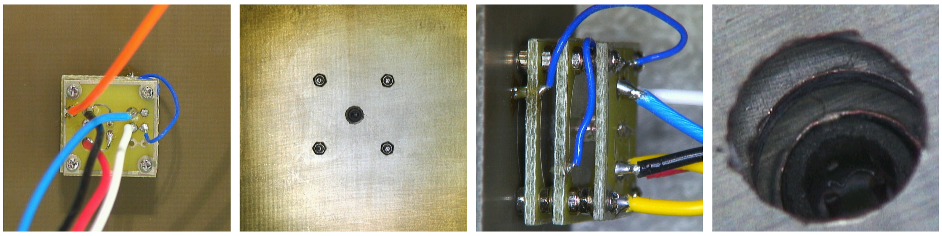

Figure 7.28: Shows the DUT mounted to the top panel from various angles.

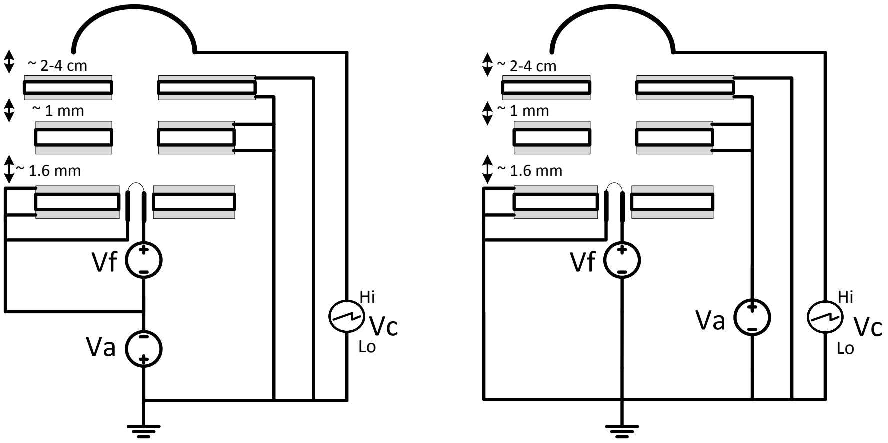

(a) **(b)**

Figure 7.29: (a) shows the setup for testing negative bias polarity while (b) shows the setup for testing positive bias polarity. The grey layers illustrates the copper traces on the PWB.

Results

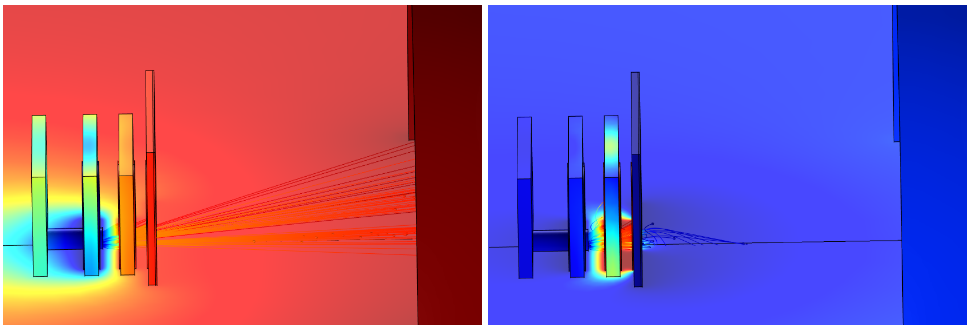

(a) Negative polarity **(b)** Positive polarity

Figure 7.30: Shows a COMSOL simulation performed on the electron gun configuration. In (a) the electrons are emitted from the filament, which is biased negatively to -30 and -26 V, and accelerated towards the anode which is at ground potential. The top electrode is too at 0V, while the Faraday cup shown to the right is at +5 V. In (b) the electrons are emitted from the filament, which is at 0 and 4V, and accelerated towards the anode at +30 V. The top electrode and the Faraday cup is still biased to 0 and +5 V, respectively. The top electrode is made smaller to ease computation. The colours show the potential distribution, with red indicating a higher potential than blue. The particles are colour coded in the same way.

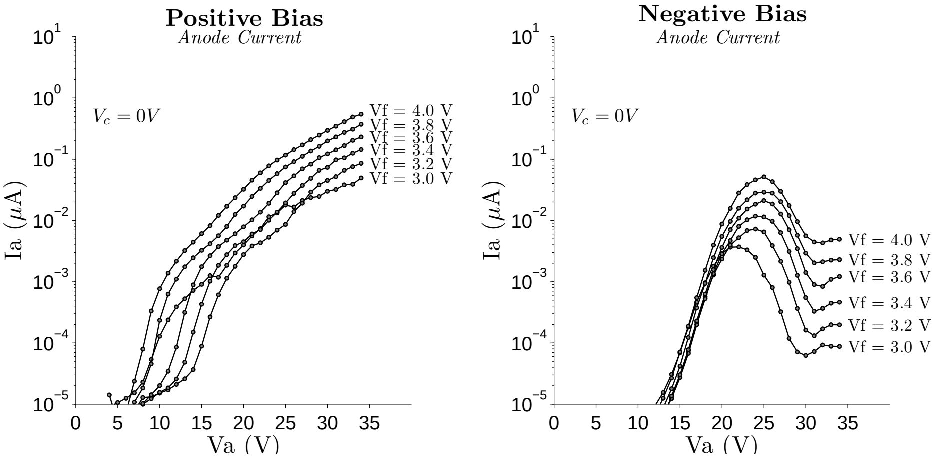

Figure 7.31: Shows the measured anode current for negative and positive bias polarity with the collector cup at 0V.

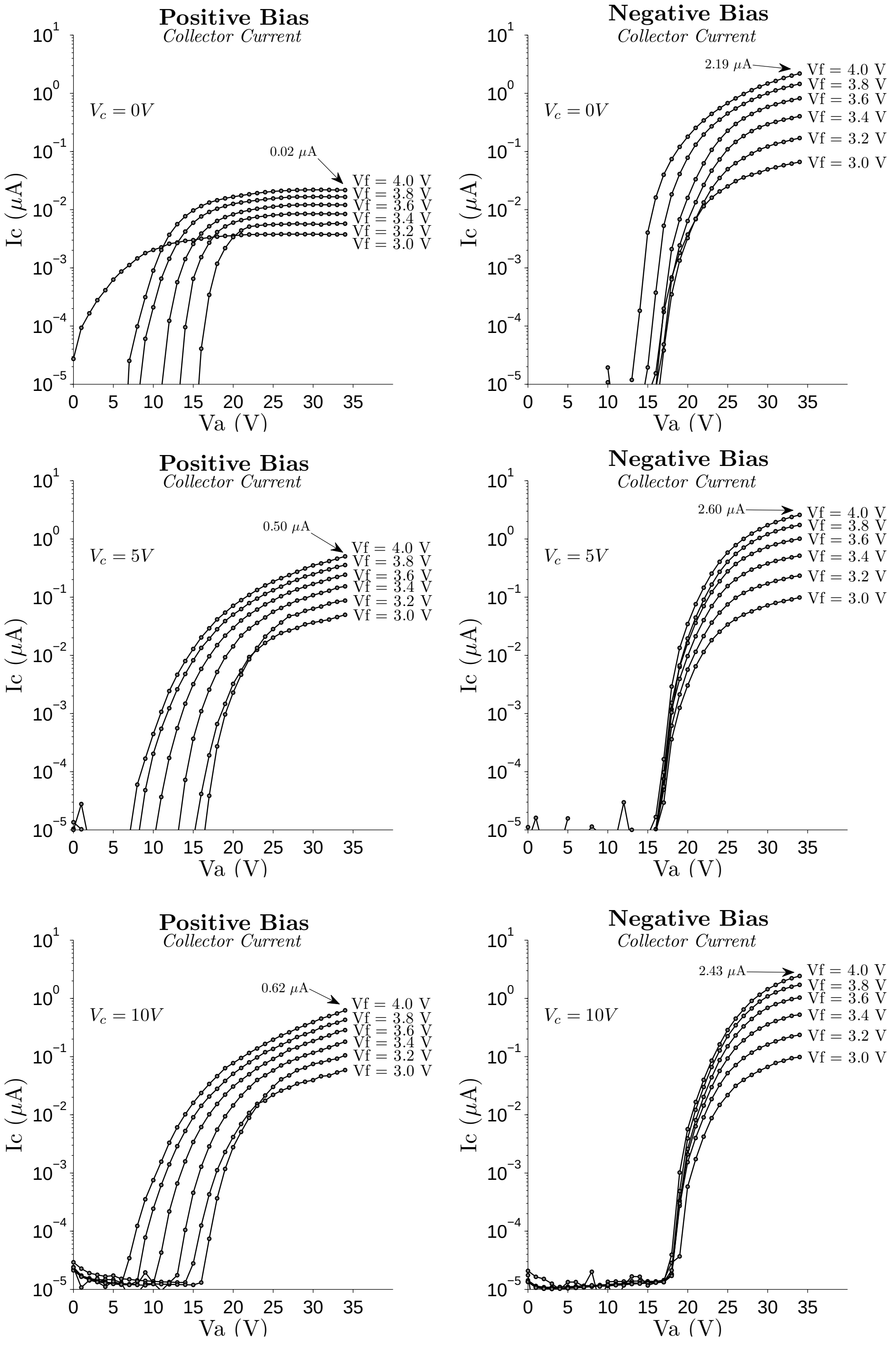

Figure 7.32: Shows the measured current from experiment no. 10. Three measurements were taken and averaged at each anode voltage to obtain the graphs. The emission current for 2b was obtained during the first pump-down, while the beam- and anode current was obtained during the second pump-down. 2a followed the reversed order.

Discussion

It is seen in Figure 7.32 that the beam current is significantly lower for positive bias polarity than for negative. Degeneration of the filament is not to blame, as positive bias polarity was tested prior to negative bias polarity. It is furthermore seen that increasing the Faraday cup voltage leads to higher beam current for the positively biased electron gun. In orbit, the floating potential of CubeSTAR is expected to be a couple of volt negative. Having the Faraday cup biased positive with respect to the top PWB simulates this situation. The Faraday cup sets up an electric field between the top PWB and the cup, thus simulating a coarse approximation to the field which exists between the CubeSTAR top panel and the surrounding plasma. For the Faraday cup voltage of +5 V, which is higher than the expected floating potential of CubeSTAR, the beam current is 0.50 μA for positive bias polarity. For the same Faraday cup voltage with negative bias polarity, the beam current was measured to be 2.60 μA.

It is seen in Figure 7.31 that the anode current for the negatively biased electron gun is increasing monotonically, while for the positively biased electron gun it has a wave-like shape as seen in the last experiment. Clearly, the 0 V on the shield has an influence on the electron gun performance as expected. It is seen in the COMSOL simulations in Figure 7.30 that for the negatively biased electron gun, there is no electric field between the anode and the top PWB. The electrons are unaffected and goes in a straight line towards the Faraday cup. For the positively biased electron gun, on the other hand, there exists a field between the anode and the top PWB. It is seen that the positive potential from the anode bulge outwards from the aperture in the top PWB. The electrons get through the aperture but looses much of their kinetic energy due to the retarding electric field.

A decrease in dynamic range of the electron gun with respect to the previous experiment is also noticed. This is most likely a result of the extensive testing. The characteristics of the electron gun taken during the last part of this experiment, is now similar to the performance of characteristics of the electron gun in Section 7.5.

As the electron gun is of now, it should be biased negatively with respect to the CubeSTAR frame ground to avoid any interference.

7.8 Experiment no. 11 - Supporting Electrode

Introduction

The purpose of this experiment was to investigate whether or not the supporting electrode had an influence on the electron gun performance.

Experimental method

Prototype 2a was configured in the same way as in experiment no. 9, except for that the supporting electrode was placed 0.6 mm closer to the base PWB. The reason for this was to have the filament protruding further up from the supporting electrode, to avoid the filament to sag into the aperture. This configuration left about 2 mm between the electrodes, and 1 mm between the tip of the filament and the anode. Prototype 2b was configured in the same way as prototype 2a, but without the supporting electrode. This left about 1 mm between the tip of the filament and the anode. Both prototypes were tested twice with a two hour time interval in the first pump-down, and once in the second pump-down. The purpose of this was to look for changes between the pump-downs and tests. Both prototypes had fresh filaments.

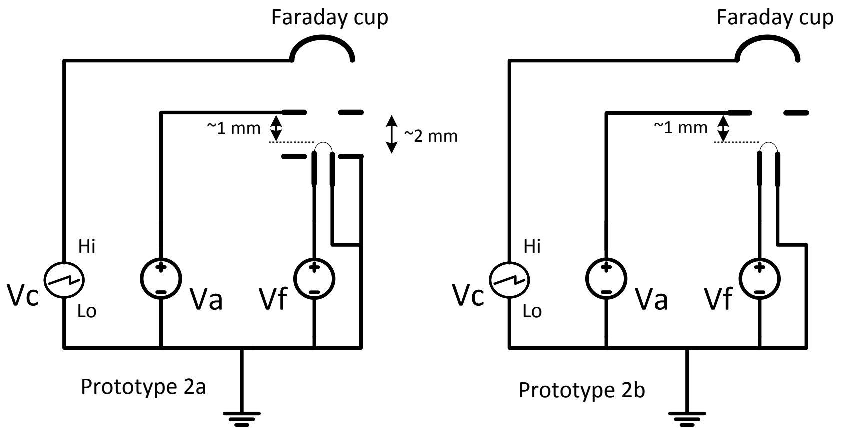

Figure 7.33: Shows the setup of experiment no. 11

Results

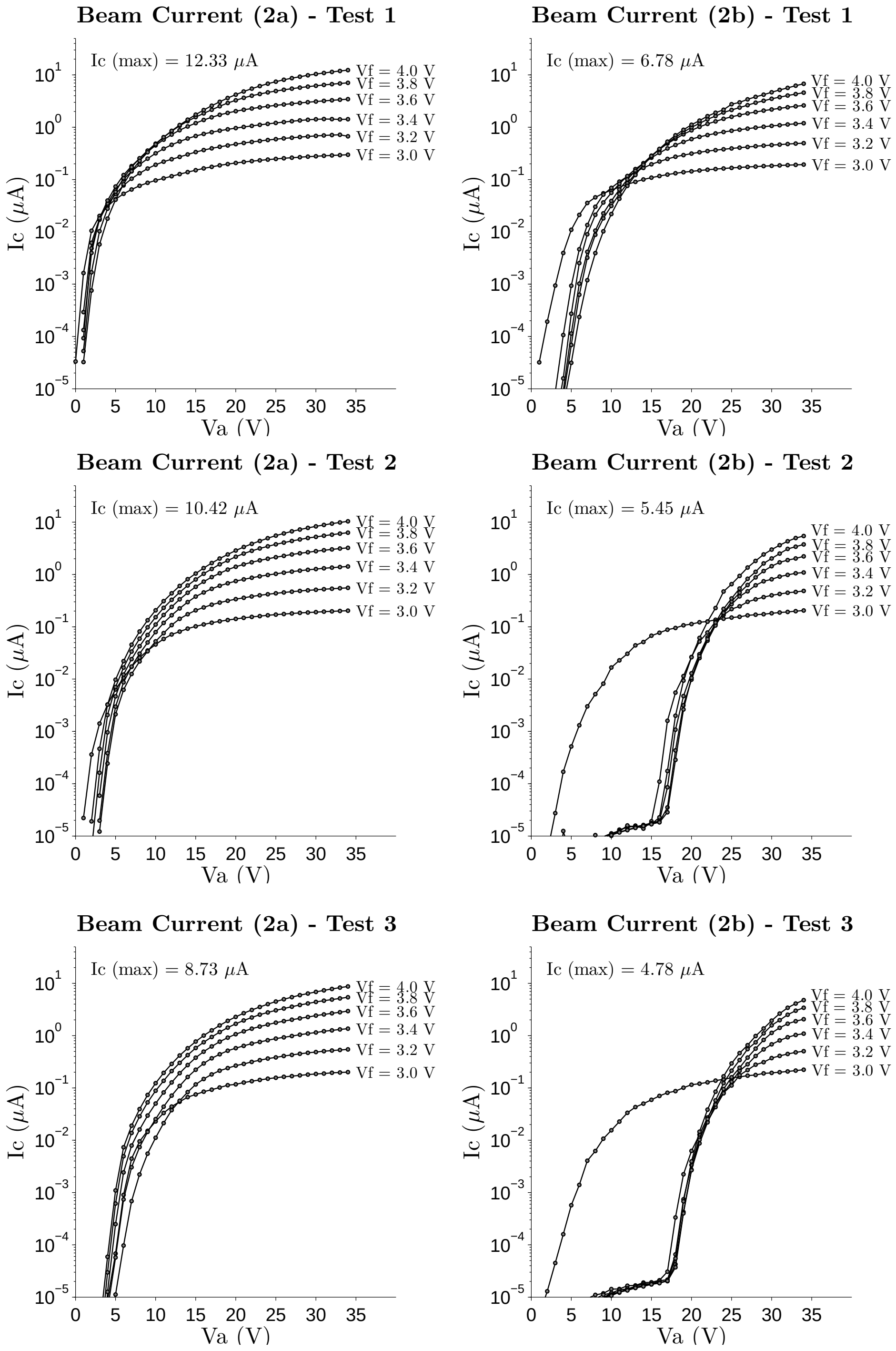

Figure 7.34: Shows measured current from experiment no. 11. Three measurements were taken and averaged at each anode voltage to obtain the graphs. Test 1 and 2 were taken at the same pump-down, while test 3 was taken at the second pump-down.

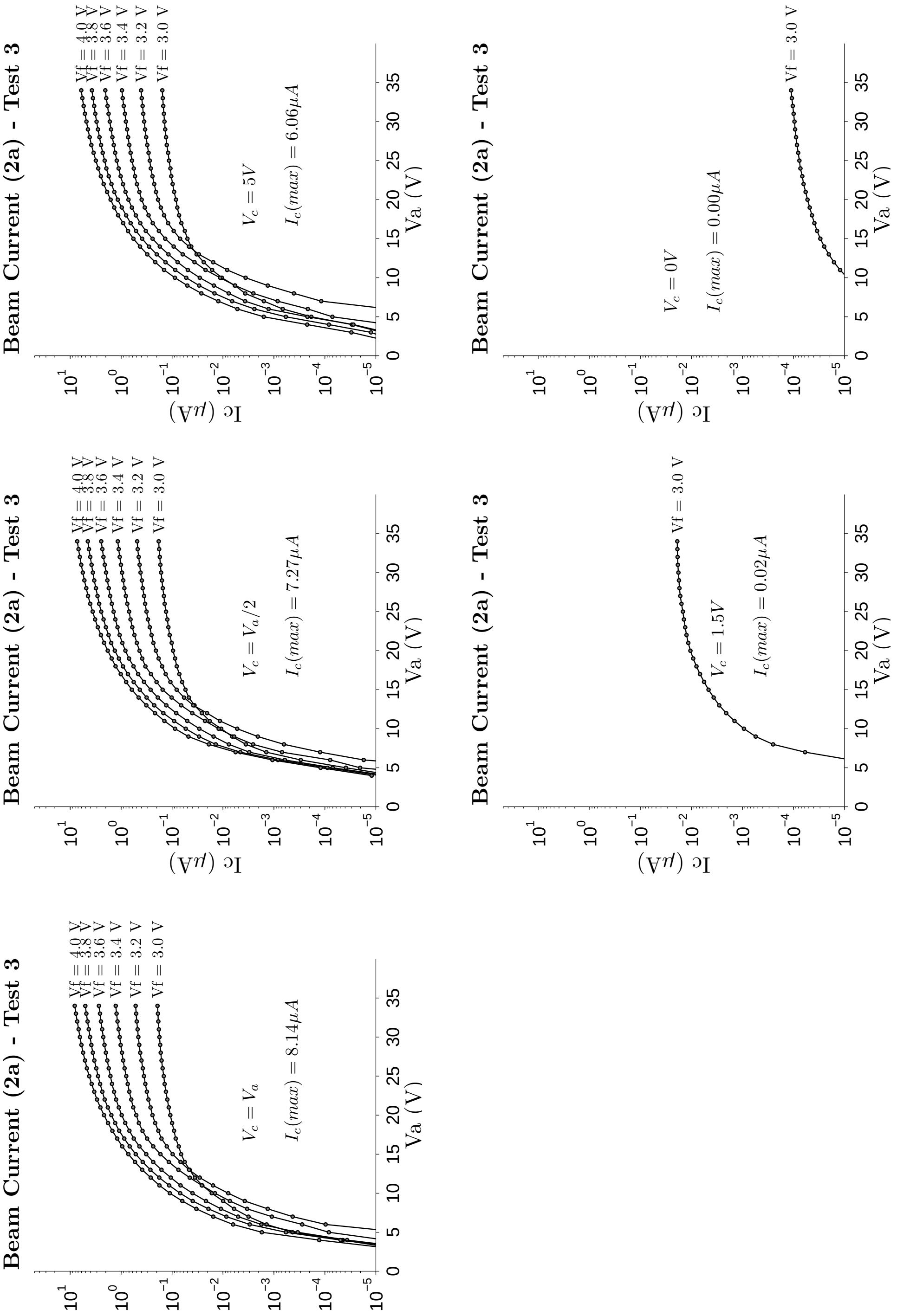

Figure 7.35: Shows the measured current from experiment no. 11 at different Faraday cup voltages during test 3. Three measurements were taken and averaged at each anode voltage to obtain the graphs.

Discussion

A shift in the positive x-direction and a lower dynamic range between the tests is seen in the characteristics of both prototypes in Figure 7.34. However, the shift is more severe for the electron gun configured without the supporting electrode, and it is tempting to believe this is due to the ground potential of the supporting electrode. A lowering in the beam current, that is a shift in the negative y-direction, is also observed between the tests for both prototypes. This is most likely due to degeneration of the filament. Another interesting observation is that the first measurement series for prototype 2b in each anode sweep, that is Vf = 3.0 V, follows a different curve. It is believed that this is because it is the first sweep in the sequence, and not necessarily due to the lower filament voltage.

It is furthermore seen in Figure 7.35, that the voltage on the Faraday cup influences the measured beam current to a very little extent for voltages higher than the filament voltage. The anode sweeps performed to obtain he graphs in figure 7.35 was performed after the ones performed to obtain the graphs in Figure 7.34. It is fair to assume that the lowered beam current is due to degeneration of the filament, and not due to the Faraday cup voltage. For a Faraday cup voltage lower than the filament voltage, the potential between the filament and the cup will be a negative value and hence the electrons do not have enough energy to reach the cup. Initial kinetic energy of the electrons and potential drop over the filament influences the situation and leads to deviations.

7.9 Experiment no. 12 - Limiting the Beam Angle

Introduction

The purpose of this experiment was to introduce a third electrode, whose function is to limit the angle of the beam. A second purpose of this experiment was to test 0.50 mm thick PWB electrodes.

Experimental Method

Prototype 2c was configured with electrodes and a base PWB manufactured from a 0.50 mm thick FR-4 circuit board. The prototype includes a fresh filament, a supporting electrode, an anode and a third electrode whose purpose is to limit the beam angle. This third electrode will be referred to as the 2nd anode, while the first anode is referred to as the 1st anode. The diameters of the apertures in the supporting electrode and in the anodes are 2.5 and 3.0 mm respectively. The prototype is seen from various angles in Figure 7.36, and the experimental setup is shown in Figure 7.37.

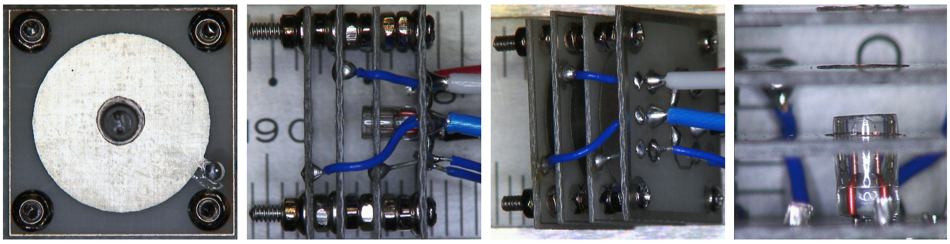

Figure 7.36: Shows prototype 2c from various angles with 0.5 mm thick electrodes and a third electrode to reduce the beam angle. The dimensions on the ruler is in mm. Two hex nuts separates the supporting electrode from the 1st anode, which gives a separation of approximately 2 mm. The 2nd anode is placed approximately 1.6 mm in front of the 1st anode, separated by one hex nut and a metal cup washer. The distance between the tip of the filament and the anode is measured to be approximately 1 mm.

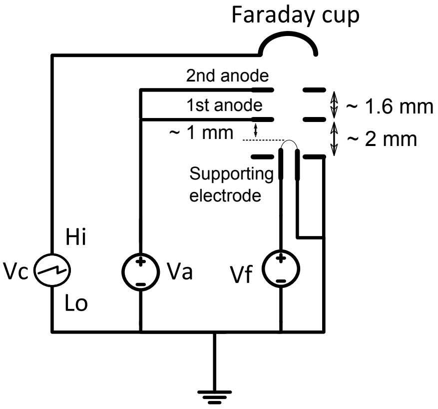

Figure 7.37: Shows the setup of experiment no. 12. The beam current and anode currents had to be obtained in different test-runs as illustrated in Figure 7.9c.

Results

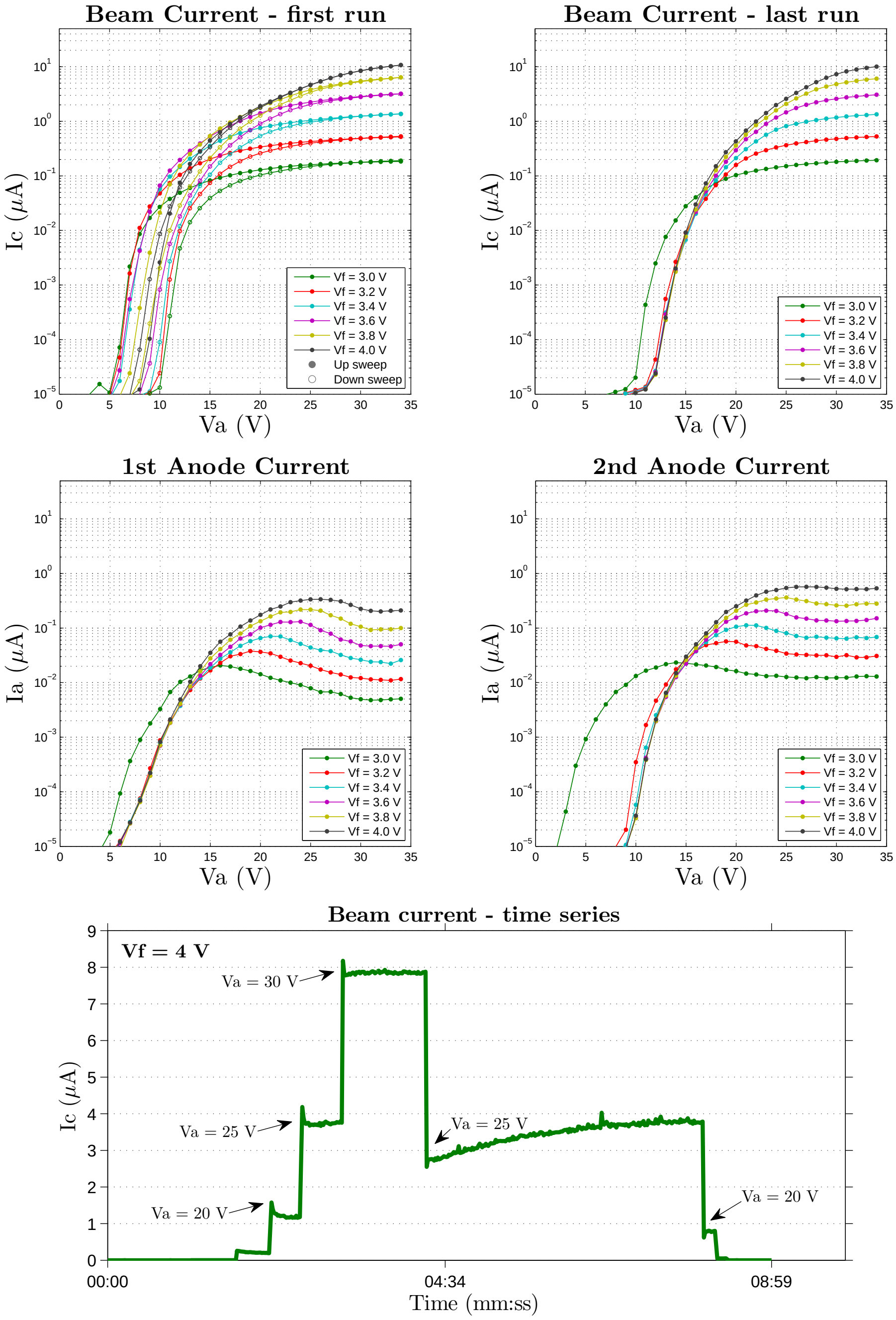

Figure 7.38: Shows the measured beam current in experiment no. 11. The graphs were obtained in the following order: (1) Beam Current - first run, (2) Beam current - time series, (3) 2nd Anode Current, (4) 1st Anode Current and (5) Beam Current - last run. For the anode sweeps, three measurements were taken and averaged, and one measurement were taken every second in the time series.

Discussion

It is seen in Figure 7.38 that the characteristics of prototype 2c is similar to the characteristics of prototype 2b shown in Figure 7.34. Experiment no. 11 indicated that having a supporting electrode would prevent the dynamic range from being deteriorated. However, according to the results shown in Figure 7.38, this is not the case. The reason for this sudden change in the characteristics remains unknown, but it is thought to be due to either deformation or contamination of the filament. It is still recommended to use the supporting electrode for mechanical stability.

The efficiency of the 2nd anode is not known, as the measurement system current does not have the possibility of measuring the beam angle. It is seen, however, that this electrode collects electrons and it assumed that these are the electrons with the largest angle to the symmetry axis. The working principle of this electrode is illustrated in Figure 7.39. The equipotential contour lines bulge through and gives the electrons a diverging effect between the first and second anode. Since the potential on the outside of the second anode is the same as on the inside, there is no electric field here. Hence, the electrons which passes this second anode goes in a straight line and is not diverged.

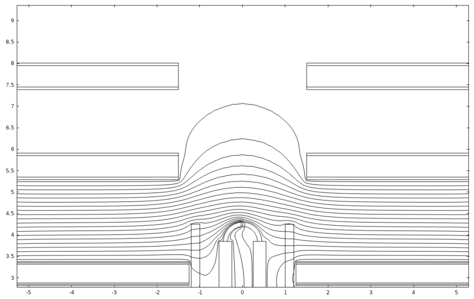

Figure 7.39: Shows a COMSOL simulation of the potential distribution in the electron gun. The copper traces have been exaggerated to ease computation. The filament is at -30 and -26 V, the supporting electrode is at -30 V and the anodes, together with the boundaries in the simulation, are at 0 V.

A significant lower beam current is measured when the anode voltage is changed in discrete step from a higher value. The time it takes for the beam current to go back to the value it had on the up steps is very long, as seen in time series-graph. Changing the filament voltage instead of the anode voltage and the Faraday cup voltage, as seen in experiment no. 7, does not seem to produce this effect. This behaviour can be an artifact of the Faraday cup measurement, and it is not necessarily due to the electron gun. A time series sweep of Prototype 2c was taken in experiment no. 13 as well, with the same experimental setup. The results, not presented in this thesis, showed less settling time for the anode voltage changes, and no settling time for the filament voltage changes.

7.10 Experiment no. 13 - New Filament

Introduction

The purpose of this experiment was to characterise the emission current of a wire-terminal lamp rated for 5V and 105 mW, and perform a stability test of the filament temperature.

Experimental method

The filament[4], with the tip of the glass envelope removed, was soldered to a base PWB with an apertureless PWB electrode placed approximately 1.5 mm in front of the tip of the filament. The experimental setup is similar to the one shown in Figure 7.3, and thus omitted here. To extract the emission current, both filament and anode sweeps were performed. The pressure in the vacuum chamber was not known, as the pressure gauge was still gone, but it should be similar to the ones obtained earlier.

To test the stability of the filament temperature, four filaments were mounted directly with the wire terminals to a breadboard. The light bulb, in which the filaments were situated, were still intact and the test was therefore performed in a more protected environment. Two and two filaments were connected in parallel and powered by a +5 V and a +6 V power supply. The current was measured by connecting a Fluke 75 multimeter in series with each filament, and the resistance was calculated using Ohms law. This is the resistance of the filament at operating temperature. The room temperature resistance was measured by disconnecting the filament from the breadboard and measured with the Fluke 75 multimeter. The wire resistance of the test leads were not corrected for, but this is not important as it will be a systematic error. The temperature of the filaments were then estimated as described in Section 7.1.

---

[4] 105 mW wire terminal lamp with a T 3/4 bulb size purchased at www.farnell.com with order code 2078333.

Results

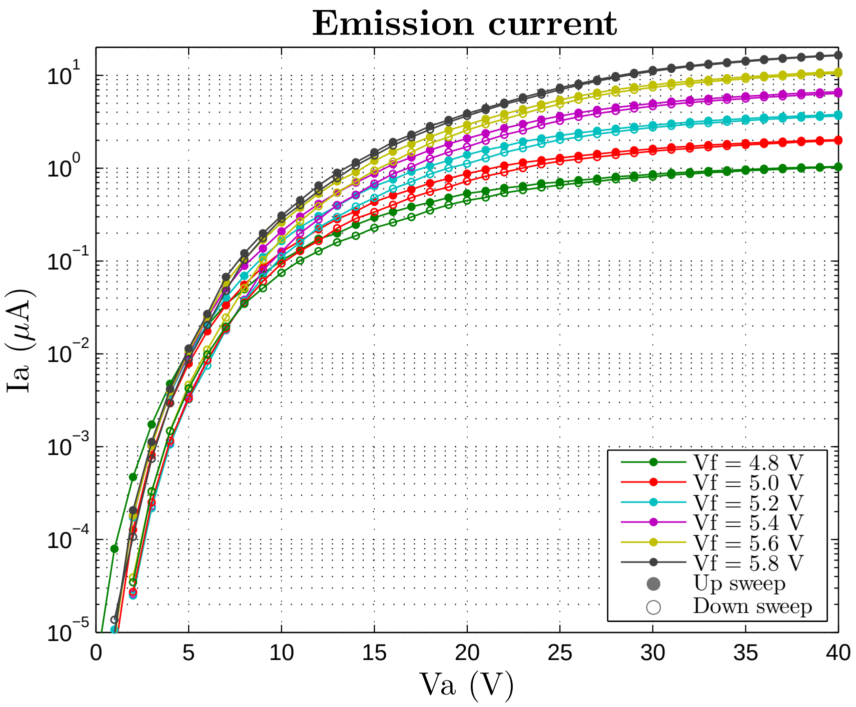

Figure 7.40: Shows the emission current of the 105 mW filament.

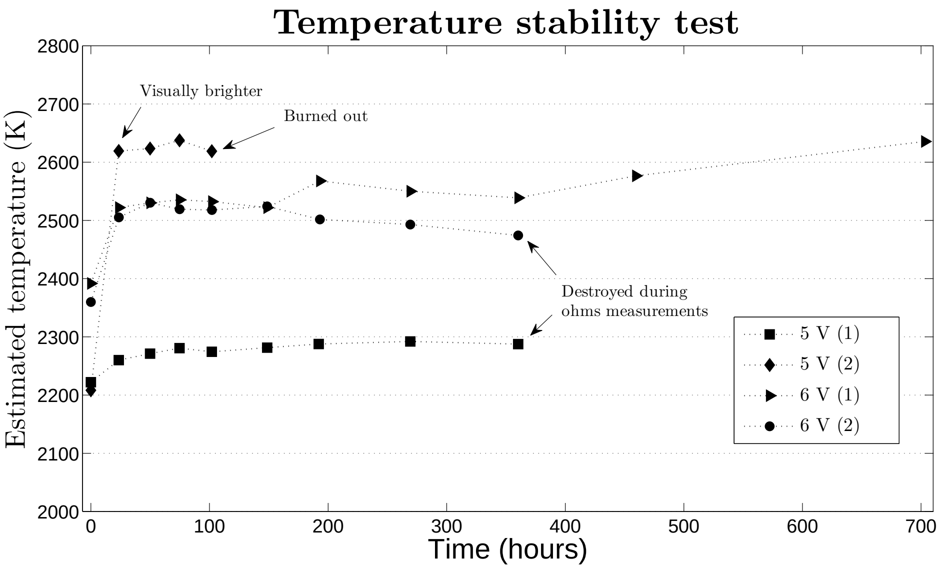

Figure 7.41: Shows an estimate of the temperature stability.

Discussion

It is seen in Figure 7.40 that this new filament rated for 105 mW gives an emission current, at its normal ratings, of approximately 2 μA with an anode voltage of 40 V. This is in the middle of the desired interval for the beam current of 0.5 - 5 μA, as stated in Chapter 2. The tests which will be presented in Chapter 8 showed, however, that a slightly higher beam current is necessary to control the floating potential of CubeSTAR. If this filament shall be used in the electron gun on the flight model of CubeSTAR, the voltage on the filament should have capabilities of being overrun to increase the beam current. Increasing the filament voltage has severe impact on the filament's lifetime and there will be a trade-off between longevity and beam current.

The temperature stability test was performed to get an initial understanding of the stability of the filament. More in-depth lifetime tests of the filaments should be performed in vacuum connected in a diode or electron gun configuration, as the filaments are in a very protected atmosphere inside the glass envelope. Contamination or poisoning from other materials present in the proximity of the electron will influence the lifetime of the filament, and needs to be taken in account. As one can see from the graph in Figure 7.41 the estimated filament temperature varies. An interesting observation is that the temperature gets higher during the first hours. One of the filaments got visibly brighter between two measurements, and the estimated temperature increase was 400 K. This filament, with a expected lifetime of 10 000 hours, burned out after just 100 hours. One must expect production flaws in these low cost light bulbs which emphasizes the importance of having redundancy on CubeSTAR. Two other filaments got destroyed during mechanical handling of the ohms measurements. It is recommended to make a more automated measurement setup if these tests are to be repeated. The light bulb who survived this test the characteristic bulb blackening was observed. This is due to evaporation of the filament material.

Chapter 8

Active Spacecraft Potential Control: Proof of Concept

Active spacecraft potential control of a preliminary CubeSTAR model was to be demonstrated at the European Space Research and Technology Centre (ESTEC). The demonstration, which is presented in this chapter, combines all the work conducted in this thesis into a system test.

8.1 Experimental Method

A full scale model of CubeSTAR was mounted on a rod in the centre of the plasma chamber at ESTEC, with an electron density typical for LEO. The CubeSTAR model, which was modified in accordance to the proposed method in Section 2.4, included side panels without solar cells mounted, and a top panel coated with graphite. The solder lands for the solar cells were left uncovered and grounded to the frame together with the top panel. This configuration gives approximately the same area of conductive surfaces as expected on the flight model of CubeSTAR. The resistance between any two points connected to the frame was measured to be less than 6 kΩ. The CubeSTAR model with the electron gun mounted is shown in Figure 8.1.

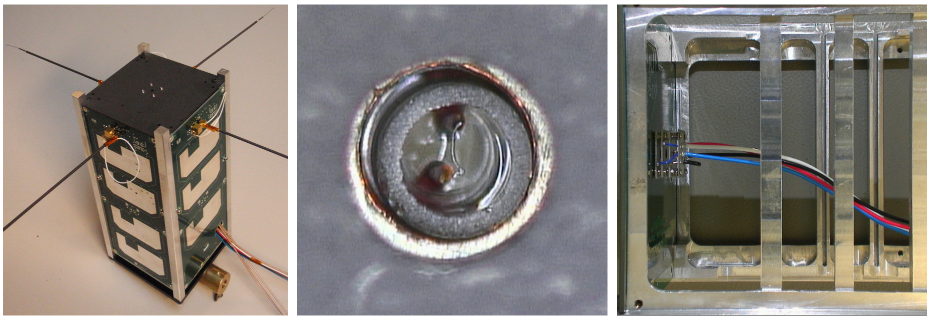

Figure 8.1: Shows the CubeSTAR model used in the experiment at ESTEC.

The prototype 2c electron gun, with a fresh filament of the type described in Section 5.4.1, was mounted in the centre of the graphite coated top panel as seen in Figure 8.1. The emitted current during the tests should therefore be somewhat similar to the graphs presented in Section 7.9. The CubeSTAR top panel, which will be the ram-facing side in orbit, was oriented towards the plasma source in the chamber, and the m-NLP probes mounted to the side panels were used to perform IV-sweeps. During most of the tests the filament and the supporting electrode were biased negatively with respect to CubeSTAR ground, in which the anodes were connected. This is the configuration shown to the right in Figure 8.2. In one of the tests, the filament was at the frame potential while the anodes were biased to a positive potential. The experimental setup of the test is shown in Figure 8.2.

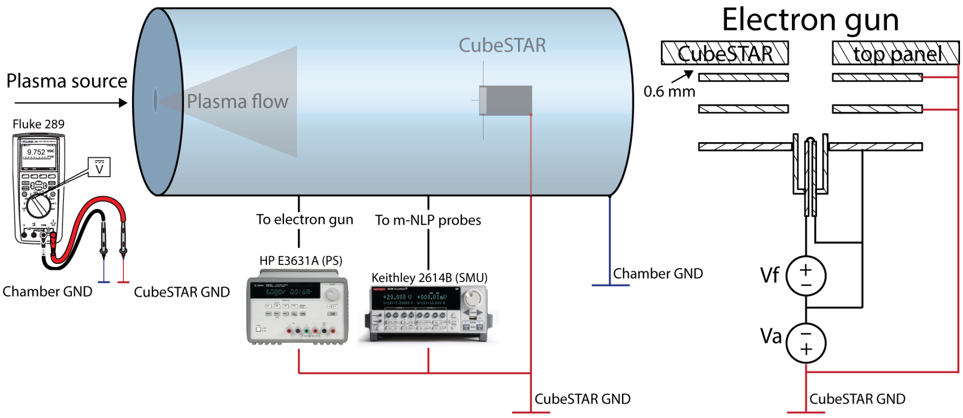

Figure 8.2: Shows an overview of the experimental setup. A power supply was used to control the electron gun while a source measurement unit performed measurements with the m-NLP probes. Both instruments were left floating and connected to the CubeSTAR ground potential. A multimeter was used to measure the potential difference between the CubeSTAR frame and the chamber wall.

In the graphs presented in Figure 8.3 one m-NLP probe was oriented towards the plasma source and swept from -5 V to +8 V and back to -5 V. A Keithley 2614B SMU was left floated and connected to the CubeSTAR frame while performing the sweeps on the probe. A HP E3631A PS, which too was left floated and connected to the CubeSTAR frame, powered the electron gun with different settings during the IV-sweeps on the m-NLP probe. The potential difference between the CubeSTAR frame and the plasma chamber wall was measured with a Fluke 289 multimeter[1].

In the graphs presented in Figure 8.4, two probes were oriented 45° to the plasma source and biased to +7 V and +5 V while the settings on the electron gun were changed in discrete steps. The potential difference between the tank and CubeSTAR frame was measured continuously.

---

[1] The potential difference between the chamber and the plasma is assumed to be zero.

8.2 Results

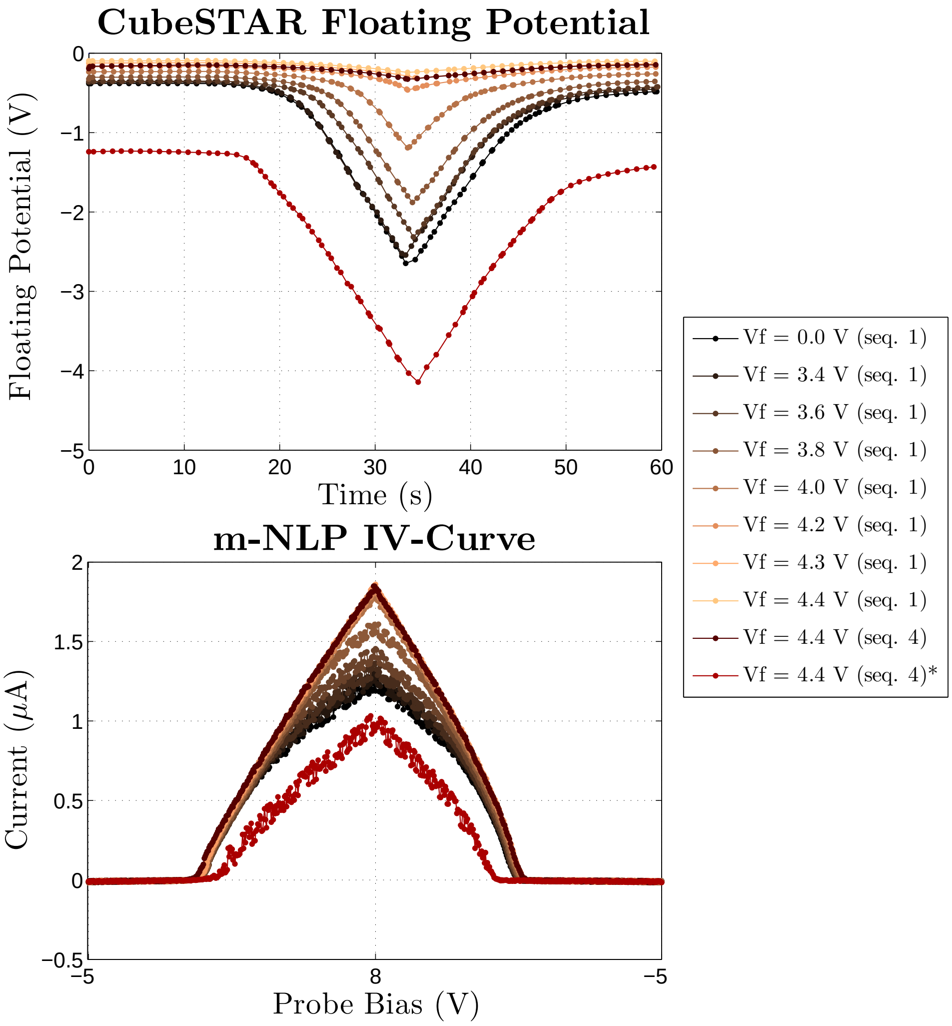

Figure 8.3: Shows the floating potential of CubeSTAR and the current to the m-NLP probe during the plasma chamber test at ESTEC. The top figure shows the measured potential difference between the chamber wall and the CubeSTAR frame during the m-NLP sweeps presented in the bottom figure. The sweeps were performed with the electron gun operating on a fixed anode voltage of 35 V with different filament voltages. The results from sequence 1 and 4 should be similar, but the graph marked with an asterisk was performed with positive bias on the anodes, and the filament at frame potential. The reason for the misalignment between the two graphs is because the recordings of the floating potential and the m-NLP probes are not identical in duration.

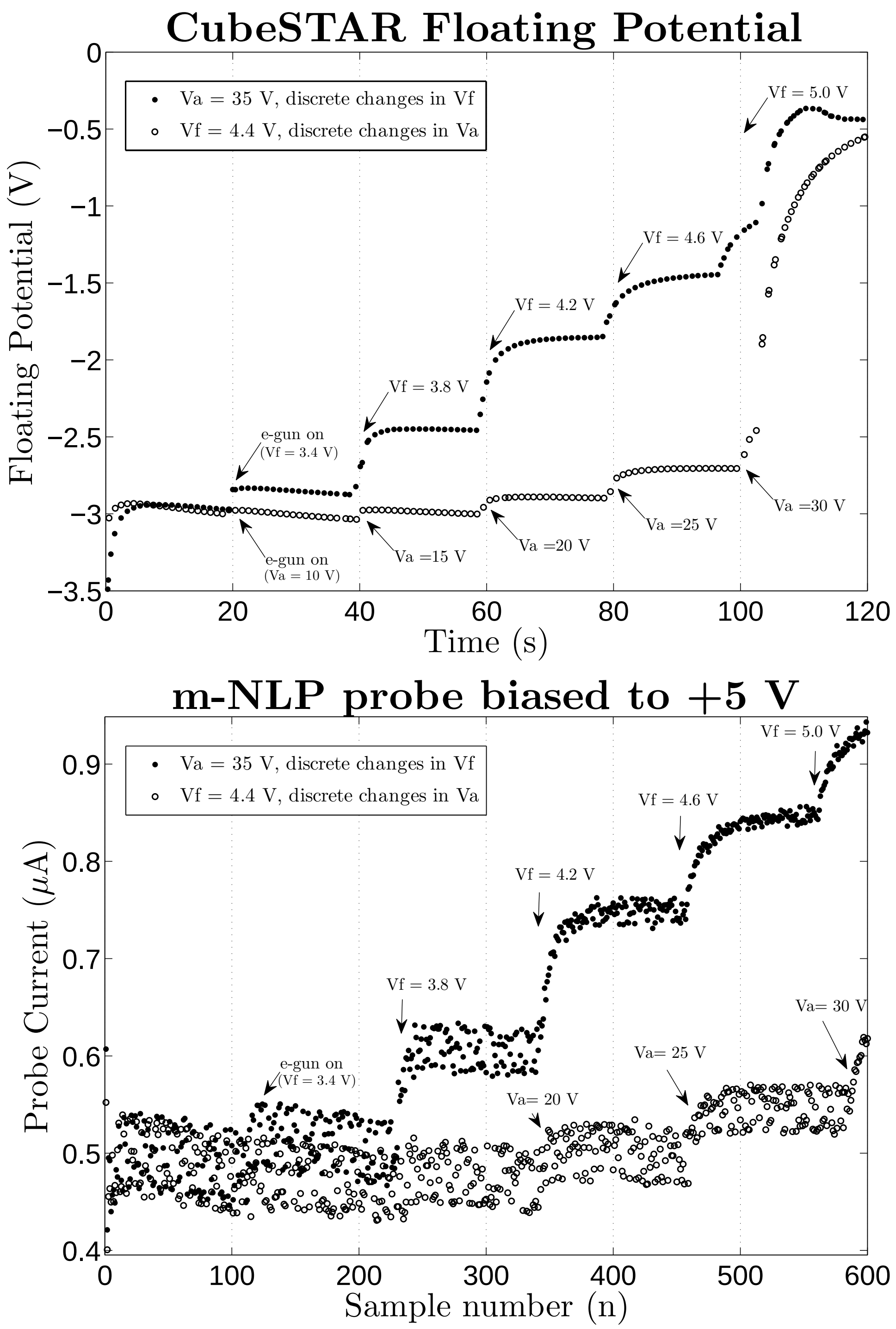

Figure 8.4: Shows the floating potential of CubeSTAR and the current to one m-NLP probe during the plasma chamber test at ESTEC. Two m-NLP probes were biased to +7 V and +5 V while the settings on the electron gun were changed in discrete steps. The reason for the increase in the floating potential at start-up is due to change in the probe bias. The reason for the misalignment between the two graphs is because the recordings of the floating potential and the m-NLP sweeps are not identical in duration.

8.3 Discussion

The tests performed in the plasma chamber at ESTEC have shown that the developed electron gun can control the floating potential of CubeSTAR. The electron gun is however, as expected, not capable of emitting enough electrons at its normal ratings. A filament with higher emission current is necessary.

It is seen in Figure 8.3 that the effect of turning the electron gun on, with the filament voltage being 3.4 V and the anode biased to 35 V, yields just a minimal effect on the floating potential. According to Figure 7.38 in Section 7.9 the electron gun should emit a current between 1-2 μA at this setting. A minor decrease in emitted current is, however, expected due to loss in the CubeSTAR top panel. Having the filament in the electron gun at 4.2 V, with an estimated current[2] of 20 μA, gives on the other hand a very good suppression of the descending floating potential of CubeSTAR during the IV-sweeps.

During the tests, CubeSTAR obtained a negative floating potential with respect to the plasma as can be seen in the figures. This is in compliance with the theory discussed in Chapter 2. In the test, the floating potential of CubeSTAR was approximately -0.4 V without the probes biased, which is roughly the estimated values of CubeSTAR for the conditions expected in LEO. It should be possible to calculate the electron density in the plasma chamber with the aid of the m-NLP measurements, but this has not yet been done. It is further seen in Figure 8.3 that turning the electron gun on, with the maximum settings used in the test, raised the floating potential from -0.38 to -0.10 V withouth the probe biased. The effect of the electron gun is even better at more negative voltages as seen in the region of the figure where the probes starts to collect electrons. At a probe bias of +8 V, the electron gun raised the potential of CubeSTAR from -2.65 to -0.24 V. On CubeSTAR the m-NLP system will be consisting of four probes with fixed bias between +2.5 to +8 V.

It is furthermore seen in Figure 8.3 that the positively biased electron gun fails to suppress the descending potential of CubeSTAR during the IV-sweeps. This is, as discussed in Section 7.7, due to the influence the ground potential on CubeSTAR has on the emitted beam. An interesting observation is that the positively biased electron gun does not only fail to suppress the descending potential of CubeSTAR, but it also lowers the potential even further with a significant amount. In the tests, the potential of CubeSTAR was lowered from -0.38 to -1.24 V with the probes unbiased, and from -2.65 to -4.14 V with the probes biased to +8 V. A conclusion that

---

[2] Estimate based on the results with prototype 1 given in Figure 7.21 and interpolation of the results in Figure 7.38.

can be drawn is that the CubeSTAR top panel does not completely shield out the potential of the positively biased anodes. The anodes then acts as Langmuir probes starting to collect electrons to the CubeSTAR frame. As the top panel suppressed the beam current of the electron gun in addition to driving the floating potential of CubeSTAR to more negative values, it is recommended to use negative bias on the electron in the flight model of CubeSTAR.

It is seen in Figure 8.4 that the floating potential of CubeSTAR can be changed in discrete steps by adjusting the filament and anode voltage. The reason for the insignificant influence of the changes in small anode voltage is most likely due to the degeneration of the filament and subsequently lower dynamic range as explained in Chapter 7. As seen in the graph *CubeSTAR Floating Potential* there is a leap in potential when the anode is increased to 30 V. Due to synchronization issues between the recordings of the potential and the probes, the current to the m-NLP probes during this leap is barely seen at the end of the graph *m-NLP probe biased to +5 V*. If the issues with the lowering of the dynamic range of the electron gun is not fixed, it is recommended to adjust the beam current with the filament voltage.

A settling time is observed for the floating potential of CubeSTAR. In the first part of the graph *CubeSTAR Floating Potential* it is seen that the potential of CubeSTAR is decreasing with time when the electron gun is on. This could be due to the settling time of the change in probe bias at the very start of the measurements. In the middle part it is seen that the potential settles to a stable value. The graph *m-NLP probe biased to +5 V* illustrates the effect a higher floating potential has on the fixed biased m-NLP probes. When the electron gun adjusts the frame potential to a higher value, the bias of the probe with respect to the plasma increases, and more current is collected by the probes.

Chapter 9

Summary and Conclusion

The work conducted in this thesis has involved several disciplines, from theoretical and experimental physics to mechanical designs and instrumentation. The following goals have been achieved:

- A miniaturized thermionic electron gun specifically designed for mitigating spacecraft charging of CubeSats has been developed. The electron gun consists of a filament harvested from a commercially available light bulb rated for 3 V at 17 mA, and a mechanical design of the electrodes not found in the literature. This novel design uses plated through-holes on printed wiring boards as the apertured electrodes, yielding a physical dimension of the electron gun of only 15 $\times$ 15 $\times$ 10 mm. The achievable beam current of the electron gun is in the high nA-range with the filament operating at its normal ratings, and with a bias voltage of up to 40 V. A substitute filament rated for 105 mW has been found with an emission current in the desirable low μA-range.
- A low-current measurement system for running the characterization procedures on the electron gun has been developed.
- A method for rendering the surface of CubeSTAR electrically conductive has been proposed. Having an electrostatic clean surface is a necessity when using electron guns for active spacecraft potential control. Included is recommendations and a literature study on transparent conductive coatings for covering the surfaces of the solar cells.
- Active spacecraft potential control of a preliminary model of CubeSTAR has successfully been proven during testing in the plasma chamber at the ESA space centre ESTEC. The tests showed that the floating potential of CubeSTAR can be locked to a comfortable level close to the plasma potential by using the developed electron gun. By overrunning the filament voltage on the electron gun to 4.4 V, the potential on CubeSTAR was raised from -2.65 to -0.24 V.

Despite that a lot of the goals were achieved, there are still work remaining. The following needs to be performed prior to launch in order to have a satisfying active spacecraft potential control of the CubeSTAR nanosatellite:

- The driver circuit for the electron gun must be developed for successful integration into CubeSTAR. This goal has not been met as the electron gun development process was more time consuming than foreseen. There was also an uncertainty in whether or not the electron gun could operate on positive bias voltages until it was disproved during the testing at ESTEC. Some thoughts on the driver circuit are presented in Appendix C.
- Solar cells with conductive coatings must either be purchased, or the existing solar cells must be covered with one of the recommended coatings. If the latter is chosen, the characterization of the coated solar cells should be resumed to ensure sufficient power efficiency. Unused areas on the top electric of the PCBs covering the surface of CubeSTAR should be filled with a ground layer.
- Characterization should be performed on the electron gun with the filament rated for 105 mW mounted. This filament gives an emission current of approximately 2 μA at its normal rating, and a beam current in the desirable range of 0.5 to 5 μA can be expected. Testing performed at ESTEC indicated, however, that a slightly higher beam current is necessary to control the floating potential of CubeSTAR. It is estimated that overrunning the filament voltage with 16 % to 5.8 V will give a sufficient current of approximately 20 μA.
- Lifetime tests should be performed on the electron gun with the 105 mW filament, as the tests performed with the filament rated for 3 V at 17 mA showed significant degeneration of the performance with respect to lower beam current and dynamic range. This test should be performed in an environment close to the low earth orbit which includes a plasma where the dominant ion being the reactive O^+. If the lifetime tests of the filament from the 105 mW light bulb fails, the following actions are recommended:
    - Obtain a filament from a commercially available light bulb with higher power consumption and/or lower work function, which then can be operated at its normal rating or lower.
    - Perform a follow-up on the progress of the development of a low power cathode at Kimball Physics.
    - Investigate the possibilities of obtaining filaments made of Rhenium as these will, according to Erdman and Zipf (1982), survive longer in oxygen environments than filaments made of Tungsten.

- The measurement system should be improved by incorporating the possibility of measuring the beam angle. Plans were in place to implement such as system which is presented in Appendix C.

9.1 Flight Model of the Electron Gun

Figure 9.1 shows a concept drawing of the proposed flight model of the electron gun. The configuration and dimensions are the same as in prototype 2c presented in Section 7.9, except for a larger base PWB to incorporate the driver electronics, and a conductive outer housing as spacer.

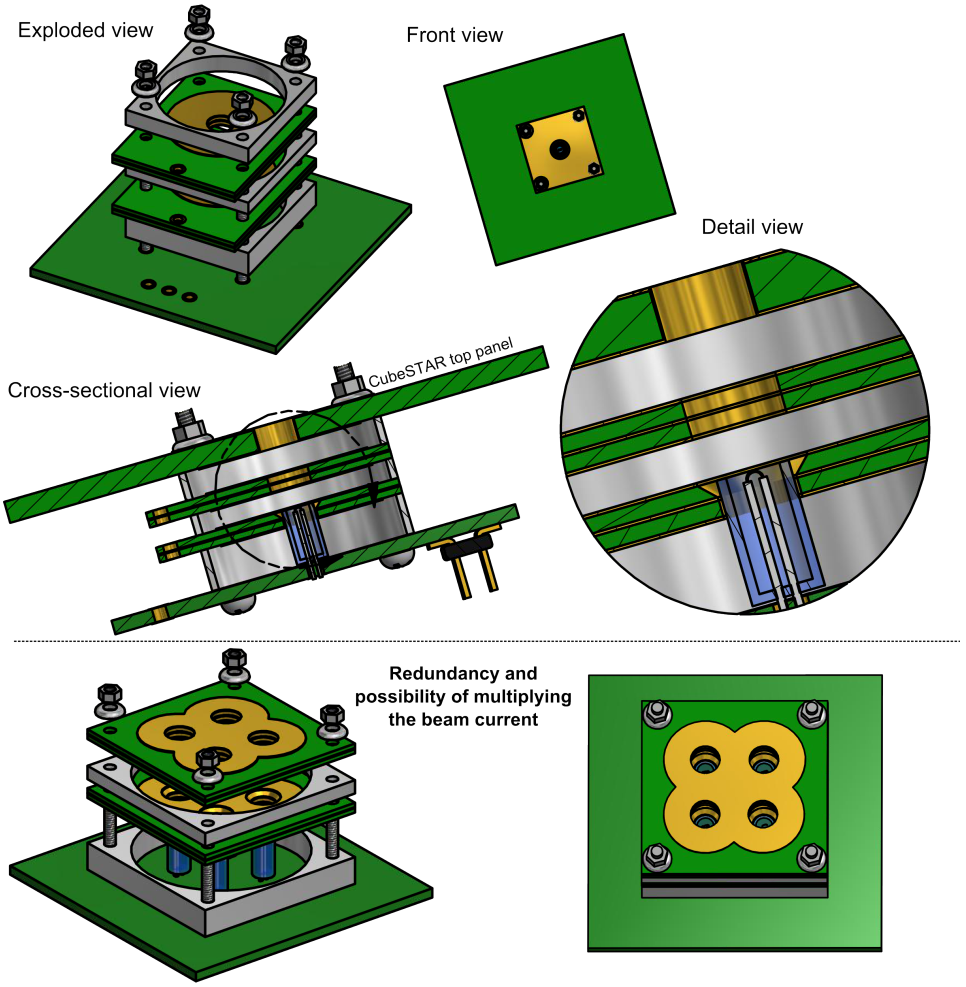

Figure 9.1: Shows a concept drawing of the proposed flight model of the electron gun. Among the differences between prototype 2c can a larger PWB to incorporate the driver electronics, a conductive outer housing and a countersink hole in the supporting electrode to resemble the Pierce-type electron gun be mentioned. Adding redundancy to the design requires a minimum amount of extra space.

The electron gun is directly mounted to the top panel on CubeSTAR with the fours screws, in which the beam angle-limiting electrode is embedded. This will ensure that there is no other copper tracks in the proximity of the top panel possibly disturbing the electric field. The distance and size of the aperture of this electrode should be derived once the measurement system has the capabilities of measuring the beam angle. The plated through-hole electrodes can be panelized and ordered in a large quantity with different shapes and sizes for further experimentation with minimum additional costs. It is proposed to replace the aperture in the supporting electrode with a countersunk hole to make a Pierce-type electron gun as seen in the detail view, but the effect of this should be investigated. As the electrical field inside a cylinder is zero, the necessity of ordering the electrodes in 0.5 mm or 1.0 mm thickness should be reviewed. The electrical connections between the base PCB and the PWB electrodes are made with external wires using through-hole soldering which is seen to the left in the cross-sectional view. An inner copper layer in the PWB electrode makes electrical contact with the plated through-hole and its annular ring. This is illustrated in the detail view. By doing so the inside of the electron gun can be completely isolated from the outside by the metal rings machined out in the space approved material 7075 aluminium. For redundancy and possibility of multiplying the beam current, it is recommended to incorporate several separate electron guns into one single physical unit as seen in the bottom of Figure 9.1.

References

Robert Bakish. *Introduction to Electron Beam Technology.* John Wiley & Sons, Inc., New York, 1962.

Aroh Barjatya. *Langmuir Probe Measurements In The Ionosphere.* PhD thesis, Utah State University, 2007.

T. A. Bekkeng, A. Barjatya, U.-P. Hoppe, A. Pedersen, J. I. Moen, M. Friedrich, and M. Rapp. Payload charging events in the mesosphere and their impact on langmuir type electric probes. *Annales Geophysicae*, 31(2):187–196, 2013. doi: 10.5194/angeo-31-187-2013. URL `http://www.ann-geophys.net/31/187/2013/`.

Tore André Bekkeng. Prototype development of a multi-needle langmuir probe system. Master's thesis, University of Oslo, 2009.

H. J. Van Der Bijl. *The Thermionic Vacuum Tube - Physics and Electronics*, pages 50–84. McGraw-Hill Book Company, Inc., New York, 1920.

Theodore Jr. F. Bogart, Jeffrey S. Beasley, and Guillermo Rico. *Electronic Devices and Circuits 6th ed.* Pearson Prentice Hall, New Jersey, 2004. ISBN 0-13-111142-6.

D. Chattopadhyay and P.C. Rakshit. *Electronics - Fundamentals and Applications (7th Edition)*, pages 10–26. New Age International (P) Ltd., Publishers, New Delhi, 2006. ISBN 81-224-1780-9.

C. D. Child. Discharge from hot cao. *Phys. Rev. (Series I)*, 32:492–511, May 1911. doi: 10.1103/PhysRevSeriesI.32.492. URL `http://link.aps.org/doi/10.1103/PhysRevSeriesI.32.492`.

F. Ciccacci, E. Vescovo, S. De Rossi, and M. Tosca. Low energy electron gun for isochromat inverse photoemission. *Nuclear Instruments and Methods in Physics Research Section B: Beam Interactions with Materials and Atoms*, 53(2):218 – 222, 1991. ISSN 0168-583X. doi: http://dx.doi.org/10.1016/0168-583X(91)95662-W. URL `http://www.sciencedirect.com/science/article/pii/0168583X9195662W`.

J. Credland, G. Mecke, and J. Ellwood. The cluster mission: Esa's spacefleet to the magnetosphere. *Space Science Reviews*, 1997.

J.L. Cronin. Modern dispenser cathodes. *Solid-State and Electron Devices, IEE Proceedings I*, 128(1):19–32, 1981. ISSN 0143-7100. doi: 10.1049/ip-i-1.1981.0012.

Aldo Vieira da Rosa. *Fundamentals of Renewable Energy Processes 2nd ed.* Elsevier Inc., London, 2009. ISBN 978-0-12-374639-9.

Kim K. de Groh, Bruce A. Banks, Joyce A. Dever, Donald A. Jaworske, Sharon K. Miller, Edward A. Sechkar, and Scott R. Panko. *NASA Glenn Research Centers Materials International Space Station Experiments (MISSE 17).* NASA, Cleveland, Ohio 44135, 2008.

Peter W. Erdman and Edward C. Zipf. Low-voltage, high-current electron gun. *Review of Scientific Instruments*, 53(2):225–227, 1982. ISSN 0034-6748. doi: 10.1063/1.1136932.

Henry B. Garrett and Albert C. Whittlesey. *Appendix G: Simple Approximations: Spacecraft Surface Charging Equations*, pages 152–155. John Wiley & Sons, Inc., 2012. ISBN 9781118241400. doi: 10.1002/9781118241400.app7. URL `http://dx.doi.org/10.1002/9781118241400.app7`.

Roy G. Gordon. Criteria for choosing transparent conductors. *MRS Bulletin*, 25:52–57, 8 2000. ISSN 1938-1425. doi: 10.1557/mrs2000.151. URL `http://journals.cambridge.org/article_S0883769400027172`.

G. Herrmann and Phil. S. Wagener. *The Oxide-coated Cathode*, pages 1–7. Chapman & Hall ltd., London, 1951.

David C. Hill and M. Frank Rose. *Summary of solar cell data from the Long Duration Exposure Facility (LDEF).* Space Power Institute, Auburn University, 1994.

Lonny Kauder. *Spacecraft Thermal Control Coatings References.* NASA/-Goddard Space Flight Center, Greenbelt, Maryland, 2005.

Charles Kittel. *Introduction to Solid State Physics (8th edition)*, page 136. John Wiley & Sons, Inc., Hoboken, 2005. ISBN 0-471-415626-X.

Javad Koohsorkhi and Shamsoddin Mohajerzadeh. Carbon nanotube based miniaturized electron gun and column assembly. *Microsystem Technologies*, pages 1–12, 2013. ISSN 0946-7076. doi: 10.1007/s00542-013-1892-y. URL `http://dx.doi.org/10.1007/s00542-013-1892-y`.

Shu T. Lai. *Fundamentals of spacecraft charging - Spacecraft Interactions with Space Plasmas*, page 8. Princeton University Press, New Jersey, 2012. ISBN 978-0-691-12947-1.

S.T. Lai. A critical overview on spacecraft charging mitigation methods. *Plasma Science, IEEE Transactions on*, 31(6):1118–1124, 2003. ISSN 0093-3813. doi: 10.1109/TPS.2003.820969.

Irving Langmuir. The effect of space charge and residual gases on thermionic currents in high vacuum. *Phys. Rev.*, 2:450–486, Dec 1913. doi: 10.1103/PhysRev.2.450. URL `http://link.aps.org/doi/10.1103/PhysRev.2.450`.

P.C. Lansåker, K. Gunnarsson, A. Roos, G.A. Niklasson, and C.G. Granqvist. Au thin films deposited on sno2:in and glass: Substrate effects on the optical and electrical properties. *Thin Solid Films*, 519(6):1930 – 1933, 2011. ISSN 0040-6090. doi: 10.1016/j.tsf.2010.09.048. URL `http://www.sciencedirect.com/science/article/pii/S0040609010013829`.

C. Lennon, R. Kodama, Y. Chang, S. Sivananthan, and M. Deshpande. Al- and al:in-doped zno thin films deposited by rf magnetron sputtering for spacecraft charge mitigation. *Journal of Electronic Materials*, 37: 1324–1328, 2008. ISSN 0361-5235. URL `http://dx.doi.org/10.1007/s11664-008-0436-1`. 10.1007/s11664-008-0436-1.

Li-jian Meng and M.P dos Santos. Properties of indium tin oxide films prepared by rf reactive magnetron sputtering at different substrate temperature. *Thin Solid Films*, 322(12):56 – 62, 1998. ISSN 0040-6090. doi: 10.1016/S0040-6090(97)00939-5. URL `http://www.sciencedirect.com/science/article/pii/S0040609097009395`.

Chang Liu. *Foundations of MEMS*, pages 173–175. Pearson Education, Inc., New Jersey, 2006.

V. Milanovic, L. Doherty, D.A. Teasdale, Siavash Parsa, and K.S.J. Pister. Micromachining technology for lateral field emission devices. *Electron Devices, IEEE Transactions on*, 48(1):166–173, 2001. ISSN 0018-9383. doi: 10.1109/16.892185.

NASA 2011. *Mitigating in-space charging effects-a guideline*. Nasa, Washington, DC 20546-0001, 2011. NASA-HDBK-4002A, Revision A.

Marla E. Perez-Davis, Tania Malave-Sanabria, Paul Hambourger, Sharon K. Rutledge, David Roig, Kim K. Degroh, and Ching-Che Hung. *Transparent conducting thin films for spacecraft applications*. NASA, 1994.

Kimball Physics. Fra-2x1-2 electron gun. online. URL `http://www.kimballphysics.com/electron_guns/specification_PDFs/FRA-2X1_Feb2013.pdf`. [Accessed November 6th, 2013].

J.R. Pierce. *Theory and Design of Electron Beams*. D. Van Nostrand Company, Inc, New York, 1949.

B. Polychronopulos and C.V. Goodall. A system for measuring and controlling the surface potential of rockets flown in the ionosphere. In R.J.L. Grard, editor, *Photon and Particle Interactions with Surfaces in Space*, volume 37 of *Astrophysics and Space Science Library*, pages 309–320. Springer Netherlands, 1973. ISBN 978-94-010-2649-9. doi: 10.1007/978-94-010-2647-5_18. URL `http://dx.doi.org/10.1007/978-94-010-2647-5_18`.

Carolyn K. Purvis, Henry B. Garrett, A. C. Whittlesey, and N. John Stevens. *Design Guidelines for Assessing and Controlling Spacecraft Charging Effects.* NASA, 1984.

S. Raj and D. D. Sarma. Optimization of a low-energy, high brightness electron gun for inverse photoemission spectrometers. *Review of Scientific Instruments*, 75(4):1020–1025, 2004. ISSN 0034-6748. doi: 10.1063/1.1647694.

Owen W. Richardson. Thermionic phenomena and the laws which govern them. `http://www.nobelprize.org/nobel_prizes/physics/laureates/1928/richardson-lecture.pdf`, December 1929. Accessed: 2013-07-09.

Alexander Roth. *Vacuum Technology*, pages 36–37. North-Holland Publishing Company, Amsterdam, 1976. ISBN 0-444-10801-7.

Jakub Siegel, Olexiy Lyutakov, Vladimír Rybka, Zdeňka Kolská, and Václav Švorčík. Properties of gold nanostructures sputtered on glass. *Nanoscale Research Letters*, 6:1–9, 2011. ISSN 1931-7573. URL `http://dx.doi.org/10.1186/1556-276X-6-96`. 10.1186/1556-276X-6-96.

Knut Olav Skyttemyr. Design and implementation of the electrical power system for the cubestar satellite. Master's thesis, University of Oslo, 2013.

Chetan Singh Solanki. *Solar Photovoltaics - Fundamentals, Technologies and Applications*, pages 110–112. PHI Learning Private Limited, New Delhi, 2009. ISBN 978-81-203-3760-2.

Spectrolab. Spectrolab photovoltaic products - 26.8% improved triple junction (itj) solar cells. online, a. URL `http://www.spectrolab.com/DataSheets/TNJCell/tnj.pdf`. [Accessed June 13th, 2012].

Spectrolab. Triple-junction terrestrial concentrator solar cells. online, b. URL `http://www.spectrolab.com/DataSheets/TerCel/tercell.pdf`. [Accessed November 4th, 2013].

Spectrolab. Spectrolab photovoltaic products - 28.3% ultra triple junction (utj) solar cells. online, c. URL `http://www.spectrolab.com/DataSheets/TNJCell/utj3.pdf`. [Accessed October 25th, 2013].

R.A. Synowicki, Jeffrey S. Hale, N.J. Ianno, John A. Woollam, and Paul D.Hambourger. Low earth orbit effects on indium tin oxide and polyester and comparison with laboratory simulations. *Surface and Coatings Technology*, 62(13):499 – 503, 1993. ISSN 0257-8972. doi: 10.1016/0257-8972(93)90290-5. URL `http://www.sciencedirect.com/science/article/pii/0257897293902905`.

Alan C. Tribble. *The Space Environment - Implications for Spacecraft Design*, page 8. Princeton University Press, New Jersey, 2003. ISBN 0-691-10299-6.

California Polytechnic State University. Cubesat design specification rev.12. `http://www.cubesat.org/index.php/documents/developers`, 2009. Accessed: 2013-07-09.

Hojun Yoon, David E. Joslin, Daniel C. Law, Dmitri Krut, Richard R. King, P. Vijayakumar, David Peterson, Jim Hanley, and Nasser H. Karam. Application of infrared reflecting (irr) coverglass on multijunction iii-v solar cells. In *booktitle*.

Appendix A

Submitted Papers

T. A. Bekkeng, E. S. Helgeby, A. Pedersen and J. I. Moen. In press 2013. m-NLP: multi-Needle Langmuir probe system for absolute electron density measurements and active spacecraft potential control on CubeSats.

Appendix B

ElectronGunMeasurementSystem

B.1 LabVIEW code

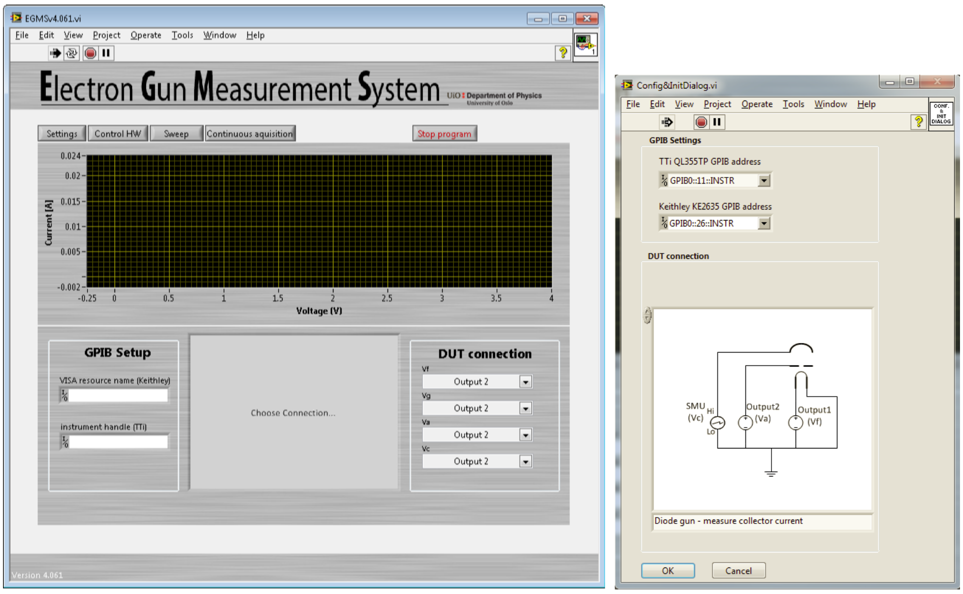

Vf: Output 2
Vg: Output 2
Va: Output 2
Vc: Output 2

TTi QL355TP GPIB address: GPIB0::11::INSTR
Keithley KE2635 GPIB address: GPIB0::26::INSTR
Diode gun - measure collector current

Figure B.1: Front panel of the settings page and the initialization dialogue.

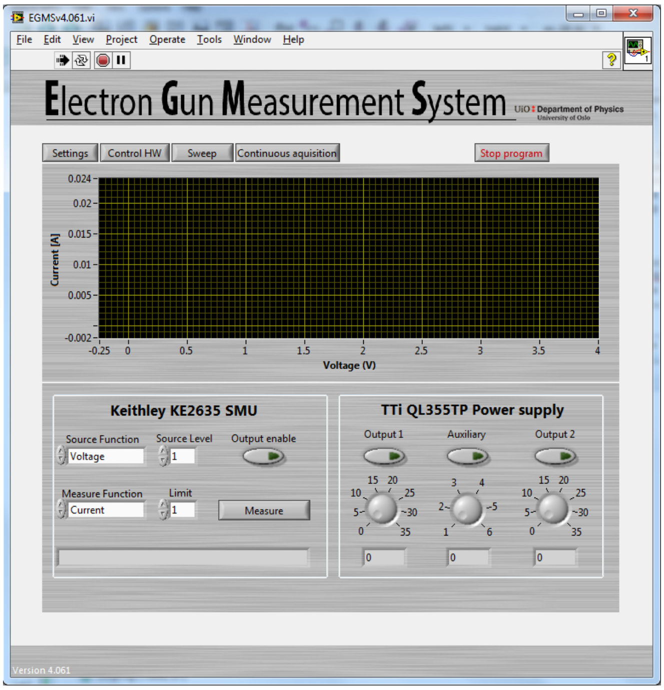

Source Function: Voltage
Source Level: 1
Measure Function: Current
Limit: 1
Output 1: 0
Auxiliary: 0
Output 2: 0

Figure B.2: Front panel of the control hardware page.

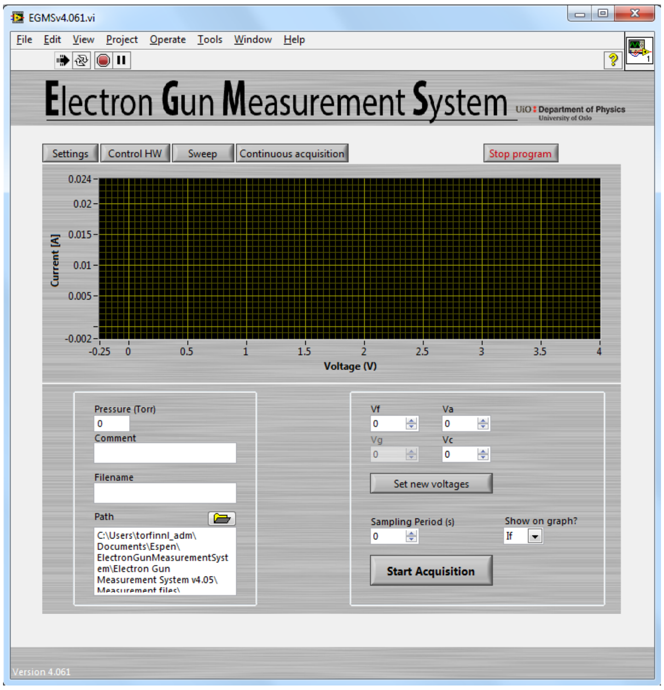

Pressure (Torr): 0
Comment:
Filename:
Path: C:\Users\torfinnl_adm\Documents\Espen\ElectronGunMeasurementSystem\Electron Gun Measurement System v4.05\Measurement files\
Vf: 0
Va: 0
Vg: 0
Vc: 0
Sampling Period (s): 0
Show on graph?: If

Figure B.3: Front panel of the continuous acquisition page.

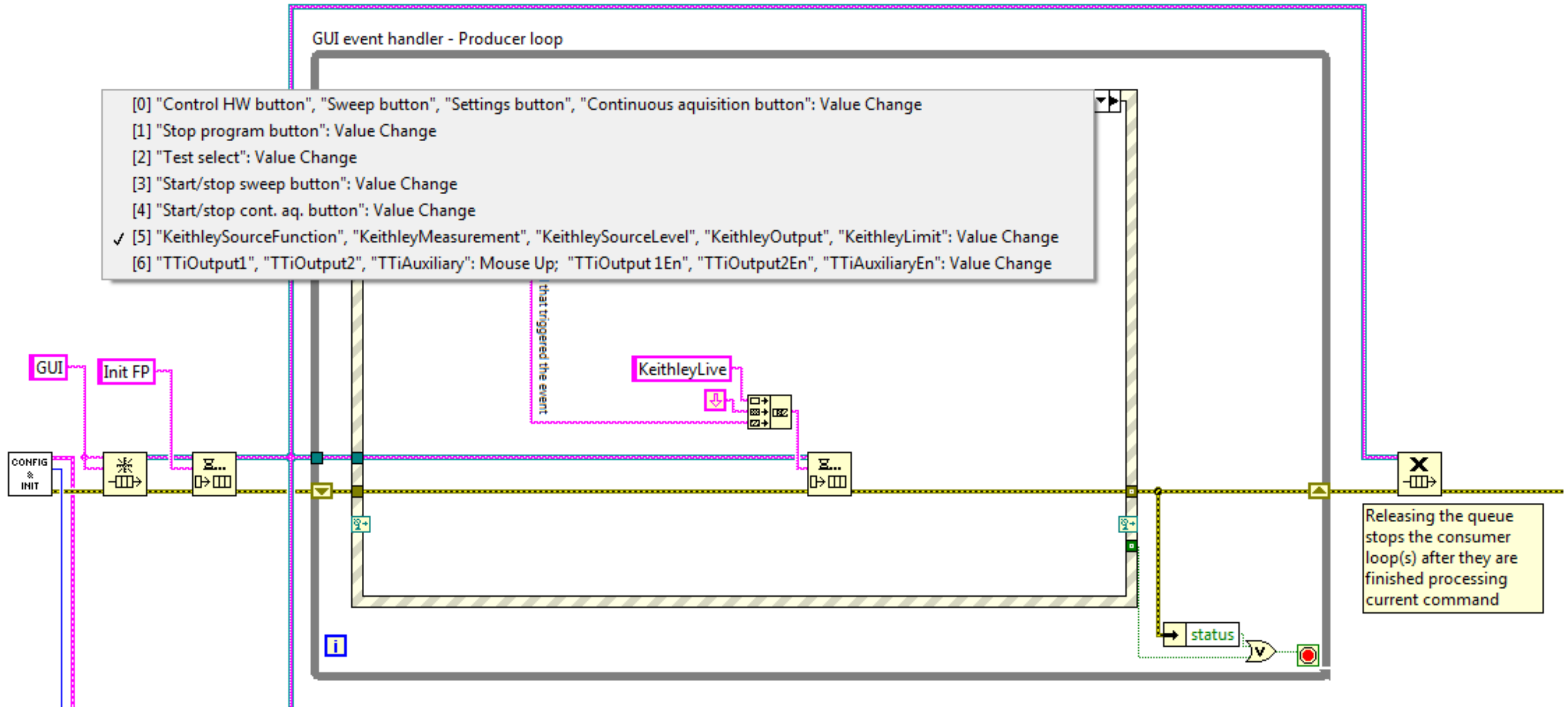

Figure B.4: Block diagram of the producer loop with all the different event cases shown in the grey box. The code for the other instances of the event case is omitted.

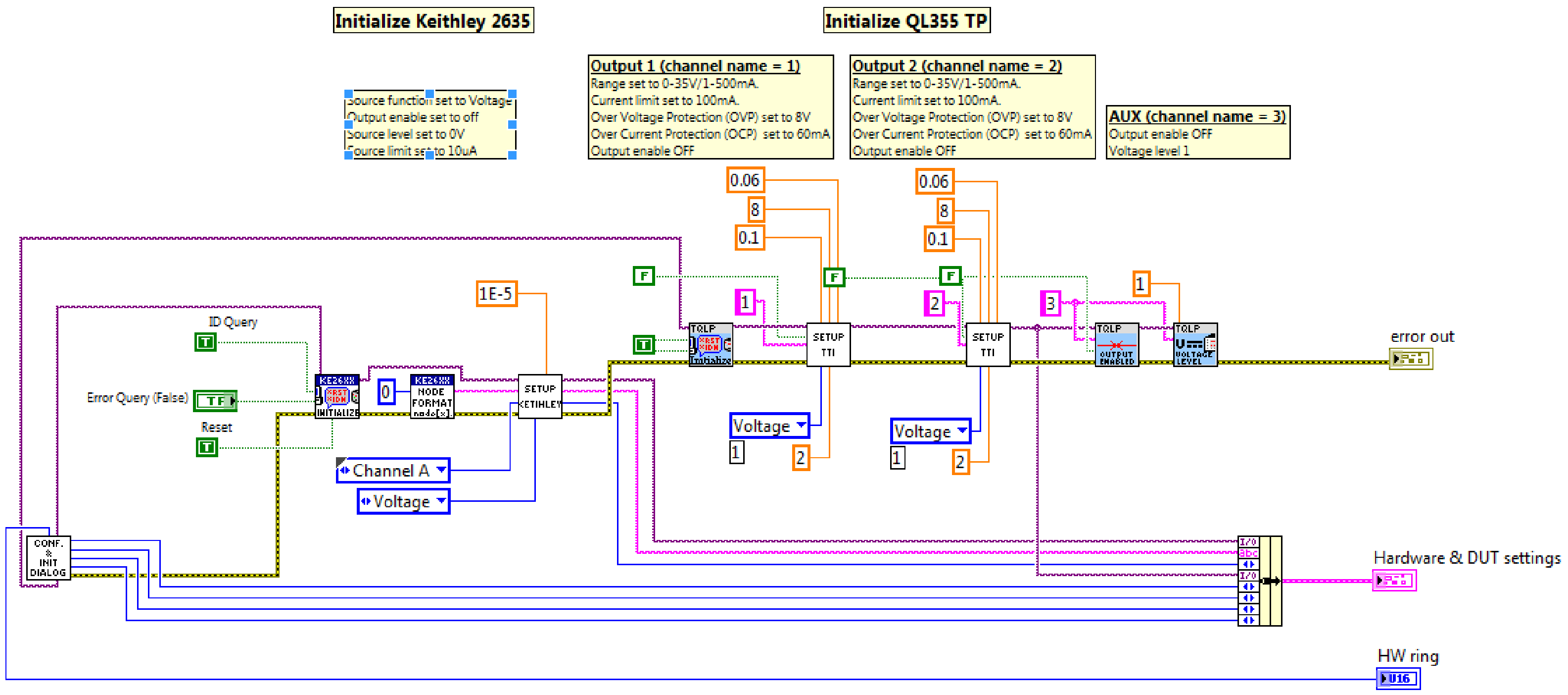

Figure B.5: Block diagram of the Congfig&Init.vi.

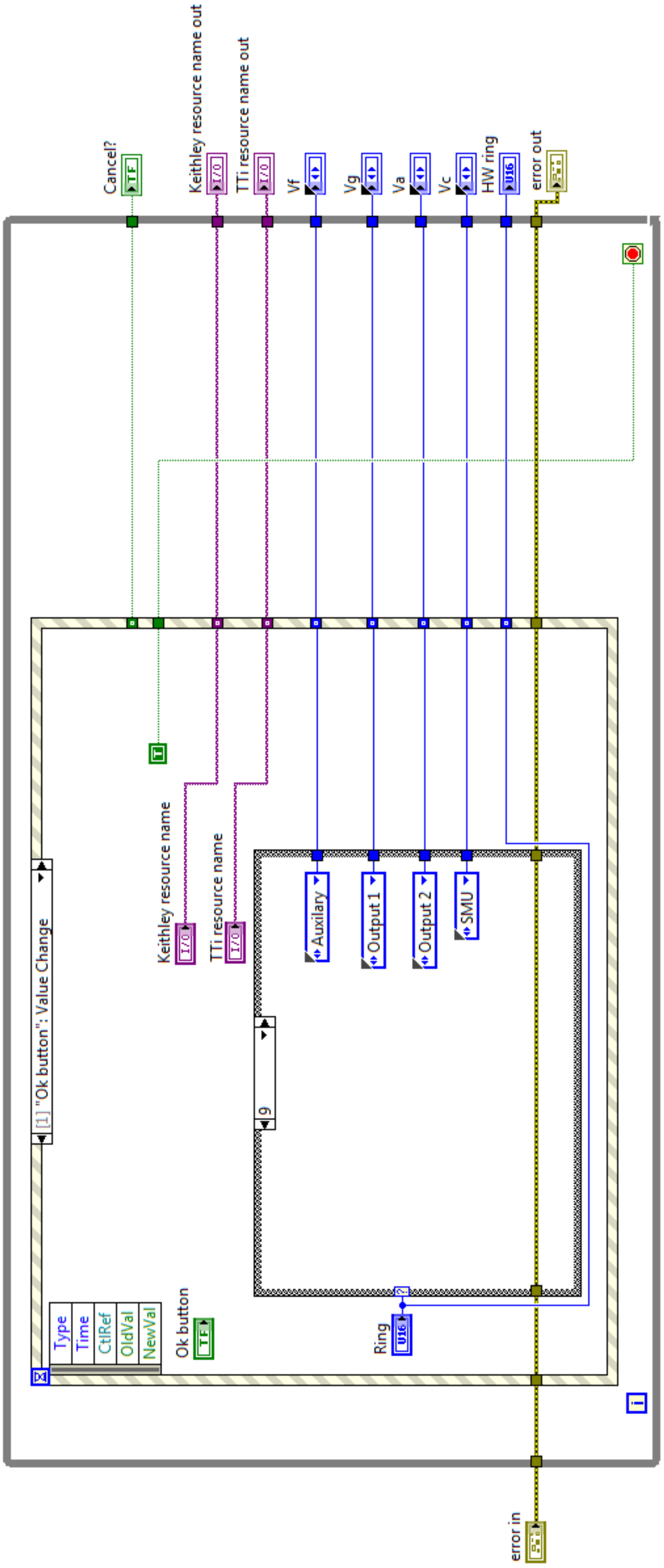

Figure B.6: Block diagram of the Congfig&InitDialog.vi. Only one instance of the case structure is shown.

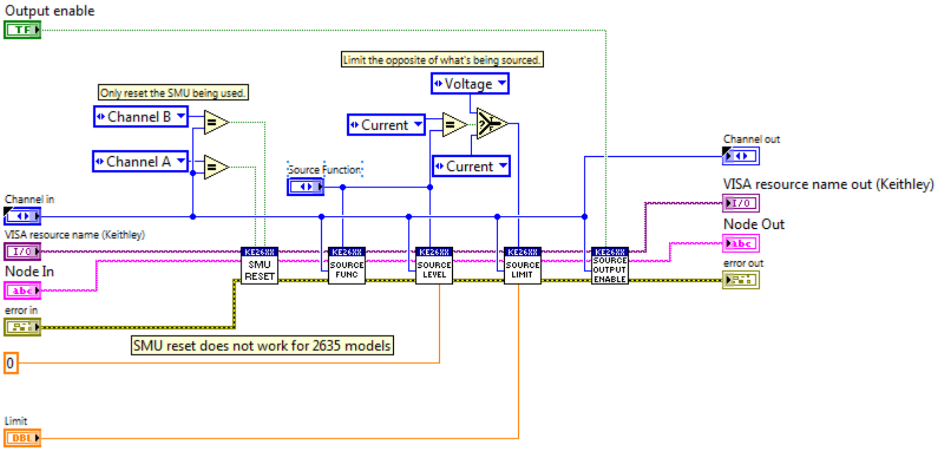

Figure B.7: Block diagram of the Keithley_Setup.vi.

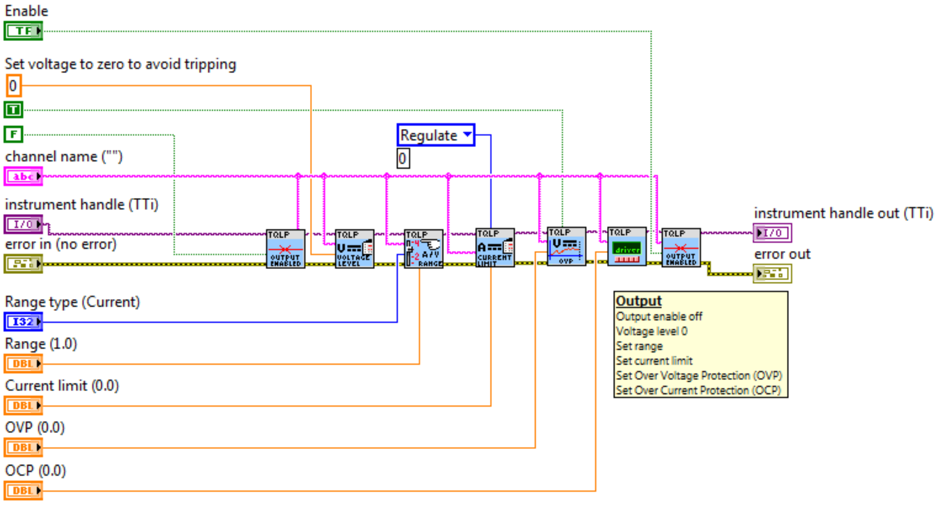

Figure B.8: Block diagram of the TTi_Setup.vi.

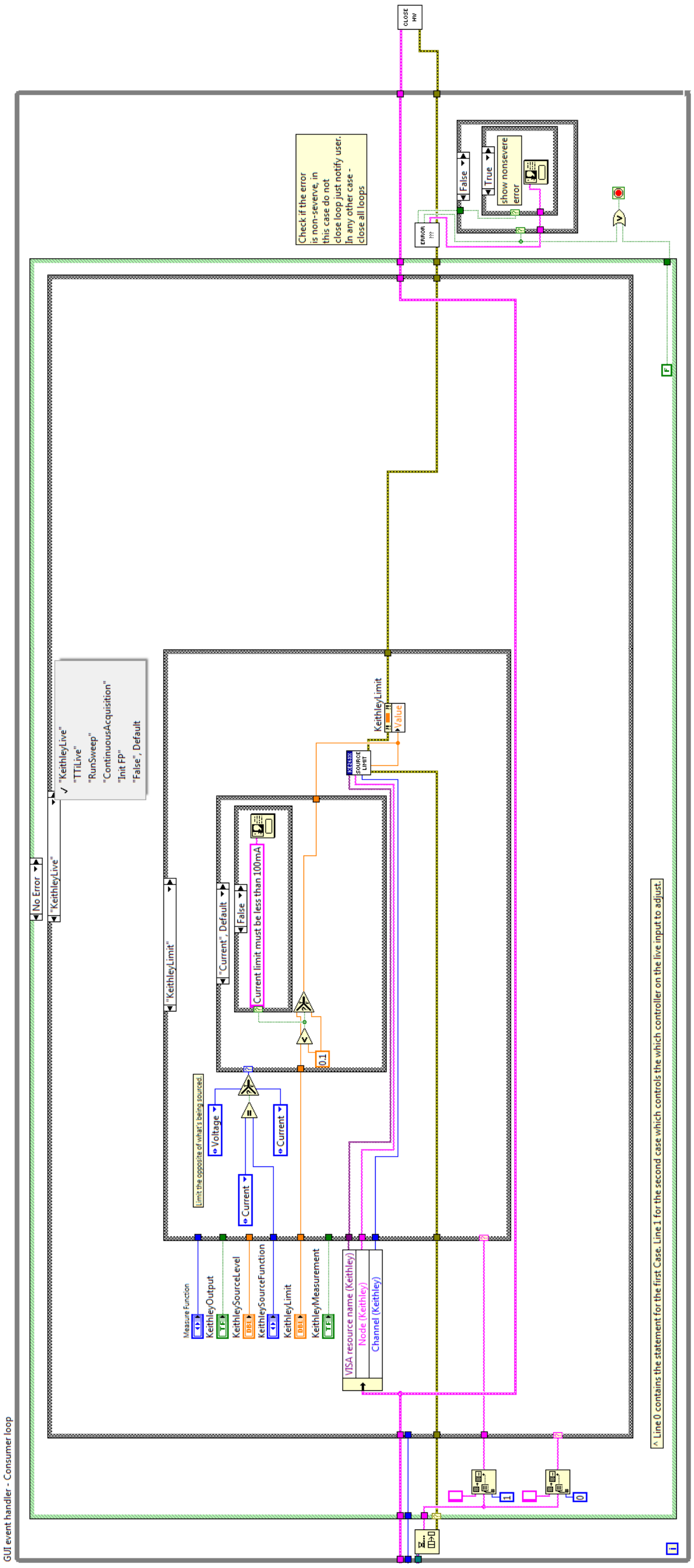

Figure B.9: Block diagram of the consumer loop with KeithleyLive case being active. Only the value which was changed and triggered the producer loop is programmed on the instrument. This case shows the KeithleyLimit case, the other cases for the Keithley live programming is omitted.

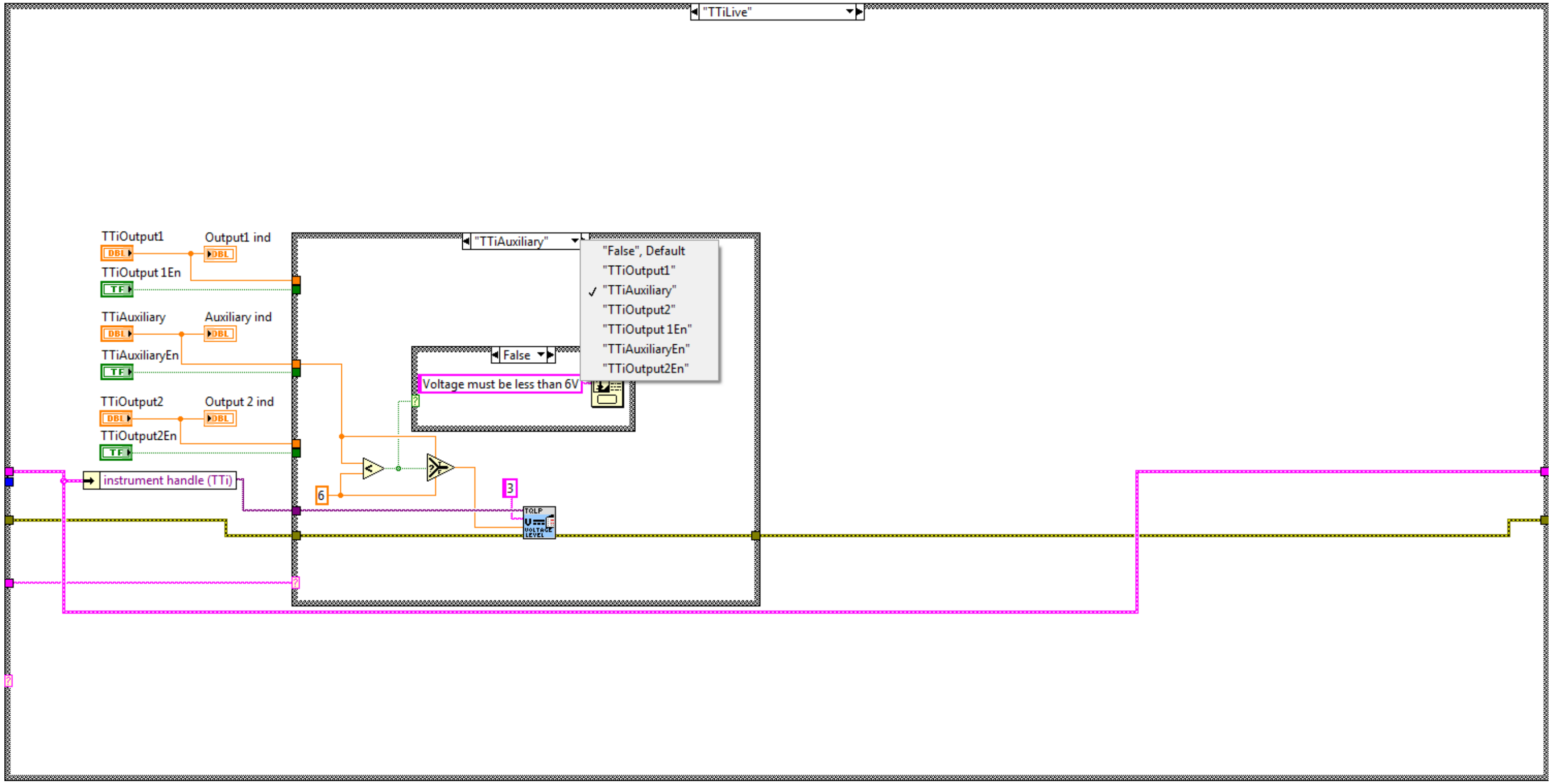

Figure B.10: Block diagram of the TTiLive case in the consumer loop. Only the value which was changed and triggered the producer loop is programmed on the instrument. This case shows the TTiAuxiliary case, the other cases for the TTi live programming is omitted.

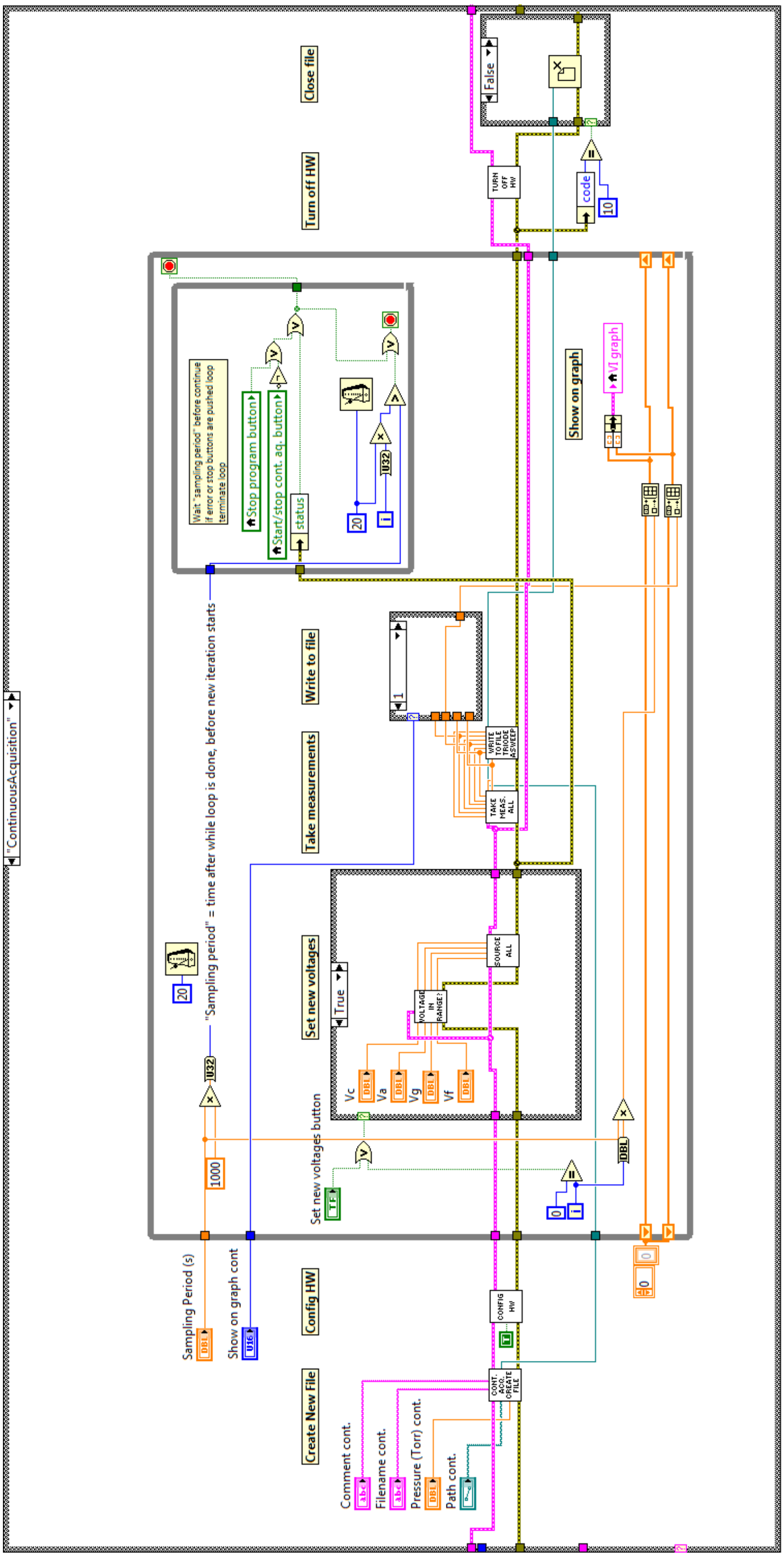

Figure B.11: Block diagram of the ContiniuousAcquisition case in the consumer loop.

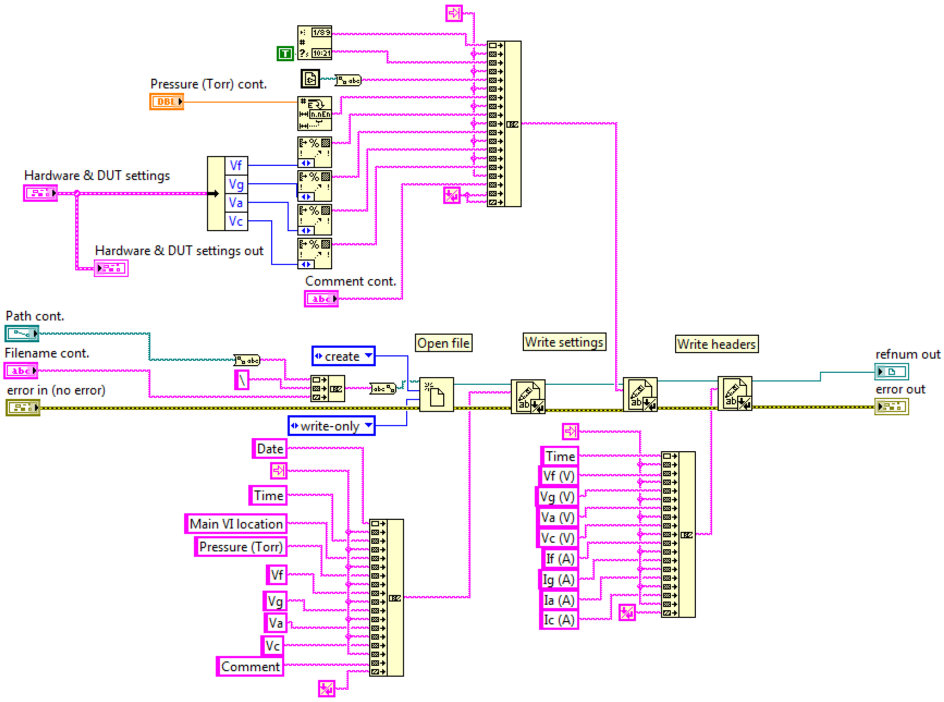

Figure B.12: Block diagram of the ContAcq_TextFileCreate.vi.

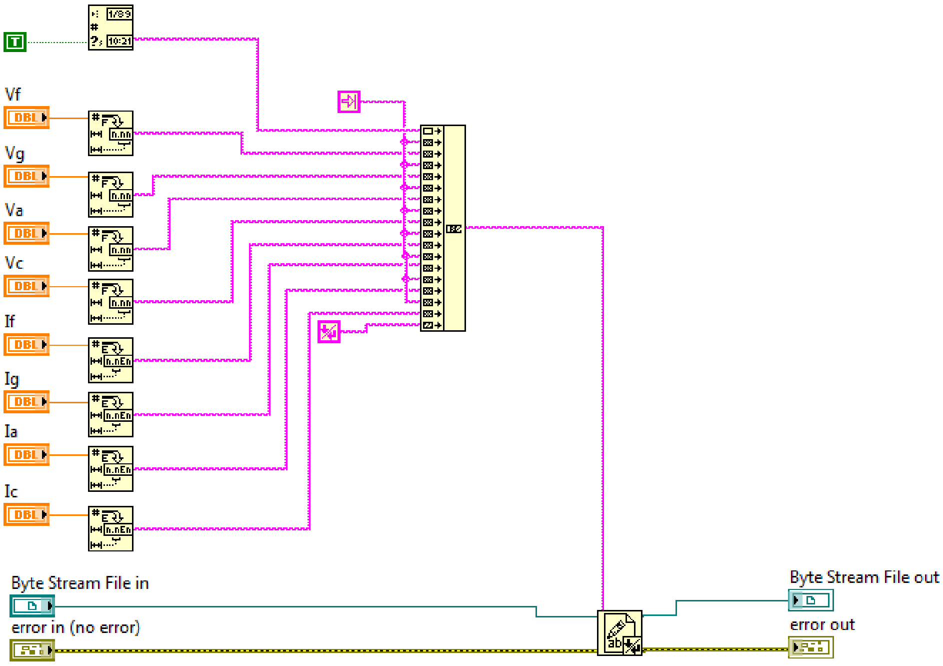

Figure B.13: Block diagram of the ContAcq_TextFileWrite.vi.

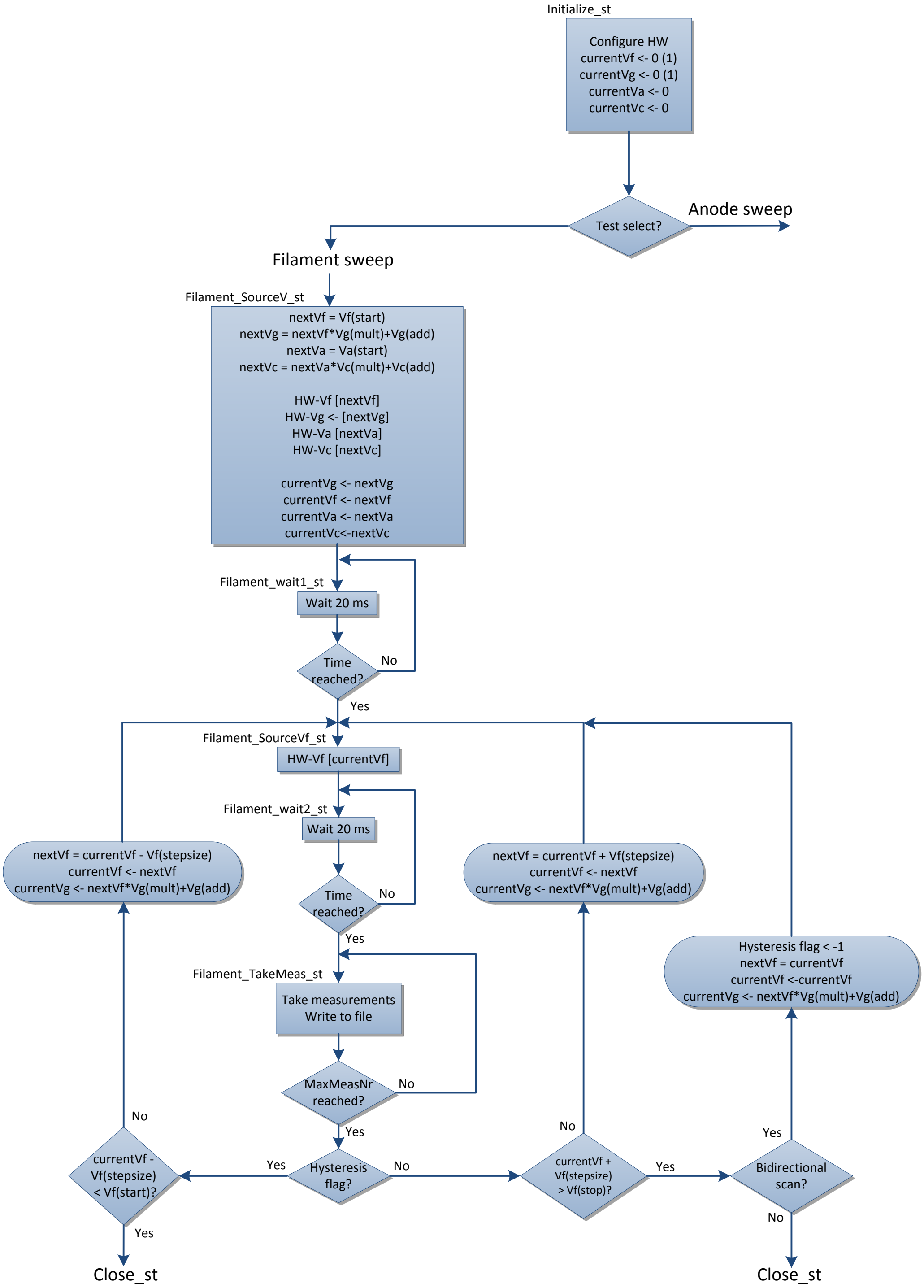

Figure B.14: Shows the state diagram for the filament sweep and anode sweep. This figure shows the initialize states and the states corresponding to the filament sweep.

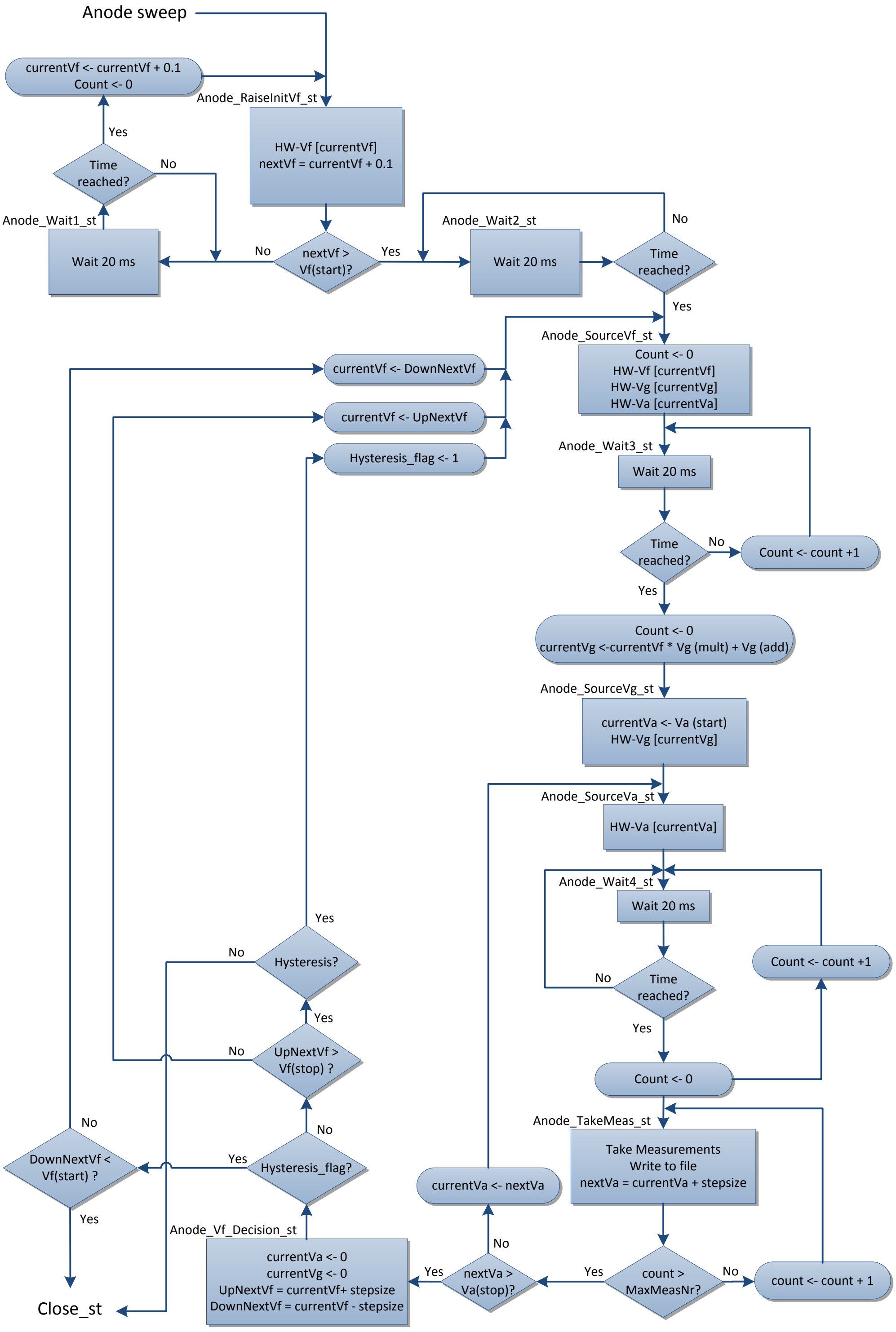

Figure B.15: Shows the state diagram for the filament sweep and anode sweep. This figure shows the states corresponding to the anode sweep.

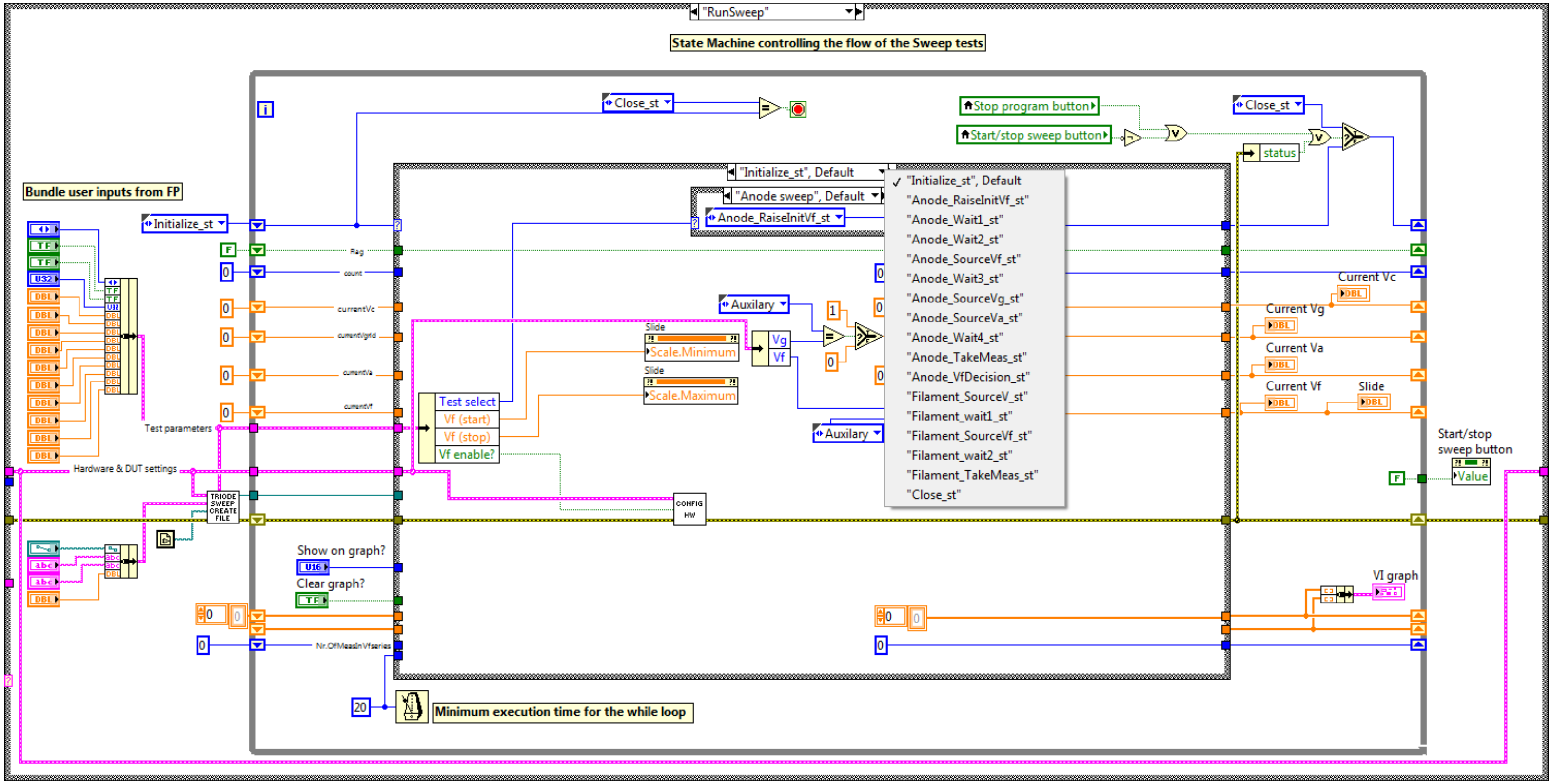

Figure B.16: Block diagram of the RunSweep case in the consumer loop. This figures shows the initialize state.

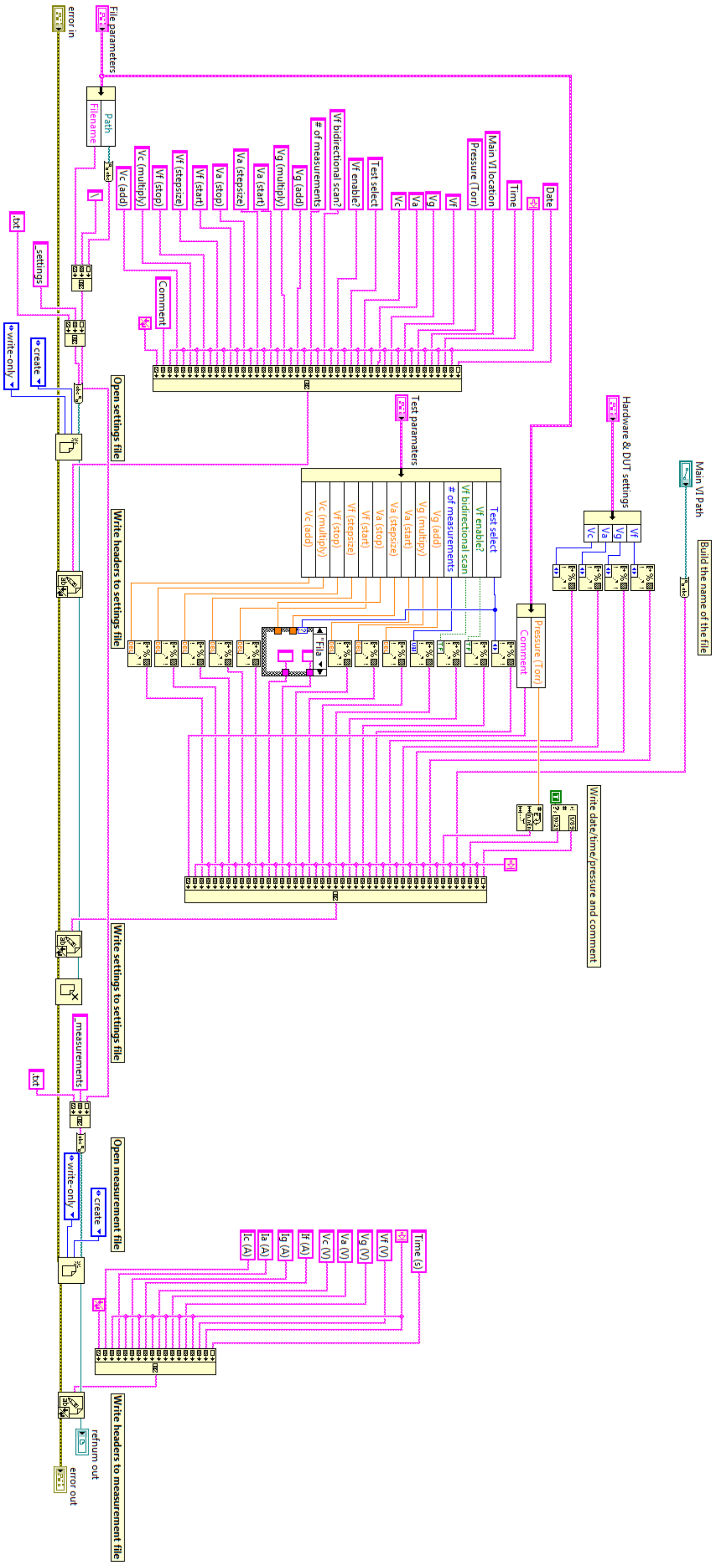

Figure B.17: Block diagram of the TriodeSweep_TextFileCreate.vi.

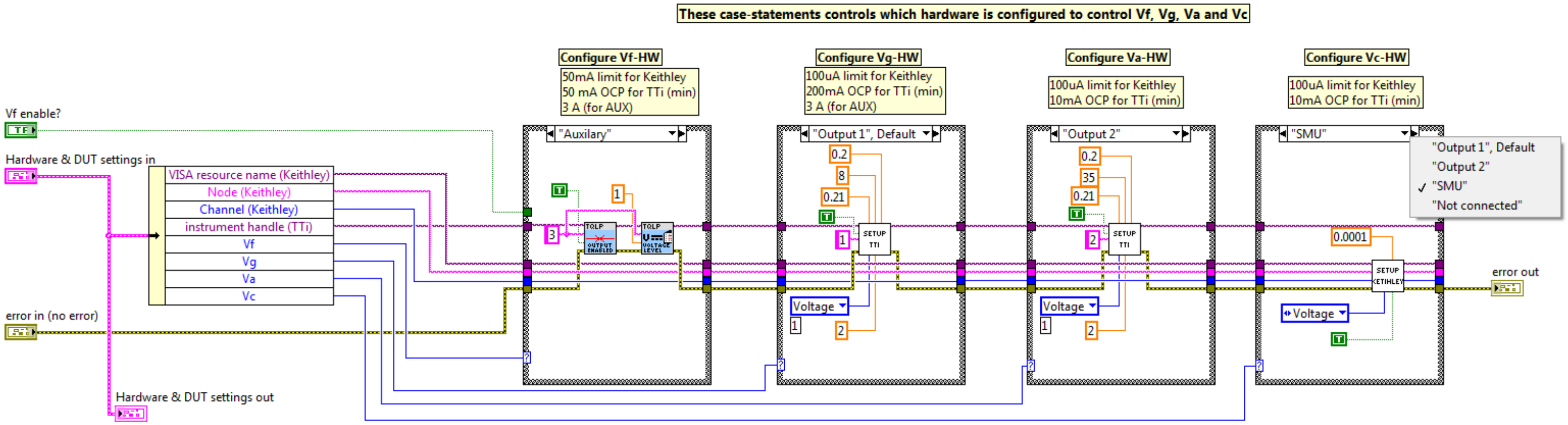

Figure B.18: Block diagram of the ConfigHW.vi. The other instances of the case structures are fairly similar and thus omitted.

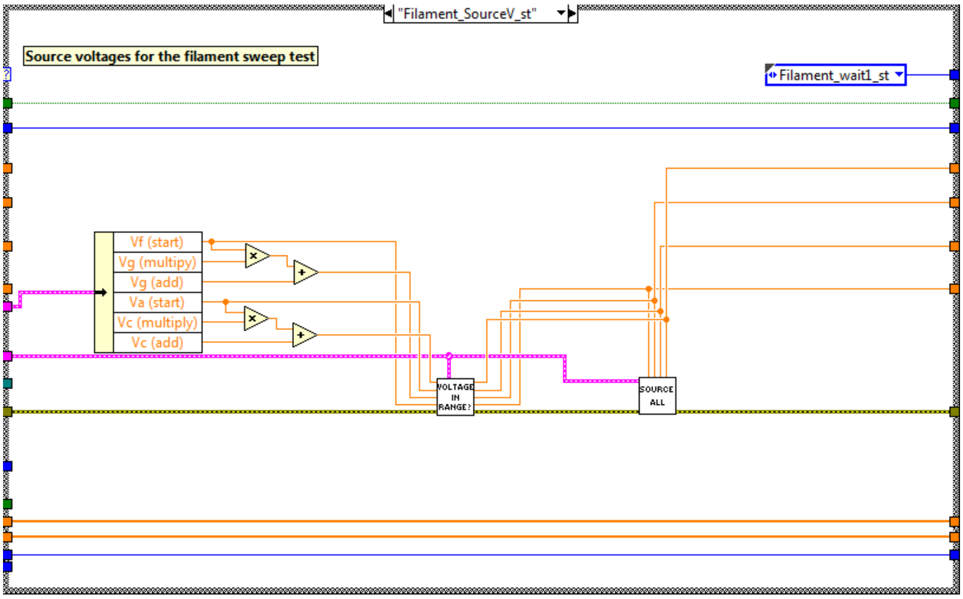

Figure B.19: Block diagram of the state Filament_SourveV_st in the statemachine in the RunSweep case.

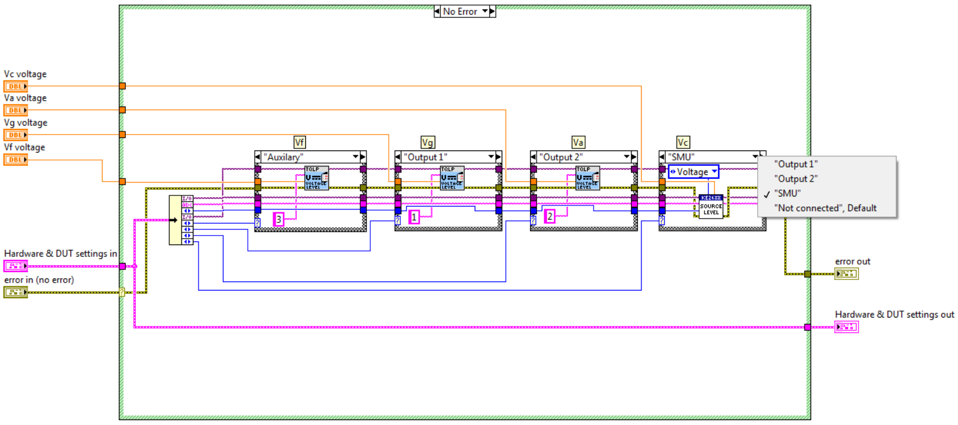

Figure B.20: Block diagram of the SourceAll.vi. The other instances of the case structures are fairly similar and thus omitted.

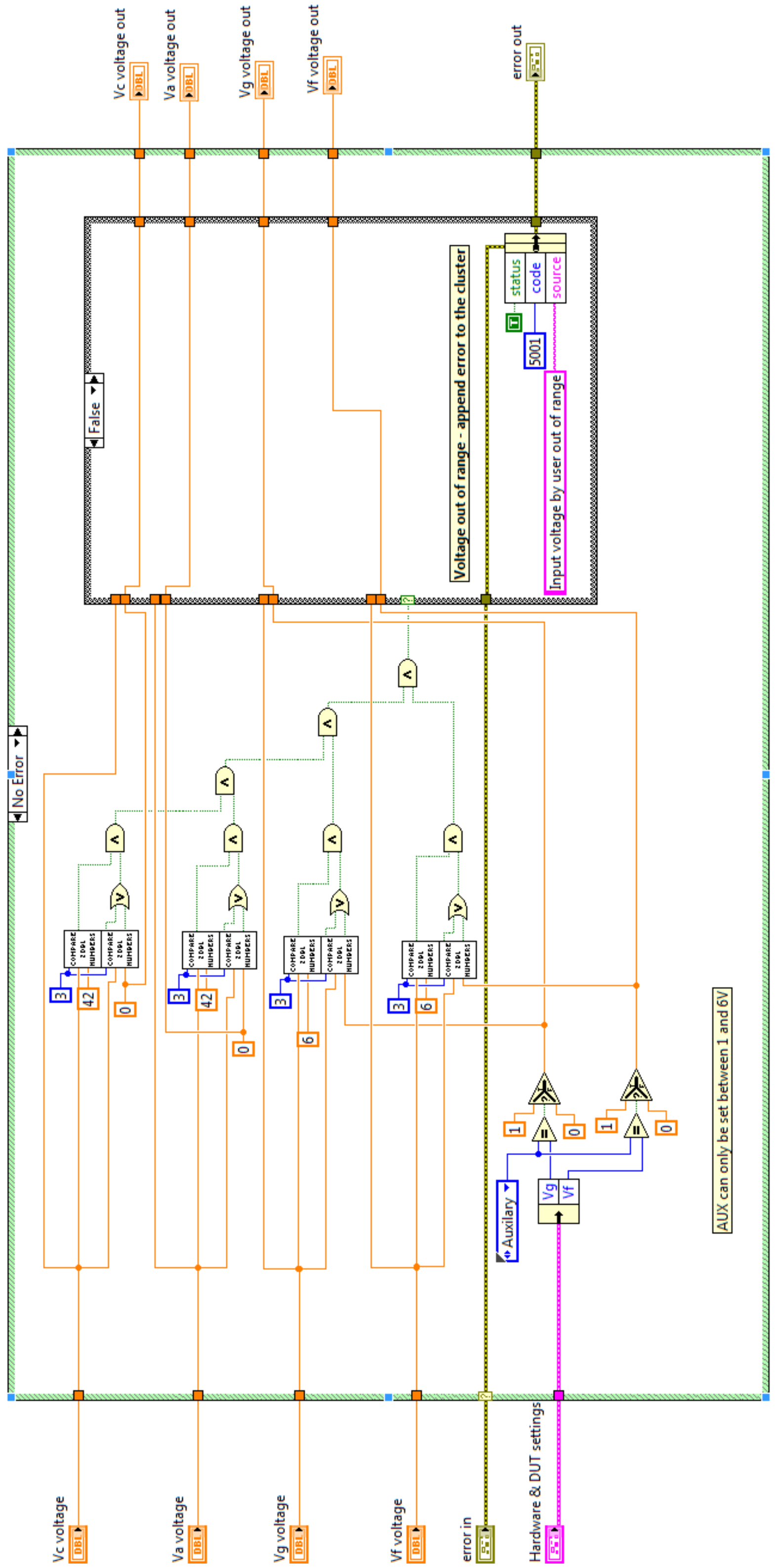

Figure B.21: Block diagram of the VoltageInRange.vi.

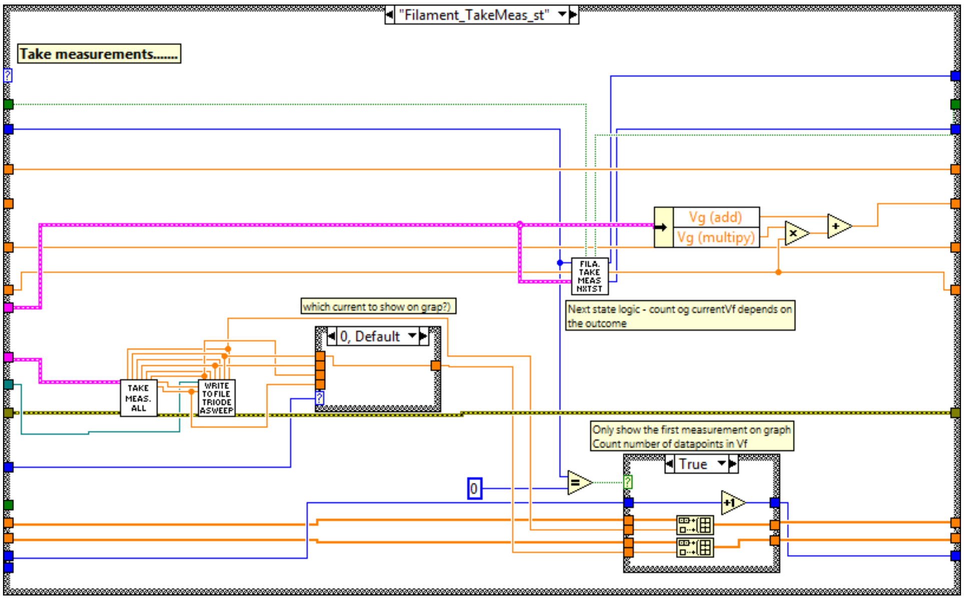

Figure B.22: Block diagram of the state Filament_TakeMeas_st in the statemachine in the RunSweep case.

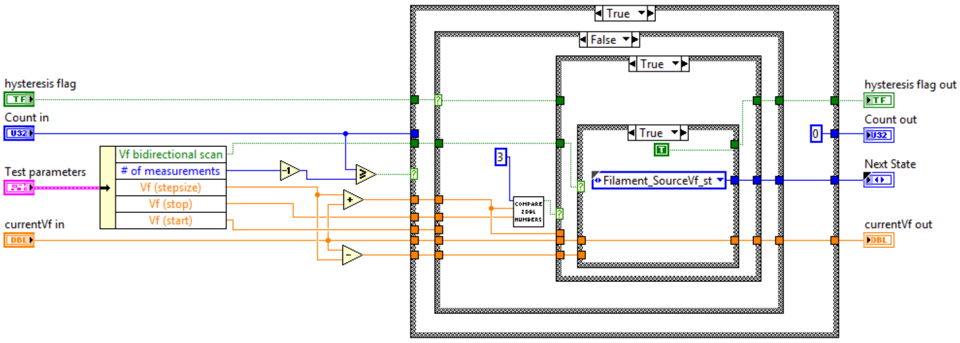

Figure B.23: Block diagram of the TriodeFSweep_TakeMeasNextSt.vi. The other instances of the case structure are omitted.

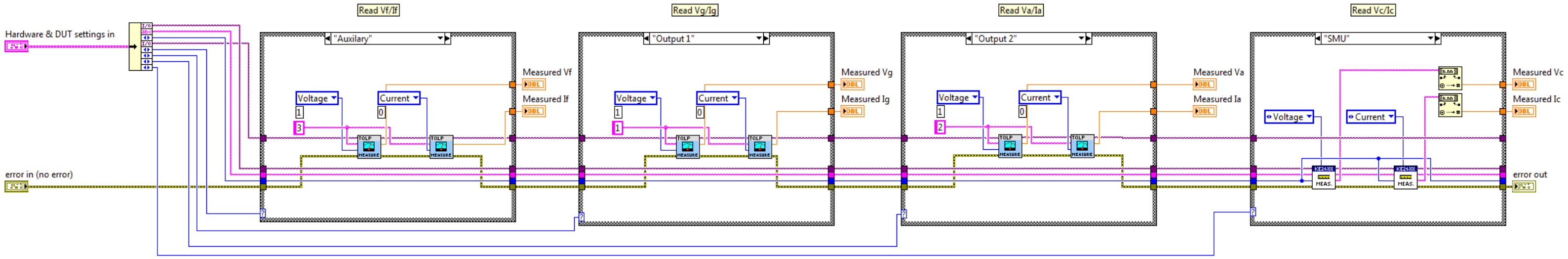

Figure B.24: Block diagram of the TakeMeasAll.vi. The other instances of the case structures are omitted

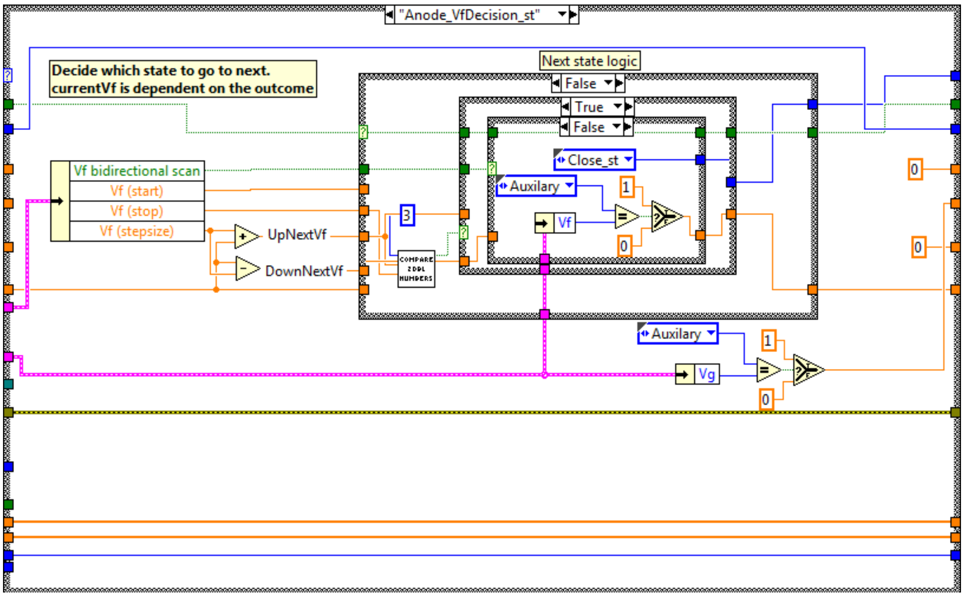

Decide which state to go to next.
currentVf is dependent on the outcome

Figure B.25: Block diagram of the state Anode_VfDecision_st in the statemachine in the RunSweep case. The other instances of the case structure is omitted.

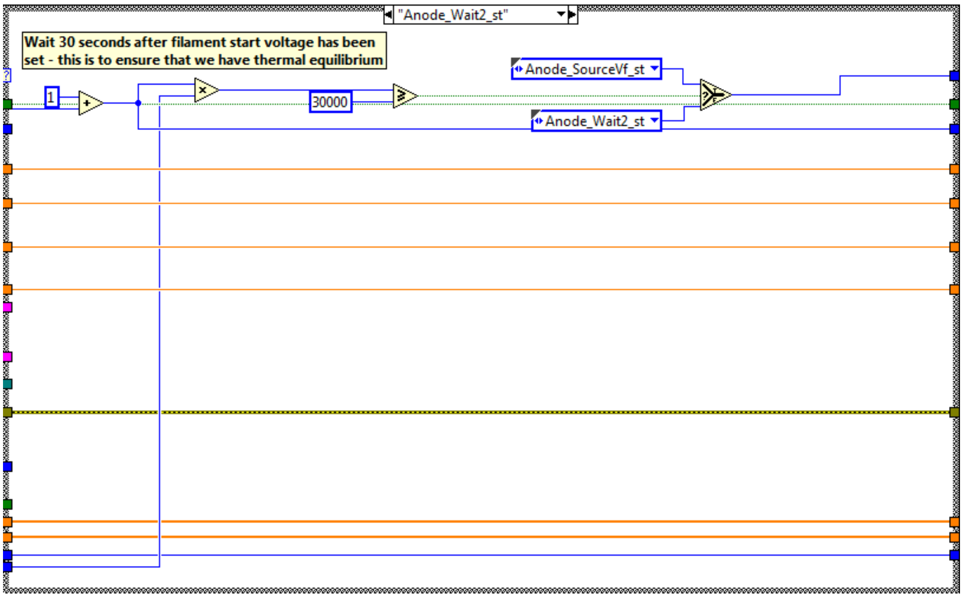

Wait 30 seconds after filament start voltage has been set - this is to ensure that we have thermal equilibrium

Figure B.26: Block diagram of the state Anode_Wait2_st in the statemachine in the RunSweep case.

B.2 Matlab code

B.2.1 anode_sweep.m

```
% ----------------------------------------------------------------------
% -- Plot data obtained with the EGMS.vi --------------------------------
% -- Electron Gun Measurement System - anode sweep ----------------------
% -- Author: Espen S. Helgeby, University of Oslo, 2013 -----------------
% ----------------------------------------------------------------------

clc
clear all
close all

% ----------------------------------------------------------------------
% ----- Please fill in user inputs -------------------------------------
% ----------------------------------------------------------------------
Vf_size = 12;           % How many anode sweeps (one for each Vf) to plot
Vf_size_up = 6;         % How many belongs to the up sweep?
Vf_size_down = 6;       % How many belongs to the down sweep?

plot_updown = 2;        % 1 = plot upsweep only,
                        % 2 = plot up -and down sweep,
                        % 3 = plot downsweep only

y_data_input = 'Ic';    % y-axis data to plot on the y-axis (If,Ig,Ia,Ic)
x_data_input = 'Va';    % x-axis data to plot on the x-axis (Vf,Vg,Va,Vc)

graph_title = '\textbf{Beam Current}'; % Fill in the title of the graph

plot_average = 'TRUE';  % TRUE  = plots the average of nr_of_measurements
                        % FALSE = plots only the first datapoints

plot_type = 1;          % 1 = plots semilogy,
                        % 2 = plots loglog,
                        % 3 = plots normal

plot_colour = 1;        % 0 = plots in black and white without grid
                        % 1 = plots in colour with grids

y_data_range = 'uA';    % nA = plots the y-axis in the nA-range
                        % uA = plots the y-axis in the uA-range
                        % mA = plots the y-axis in the mA-range

% Graph properties
axis_limits_on = 0;     % 1 = manually set axis limites
                        % 0 = automaticcaly set axis limit

axis_limits = [0 35 10^-5 2*10^1];
Y_ticks = [10^-5 10^-4 10^-3 10^-2 10^-1 10^0 10^1];
X_ticks = [0 5 10 15 20 25 30 35];
legend_location = 'SouthEast';
```

```

% ------ Load file and return measurement data --------------
[xdata,ydata,Vf_value] = load_anode_sweep(x_data_input, y_data_input,...
                                    plot_average, Vf_size, y_data_range);

% -----------------------------------------------------------------------
% ---- Plot the graph ---------------------------------------------------
% -----------------------------------------------------------------------

set(0, 'defaultTextInterpreter', 'latex');
fh = figure(1);

if ( strncmp(y_data_range, 'uA',2) == 1)
    y_data_range_text = '$\mu$A';
else
    y_data_range_text = y_data_range;
end

% Create a dummy to make the graph properties stay
if ( plot_type == 1 )
    semilogy(0,0)
elseif ( plot_type == 2 )
    loglog(0,0);
elseif ( plot_type == 3 )
    plot(0,0);
else
    warning('Unexpected plot type.')
end
hold on

title(['',graph_title],'FontSize',16,'FontWeight','bold');

if (axis_limits_on == 1)
    axis(axis_limits);
end

x_label = horzcat(x_data_input, ' (', 'V)');
xlabel(x_label,'FontSize',14);
y_label = horzcat(y_data_input, ' (', y_data_range_text, ')');
ylabel(y_label,'FontSize',14);

if (plot_colour == 0)
    set(gca, 'Box', 'off' );  % Only show the standard x -and y axis
    set(gca, 'TickDir','out');% Make the tick marks point out of the graph
    set(gca,'FontSize',12)    % Change axis font size gca=get current axis.
    set(fh, 'color', 'white');% sets the color to white
    set(gca, 'YTick', Y_ticks );
    set(gca, 'XTick', X_ticks );
    grid off
elseif (plot_colour == 1)
    grid on;
    hold all;
else
    warning('Unexpected plot type.')
```

```
end

% Plot up sweep
if ( (plot_updown == 1) || (plot_updown == 2))

    for i=1: 1: Vf_size_up

        if ( plot_type == 1 )
            h(i)=semilogy( xdata(:,i),ydata(:,i) );
        elseif ( plot_type == 2 )
            h(i)=loglog( xdata(:,i),ydata(:,i) );
        elseif ( plot_type == 3 )
            h(i)=plot( xdata(:,i),ydata(:,i) );
        else
            warning('Unexpected plot type')
        end

        if (plot_colour == 0)
            set(h(i),'LineStyle', '-', 'LineWidth', 1, 'Color', 'black',...
                     'Marker', 'o', 'MarkerFaceColor', [0.5 0.5 0.5],...
                     'MarkerEdgeColor', [0 0 0], 'MarkerSize', 3.0);

            % Write the name of the series at the last datapoint
            current_Vf_value = num2str(Vf_value(i),'%.1f');
            Vf_value_text = horzcat('Vf = ', current_Vf_value, ' V');
            y_last = ydata(length(ydata(:,i)),i);
            text(35,y_last, Vf_value_text,'FontSize',9);

        elseif (plot_colour == 1)
            set(h(i), 'LineStyle', '-', 'LineWidth', 0.7, 'Marker', 'o',...
                 'MarkerSize', 3.0 ,'MarkerFaceColor', get(h(i), 'Color'));
            color_order(:,i) = get(h(i), 'Color');

            % Write the name of the series at the last datapoint;
            current_Vf_value = num2str(Vf_value(i),'%.1f');
            Vf_value_text = horzcat('Vf = ', current_Vf_value, ' V');
            y_last = ydata(length(ydata(:,i)),i); % Last y-value
            legend_str{i} = Vf_value_text;
        else
            warning('Unexpected plot type.')
        end

    end

     if (plot_colour == 1)
         legend([h(1:i)], (legend_str{:}),'Location',legend_location);
     else
         %do nothing
     end

end


if ( (plot_updown == 2) || (plot_updown == 3) )
```

```

    j=0;
    for i=(Vf_size/2)+1: 1: Vf_size

        if ( plot_type == 1 )
            h(i)=semilogy( xdata(:,i),ydata(:,i) );
        elseif ( plot_type == 2 )
            h(i)=loglog( xdata(:,i),ydata(:,i) );
        elseif ( plot_type == 3 )
            h(i)=plot( xdata(:,i),ydata(:,i) );
        else
            warning('Unexpected plot type. No plot created.')
        end

        % Write the name of the series at the last datapoint
        current_Vf_value = num2str(Vf_value(i),'%.1f');
        Vf_value_text = horzcat('Vf = ', current_Vf_value, ' V');
        y_last = ydata(length(ydata(:,i)),i); % Last y-value

        if (plot_colour == 0)
           set(h(i), 'LineStyle', '-', 'LineWidth', 1, 'Color', 'black',...
           'Marker', 'o', 'MarkerFaceColor', [1 1 1], 'MarkerEdgeColor',...
           [0 0 0], 'MarkerSize', 3.0);

            if (plot_updown == 3)
                text(35,y_last, Vf_value_text,'FontSize',9,'FontWeight',...
                                                            'normal');
            elseif (plot_updown == 2)
                % do nothing - already been written to graph
            end

        elseif (plot_colour == 1)
            if (plot_updown == 2)
                set(h(i), 'LineStyle', '-', 'LineWidth', 0.7, 'Color',...
                           color_order(:,(length(color_order(1,:))-j)),...
                           'Marker', 'o', 'MarkerSize', 3.0);
            elseif (plot_updown == 3)
                set(h(i), 'LineStyle', '-', 'LineWidth', 0.7);
                set(h(i), 'Marker', 'o', 'MarkerSize', 3.0);
            end
            j=j+1;

        else
            warning('Unexpected plot type. No plot created.')

        end

    end

    if (plot_colour == 1)
        % Append information to legend about up/down sweep
        if (plot_updown == 2)
            h((Vf_size/2)+1) = scatter(0,0,0.5,[0.45 0.45 0.45],'filled');
            legend_str{Vf_size/2+1} = 'Up sweep';
```

```
            h((Vf_size/2)+2) = scatter(0,0,0.5,[0.45 0.45 0.45]);
            legend_str{Vf_size/2+2} = 'Down sweep';

            % Plot the legend
            legend([h(1:Vf_size/2+2)], (legend_str{:}),'Location',legend_location);
        else
            legend([h(1:i)], (legend_str{:}),'Location',legend_location);
        end

    else
        % do nothing
    end

end
```

B.2.2 load_anode_sweep.m

```matlab
% ----------------------------------------------------------------------------
% -- Function load_anode_sweep -----------------------------------------------
% -- This function fetch data from an anode sweep measurement file ----------
% -- obtained with the LabVIEW program EGMS.vi -------------------------------
% -- Author Espen S. Helgeby, Univeristy of Oslo, 2013 ------------------------
% ----------------------------------------------------------------------------

function [xdata,ydata,Vf_value] = load_anode_sweep(x_data_input,...
                           y_data_input,plot_average,Vf_size, y_data_range)

% ------------------------------------------------
% ----- Read measurements and settings file -----
% ------------------------------------------------

% Promt for settings file with .txt extension
DialogTitle = 'Select settings file';
[filename, pathname] = uigetfile('*.txt',DialogTitle);
filename = horzcat(pathname,filename);

% Open file
fid = fopen(filename,'r');

% Read file
settings_headers = textscan(fid, '%s', 23, 'delimiter', '\t');
settings_headers = settings_headers{1,1}';
format = '%s%s%s%f%s%s%s%s%s%s%s%f%f%f%f%f%f%f%f%f%f%s';
settings_data = textscan(fid, format, 23, 'delimiter', '\t');

% Close file
fclose(fid);

% Arrange into more readable variables
Va_start = settings_data{1,15};
Va_stepsize = settings_data{1,16};
Va_stop = settings_data{1,17};
Vf_start = settings_data{1,18};
Vf_stepsize = settings_data{1,19};
Vf_stop = settings_data{1,20};
nr_of_measurements = settings_data{1,12};
Vf_bidirectional = settings_data{1,11};

% Promt for measurements file with .txt extension
DialogTitle = 'Select measurements file';
[filename, pathname] = uigetfile('*.txt',DialogTitle);
filename = horzcat(pathname,filename);

% Open file
fid = fopen(filename,'r');

% Read file
```

```
measurements_headers = textscan(fid, '%s', 9, 'delimiter','\t');
measurements_headers = measurements_headers{1,1}';
measurements_data = textscan(fid, '%s %f %f %f %f %f %f %f %f');

% Close file
fclose(fid);

% Arrange into more readable variables
time = [measurements_data{:,1}];
Vf = [measurements_data{:,2}];
Vg = [measurements_data{:,3}];
Va = [measurements_data{:,4}];
Vc = [measurements_data{:,5}];
If = [measurements_data{:,6}];
Ig = [measurements_data{:,7}];
Ia = [measurements_data{:,8}];
Ic = [measurements_data{:,9}];

% Number of datapoints in one anode sweep
Va_size = ( ((Va_stop-Va_start) / Va_stepsize) +1 ) * nr_of_measurements;

% Arrange the datapoints which belongs to the same anode sweep in one array
for i=0:Vf_size-1
    start_array = i*Va_size+1;
    stop_array = (i+1)*Va_size;
    Vf_series(:,i+1) = Vf(start_array:stop_array);
    Vg_series(:,i+1) = Vg(start_array:stop_array);
    Va_series(:,i+1) = Va(start_array:stop_array);
    Vc_series(:,i+1) = Vc(start_array:stop_array);
    If_series(:,i+1) = If(start_array:stop_array);
    Ig_series(:,i+1) = Ig(start_array:stop_array);
    Ia_series(:,i+1) = Ia(start_array:stop_array);
    Ic_series(:,i+1) = Ic(start_array:stop_array);
    i=i+1;
end

% -------------------------------------------------------
% -- Pick out the first measurement in each series -----
% -------------------------------------------------------

j=1;
k=1;
% Loop through all the Vf series
for l=0:Vf_size-1
    % Loop through the anode sweep
    for i=0:Va_size-1
        if j == 1
            Vf_series_first(k,l+1) = Vf_series(i+1,l+1);
            Vg_series_first(k,l+1) = Vg_series(i+1,l+1);
            Va_series_first(k,l+1) = Va_series(i+1,l+1);
            Vc_series_first(k,l+1) = Vc_series(i+1,l+1);
            If_series_first(k,l+1) = If_series(i+1,l+1);
            Ig_series_first(k,l+1) = Ig_series(i+1,l+1);
            Ia_series_first(k,l+1) = Ia_series(i+1,l+1);
```

```
            Ic_series_first(k,l+1) = Ic_series(i+1,l+1);
            k=k+1;
        end

        if j == nr_of_measurements
            j=1;
        else
            j=j+1;
        end
        i=i+1;
    end
    k=1;
    l=l+1;
end

% ------------------------------------------------------
% ---  Average all the measurements in each series -----
% ------------------------------------------------------

j=1;
k=1;
Vf_sum = 0;
Vg_sum = 0;
Va_sum = 0;
Vc_sum = 0;
If_sum = 0;
Ig_sum = 0;
Ia_sum = 0;
Ic_sum = 0;
% Loop through all the Vf series
for l=0:Vf_size-1
    % Loop through the anode sweep
    for i=0:Va_size-1
        Vf_sum = Vf_sum + Vf_series(i+1,l+1);
        Vg_sum = Vg_sum + Vg_series(i+1,l+1);
        Va_sum = Va_sum + Va_series(i+1,l+1);
        Vc_sum = Vc_sum + Vc_series(i+1,l+1);
        If_sum = If_sum + If_series(i+1,l+1);
        Ig_sum = Ig_sum + Ig_series(i+1,l+1);
        Ia_sum = Ia_sum + Ia_series(i+1,l+1);
        Ic_sum = Ic_sum + Ic_series(i+1,l+1);
        if j == nr_of_measurements
            Vf_series_average(k,l+1) = Vf_sum/nr_of_measurements;
            Vg_series_average(k,l+1) = Vg_sum/nr_of_measurements;
            Va_series_average(k,l+1) = Va_sum/nr_of_measurements;
            Vc_series_average(k,l+1) = Vc_sum/nr_of_measurements;
            If_series_average(k,l+1) = If_sum/nr_of_measurements;
            Ig_series_average(k,l+1) = Ig_sum/nr_of_measurements;
            Ia_series_average(k,l+1) = Ia_sum/nr_of_measurements;
            Ic_series_average(k,l+1) = Ic_sum/nr_of_measurements;
            Vf_sum = 0;
            Vg_sum = 0;
            Va_sum = 0;
            Vc_sum = 0;
```

```
            If_sum = 0;
            Ig_sum = 0;
            Ia_sum = 0;
            Ic_sum = 0;
            j=1;
            k=k+1;
        else
            j=j+1;
        end
        i=i+1;
    end

    Vf_value(l+1) = Vf_series_average(k-1,l+1);
    k=1;
    l=l+1;
end

% -------------------------------------------------------------------
% ----  Decide which variables to return ----------------------------
% -------------------------------------------------------------------

switch x_data_input

    case 'Vf'
        % Average or first number?
        if ( strncmp(plot_average, 'TRUE',4) == 1)
            xdata = Vf_series_average;
        else
            xdata = Vf_series_first;
        end

    case 'Vg'
        % Average or first number?
        if ( strncmp(plot_average, 'TRUE',4) == 1)
            xdata = Vg_series_average;
        else
            xdata = Vg_series_first;
        end

    case 'Va'
        % Average or first number?
        if ( strncmp(plot_average, 'TRUE',4) == 1)
            xdata = Va_series_average;
        else
            xdata = Va_series_first;
        end

    case 'Vc'
        % Average or first number?
        if ( strncmp(plot_average, 'TRUE',4) == 1)
            xdata = Vc_series_average;
        else
            xdata = Vc_series_first;
        end
```

```

    otherwise
        warning('Unexpected input.')
end

switch y_data_input

    case 'If'
        % Average or first number?
        if ( strncmp(plot_average, 'TRUE',4) == 1)
            ydata = If_series_average;
        else
            ydata = If_series_first;
        end

    case 'Ig'
        % Average or first number?
        if ( strncmp(plot_average, 'TRUE',4) == 1)
            ydata = Ig_series_average;
        else
            ydata = Ig_series_first;
        end

    case 'Ia'
        % Average or first number?
        if ( strncmp(plot_average, 'TRUE',4) == 1)
            ydata = Ia_series_average;
        else
            ydata = Ia_series_first;
        end

    case 'Ic'
        % Average or first number?
        if ( strncmp(plot_average, 'TRUE',4) == 1)
            ydata = Ic_series_average;
        else
            ydata = Ic_series_first;
        end

    otherwise
        warning('Unexpected input.')
end

switch y_data_range
    case 'nA'
        ydata = ydata./10^-9;
    case 'uA'
        ydata = ydata./10^-6;
    case 'mA'
        ydata = ydata./10^-3;
    otherwise
        warning('Unexpected range type.')
end
```

Appendix C

A Head Start on the Future Work

C.1 Driver Electronics

The proposed connector between the m-NLP system and the electron gun is the Datamate M80 connector from Harwin with known outgassing specifications[1]. As of now, the current m-NLP system for CubeSTAR incorporates one such connector for the electron gun with the following pin-out:

1. GND
2. I/O pin from FPGA
3. +3.3 V
4. +12 V
5. No connect
6. +5 V

The requirement of having negative bias polarity on the electron gun makes the design more complex. The electronics for generating the voltages can be implemented as an integrated circuit (IC) or built from discrete components. Using a boost converter in a small IC package will give a smaller footprint on the base PCB than building the electronics with discrete components. The I/O pin from the FPGA is intended to control the boost converts either directly, for those supporting such operation, or by for instance filtering a pulse width modulated signal to generate a DC voltage for the booster. Care should be taken to choose boost converts with minimum noise which is stable under no-load conditions.

---

[1] http://www.harwin.com/technical_resource/ - Accessed: 27.11.2013

C.2 Measurement System

The beam angle of the electron gun should be as narrow as possible to reduce influence of the measurements done by the m-NLP system. It is therefore of interest to characterize the beam angle. Two possible solutions are presented here, with a more detailed look on the second one.

The first solution is to mount a small probe, for instance one of the Langmuir probes used in the m-NLP system, to a movable boom. The probe is then swept in both x and y direction and the current is measured at each point. The total current from the gun is found by integrating the current at each point, and the beam angle is found from the geometry. This solution will have a negligible effect on the electric field in the measurement setup and it will give the best measurement setup, albeit the most complicated.

The second solution is to have a plate with conductive zones insulated from each other. This plate can be made in the same manners as the electron gun with a printed wiring board. The current is then measured from each zone and the distribution is directly mapped. The beam angle can be found from the geometry. This solution will influence the electric field to a more extent than the first solution, since the collector plate will have more conductive areas than the langmuir probe. One drawback with this solution is that multiple measurement devices are needed unless time multiplexing is used. This is,however, the most feasible solution.

C.2.1 System Overview

The system consists of a collector plate PCB with conductive zones separated from each other. As the zones will be on the same potential, leakage current is not a problem and the insulating parts between the zones can be minimized. An interface board consisting of relays is controlled by a NI USB-6008 DAQ USB Device for time-multiplexing of the single channel Keithley SMU. The EGMS.vi labview program must be expanded to control the NI USB-6008, and an algorithm for multiplexing between the different zones at each voltage in the characterization procedures must be implemented. The proposed relays are the electromagnetic 2200 Series Reed Relays with insulation resistance of up to $10^{12}\Omega$, which limits the leakage current. Cheaper relays with lower leakage resistance can be chosen if the anode in the electron gun is at ground potential. The relay is a form C relay which means the output line switches between to input lines. The digital I/O lines on the USB NI-6008 is configured as open drain and operates on 5 V TTL logic levels with a current drive of 8.5 mA. This is enough to drive the BC546 BJT transistor which is used to power the reed relays with the external +5 V power supply on the DAQ box. A 1N4148 flyback diode is connected in parallel with the coil to suppress the voltage spikes that occur when the transistor turns off. The system can be seen in Figure C.1.

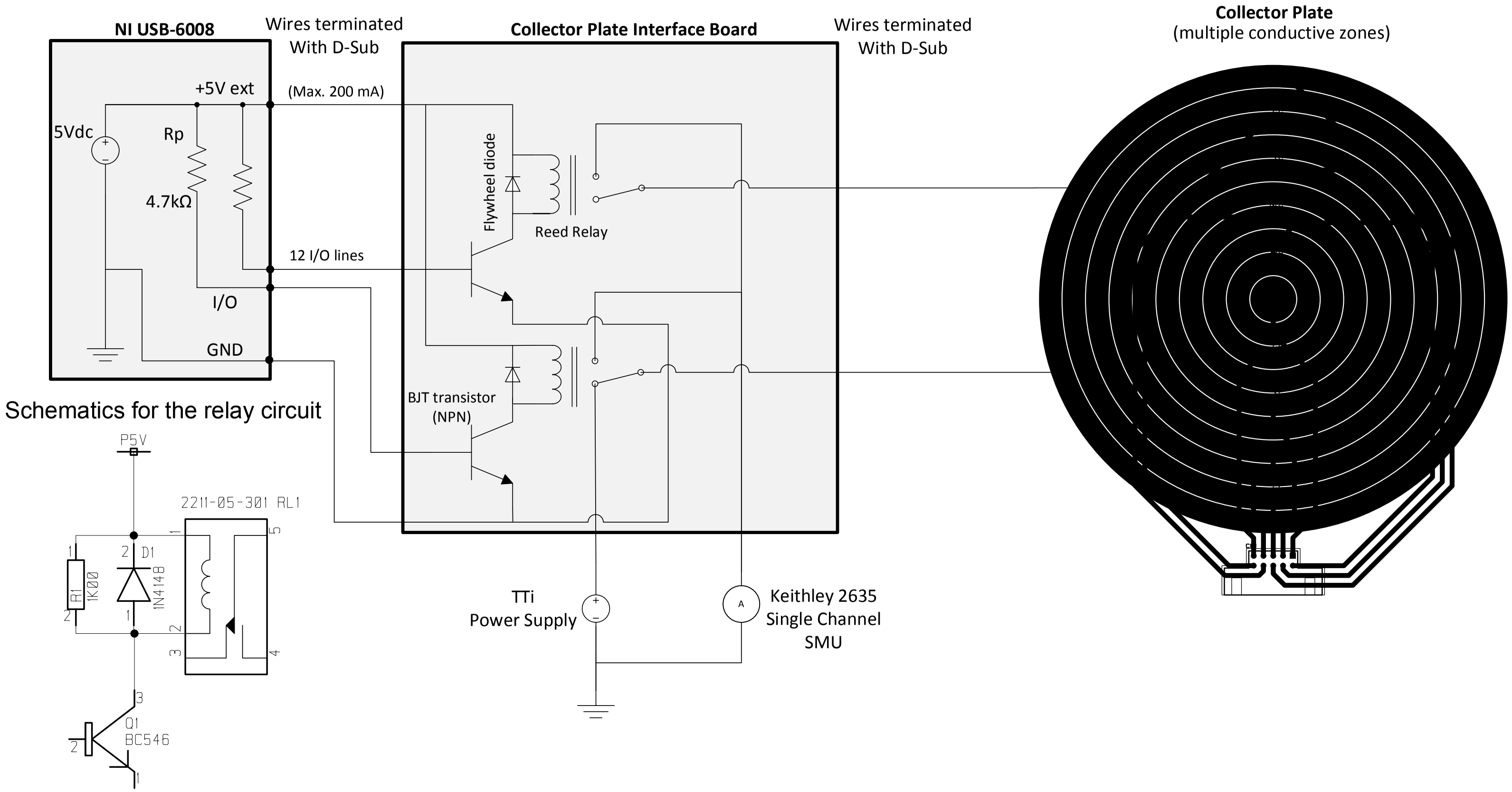

Figure C.1: Shows a system overview of the proposed method for measuring the beam angle.

Appendix D

Prototypes and Concepts

D.1 Prototype 0.1

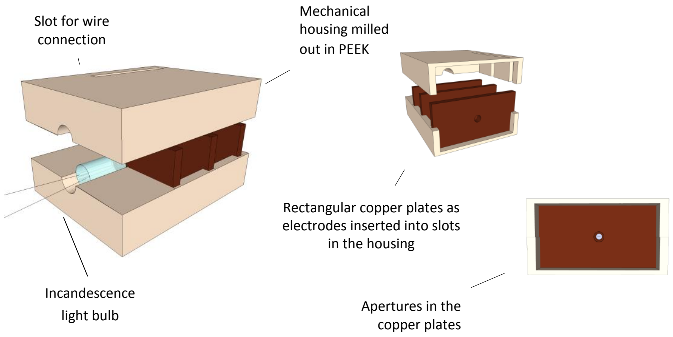

Cathode	Electrodes	Mechanical housing	Focusing
[✓ Thermionic]	[✓ Metal plates]	[✓ PEEK house]	Wehnelt
Field	Embedded in housing	Supporting rods	Pierce type
	Plated through-holes	Aluminium house	[✓ Einzel lens]
			Magnetic lens
			[✓ None]

Figure D.1: Illustrates the concept for prototype 0.1. The concept involves embedding the cathode together with the electrodes inside a mechanical housing milled out in PEEK. The proposed miniaturized light bulb is placed inside a socket in the mechanical housing and glued to the structure with a low outgassing RTV glue. The wire leads from the light bulb is soldered onto a connector outside the housing together with wires from the electrodes. The electrodes are made from rectangular shaped copper plates, measuring $12 \times 6 \times 1$ mm, with apertures drilled in the centre of the plates. Wires are threaded through an aperture in the top half of the housing and soldered onto the copper plates. To be able to test different electrode configurations, such as the distance between the plates, several slots is incorporated into the housing. The focusing possibilities with this concept, if any, were thought to be a variation of the einzel lens.

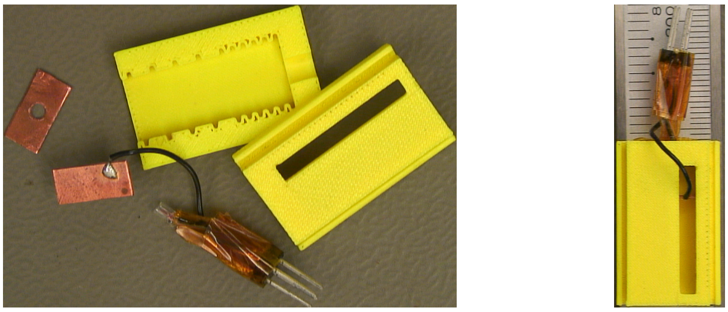

(a) (b)

Figure D.2: Shows the realization of prototype 1. Kapton, a polyimide insulating film developed by DuPont, was used instead of shrink tubes to avoid additional outgassing. Problems encountered with this prototype includes: (1) difficulties in soldering the wire to the copper plates due to heat loss, (2) no strain relief between the filament and the connector (3) aperture too close to the top edge of the electrodes and (4) exposed insulating surfaces in the electron gun might charge up due to the electron beam.

D.2 Prototype 0.2

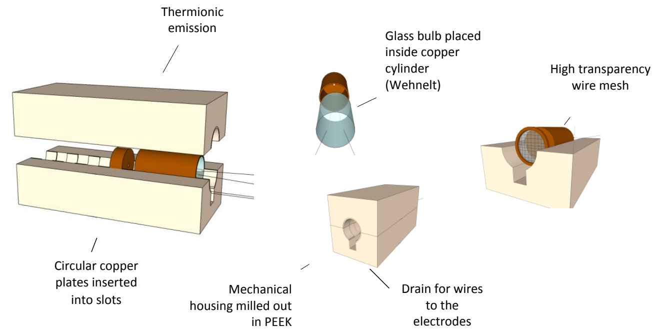

Cathode	Electrodes	Mechanical housing	Focusing
[✓ Thermionic]	[✓ Metal plates]	[✓ PEEK house]	[✓ Wehnelt]
Field	Embedded in housing	Supporting rods	Pierce type
	Plated through-holes	Aluminium house	[✓ Einzel lens]
			Magnetic lens
			[✓ None]

Figure D.3: Illustrates the concept for prototype 0.2 This concept was based on the previous concept except for some minor changes. The miniature light bulb is placed inside a copper cylinder, with an outer diameter of 4 mm, to resemble the Wehnelt cylinder described in Section 4.5. Wires are soldered onto circular electrodes and the wires are lead through a drain at the bottom half of the housing where they are soldered onto a connector outside the housing. The electrodes and the cylinder are placed inside circular slots. A high transparency wire mesh is proposed as an alternative to the apertured anode.

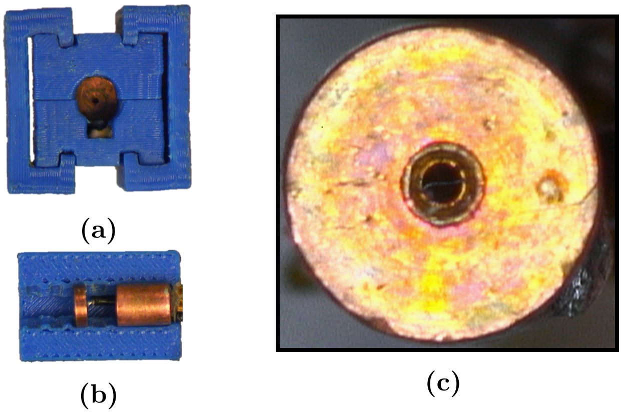
(a) (b) (c)

Figure D.4: Shows the realization of prototype 2. Figure (a) shows a photograph of the prototype from the side with an anode placed in front, while (b) shows the prototype from the front. Figure (c) shows the filament placed inside the cylinder. Problems encountered with this prototype includes: (1) difficulties handling in handling the prototype due to small dimensions, (2) electrical field from the wires in the drain possibly affecting the particle trajectory, (3) accuracy of 3D printer not good enough for the small sizes and (4) electrodes will jump inside the slots destroying the solder-joints during launch. Point (1) and (2) from the last prototype is still valid.

D.3 Other Concept Proposals

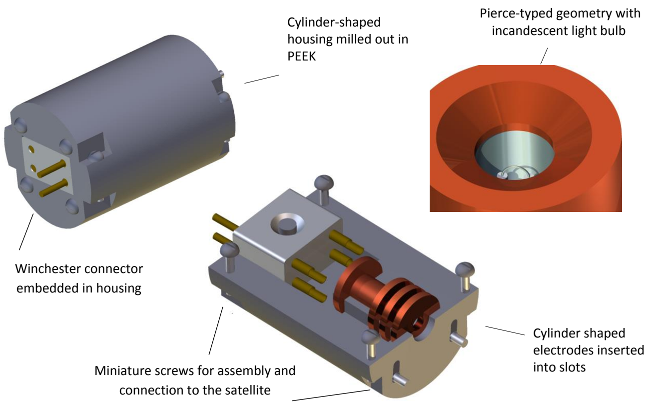

Cathode	Electrodes	Mechanical housing	Focusing
Thermionic	**Metal plates**	**PEEK house**	**Wehnelt**
Field	Embedded in housing	Supporting rods	**Pierce type**
	Plated through-holes	Aluminium house	**Einzel lens**
			Magnetic lens
			None

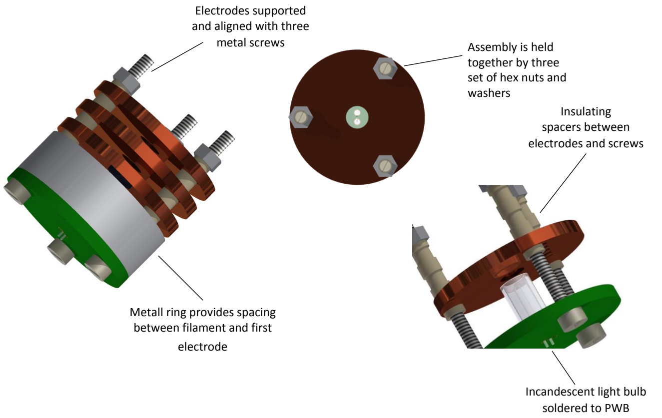

Cathode	Electrodes	Mechanical housing	Focusing
Thermionic	**Metal plates**	PEEK house	**Wehnelt**
Field	Embedded in housing	**Supporting rods**	**Pierce type**
	Plated through-holes	**Aluminium house**	**Einzel lens**
			Magnetic lens
			None

Figure D.5: Shows two other concepts that were generated during the thesis.

D.4 Prototype 1 - Mechanical Drawings and PWB Layout

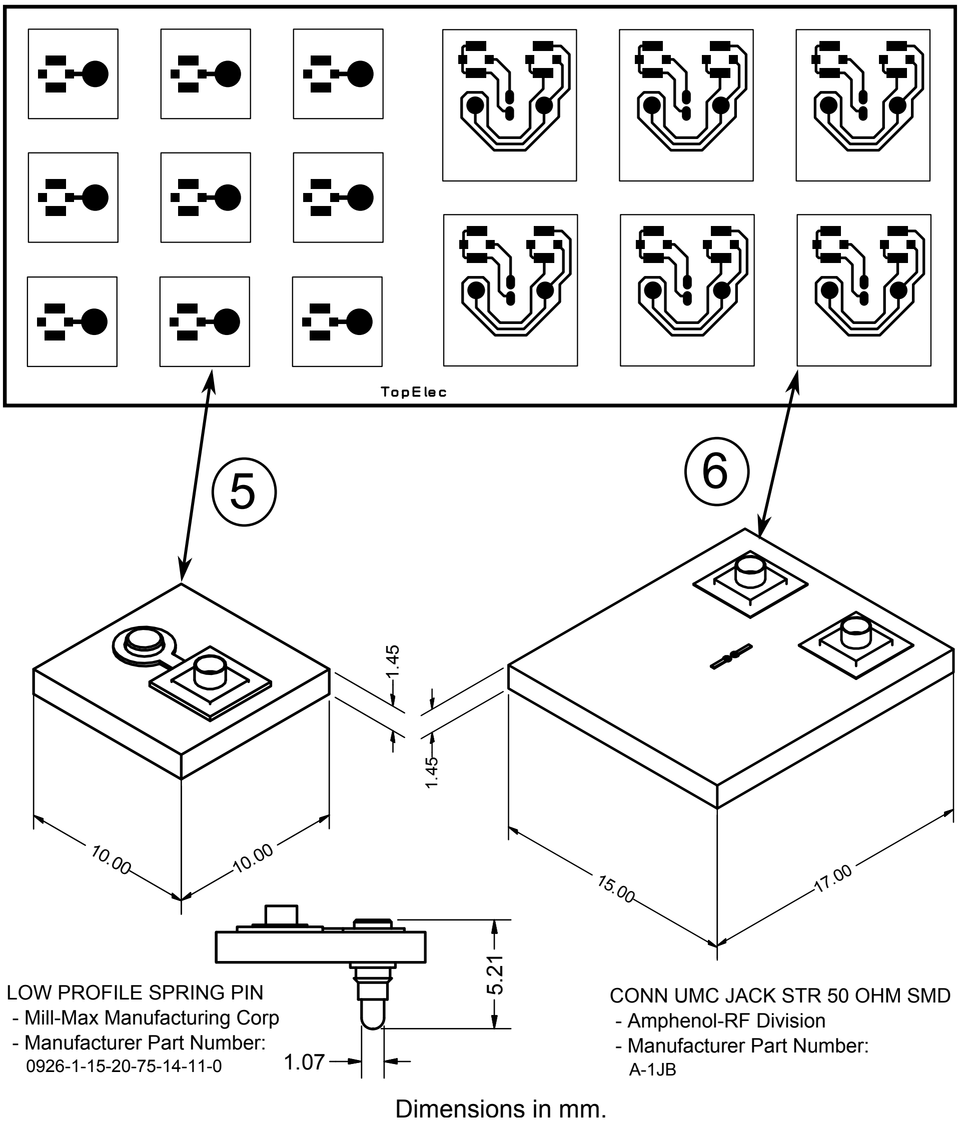

Figure D.6: Shows the PWB layout in the upper figure, and mechanical sketch of the boards in the lower figure. It should be noted that there was a mismatch between the thickness of the PWB and the thickness of the slot in the mechanical housing. The dimensions are in mm.

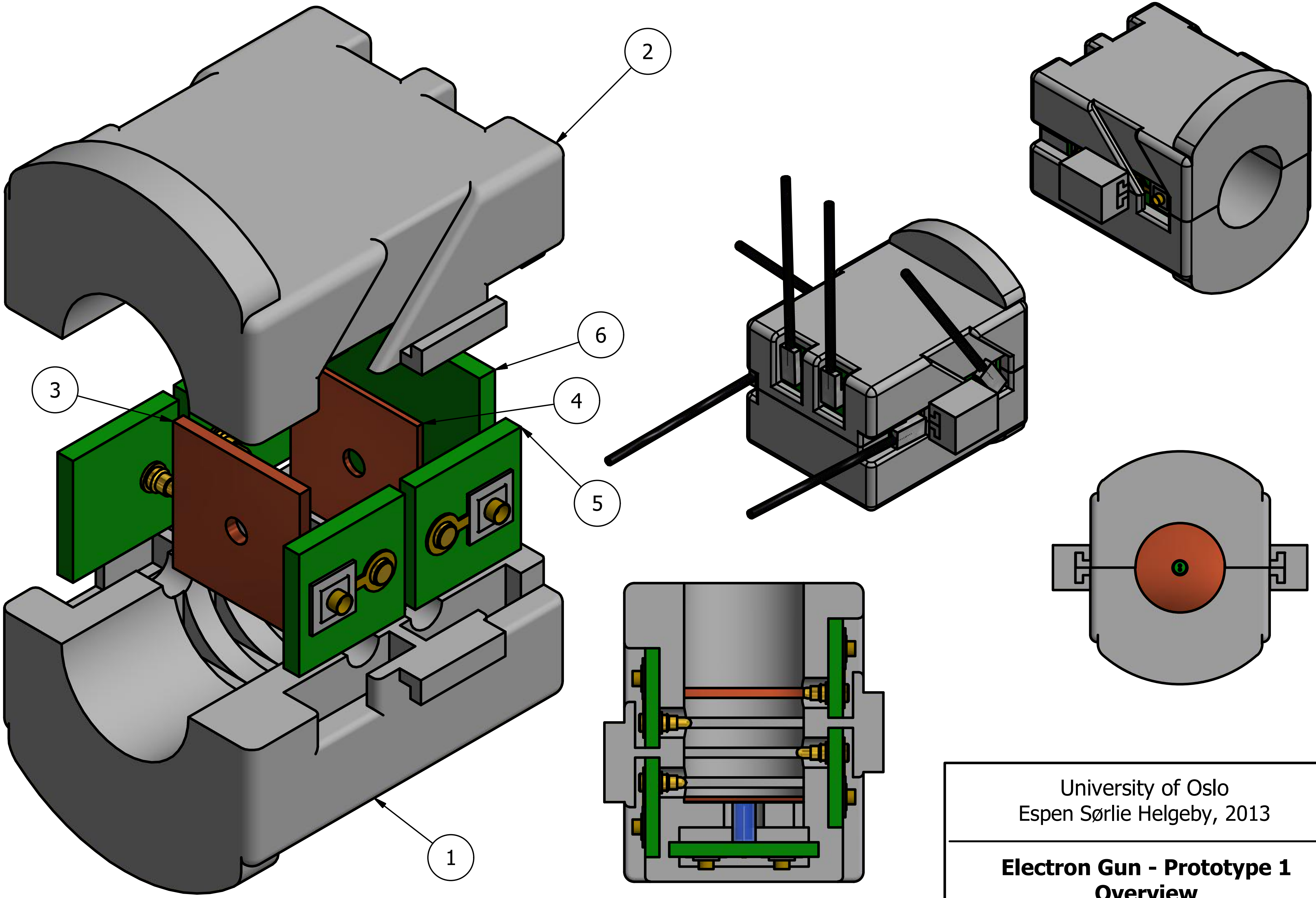

University of Oslo
Espen Sørlie Helgeby, 2013

Electron Gun - Prototype 1
Overview

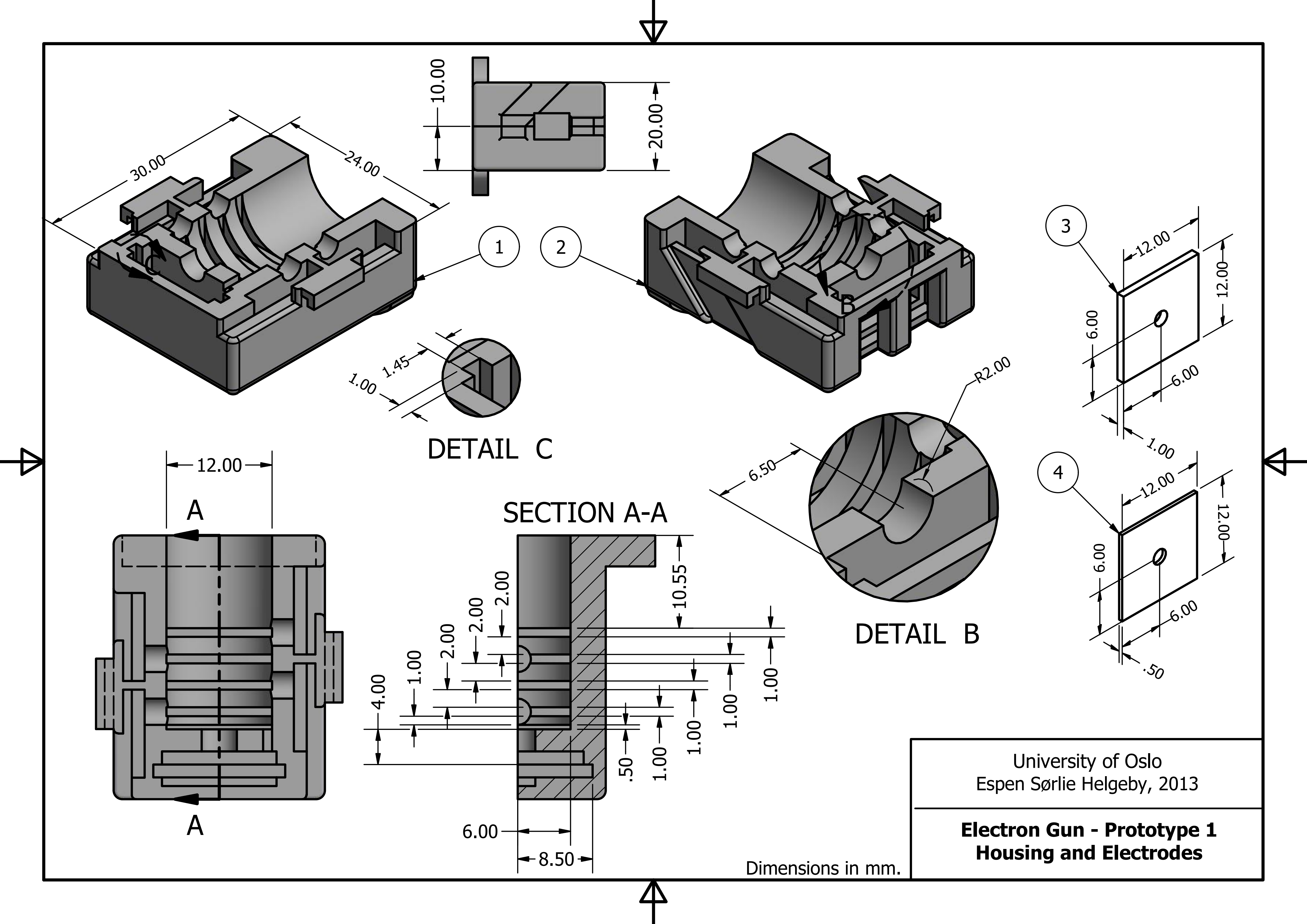

Dimensions in mm.

University of Oslo
Espen Sørlie Helgeby, 2013

Electron Gun - Prototype 1
Housing and Electrodes

D.5 Prototype 2 - Mechanical Drawings and PWB Layout

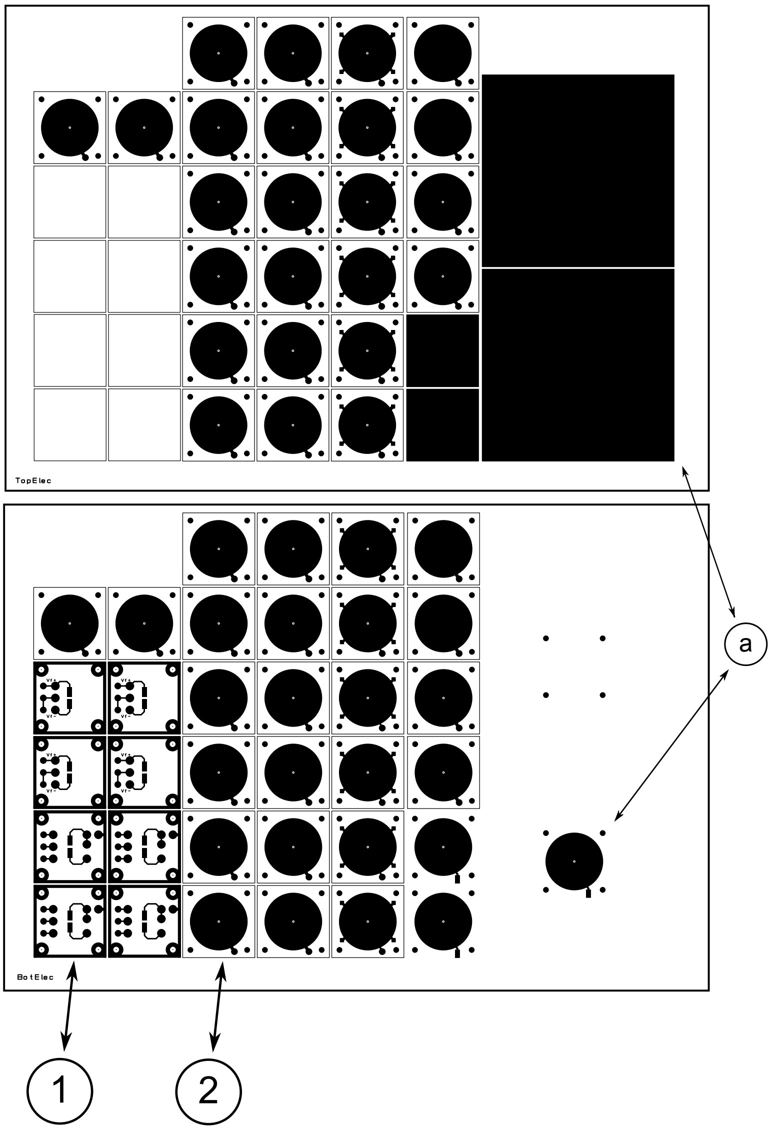

Figure D.7: Shows the PWB layout used in prototype 2.

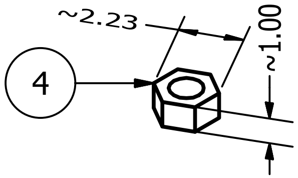

Dura-Tec Hex Nut
The Hilsinger Company
Part no. : 05/818/0000

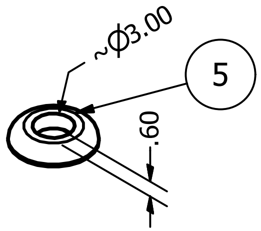

Metal Cup (Washers)
The Hilsinger Company
Part no. : 05/104/0000

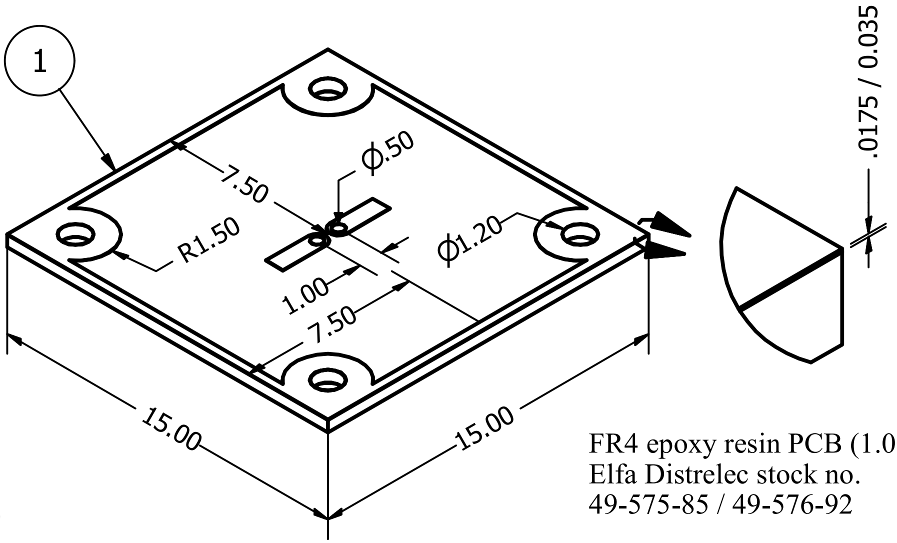

FR4 epoxy resin PCB (1.00 mm / 0.50 mm)
Elfa Distrelec stock no.
49-575-85 / 49-576-92

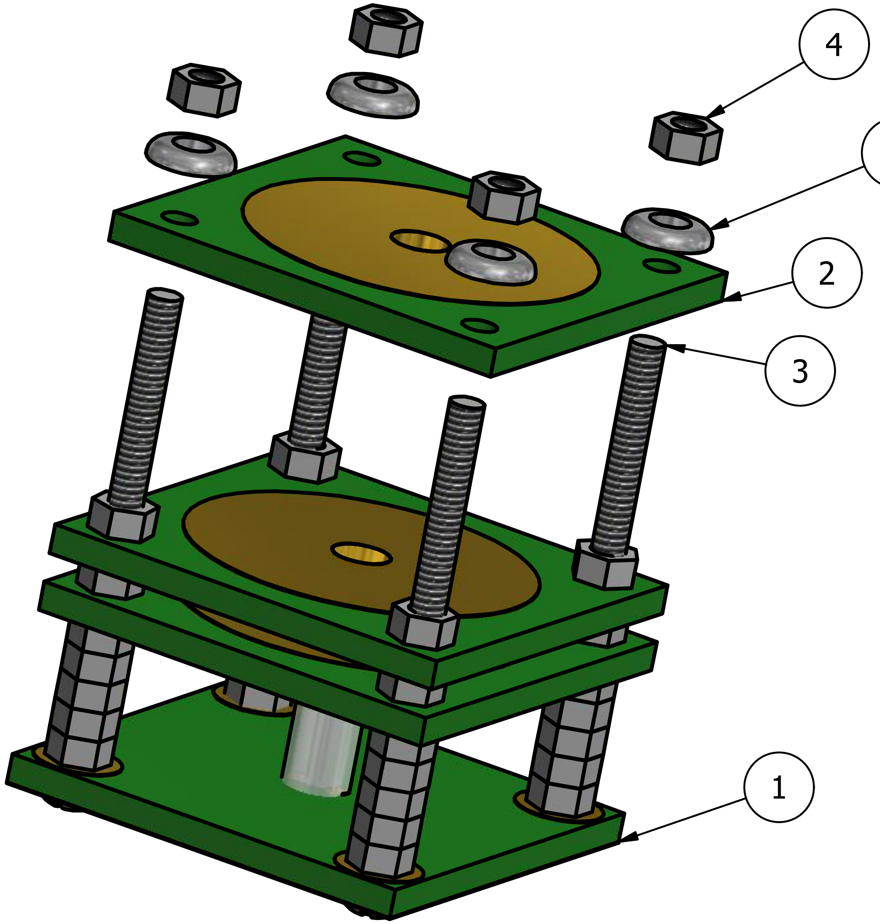

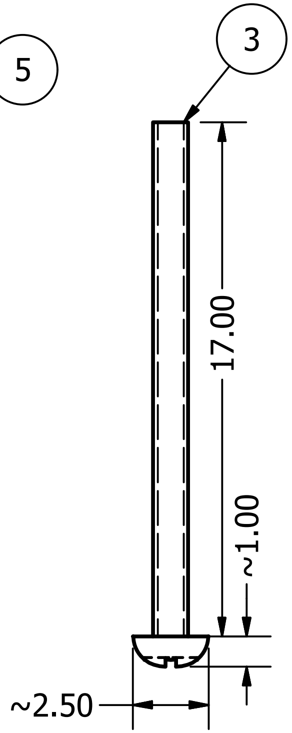

Dura-Tec Lens Screws
The Hilsinger Company
Part no. : 05/819/0000

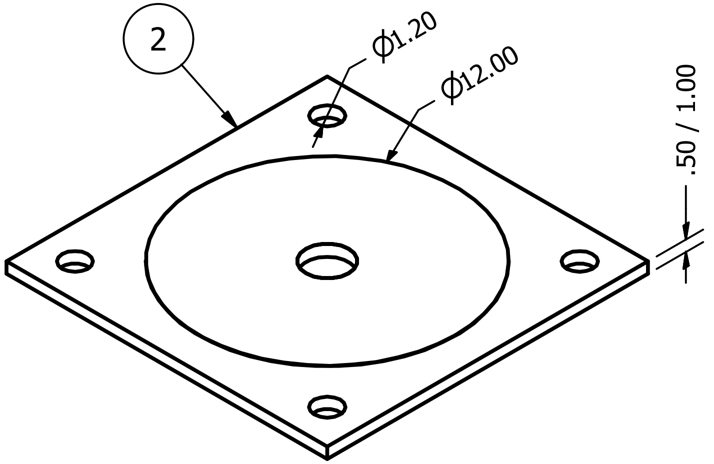

Dimensions in mm.
~ measured values

University of Oslo
Espen Sørlie Helgeby, 2013

Electron Gun - Prototype 2

Appendix E

Datasheets

E.1 Qioptiq Solar Cell Coverglass

Solar Cell
Coverglasses

Qioptiq Space Technology

- Design and manufacture of radiation-stable Coverglasses
- 40 years of Space Heritage
- Space Qualified
- Choice of glass types (CMX, CMG, CMO)
- Supply 80% of the world's Coverglasses
- Bespoke solutions to meet every mission need

Courtesy of European Space Agency

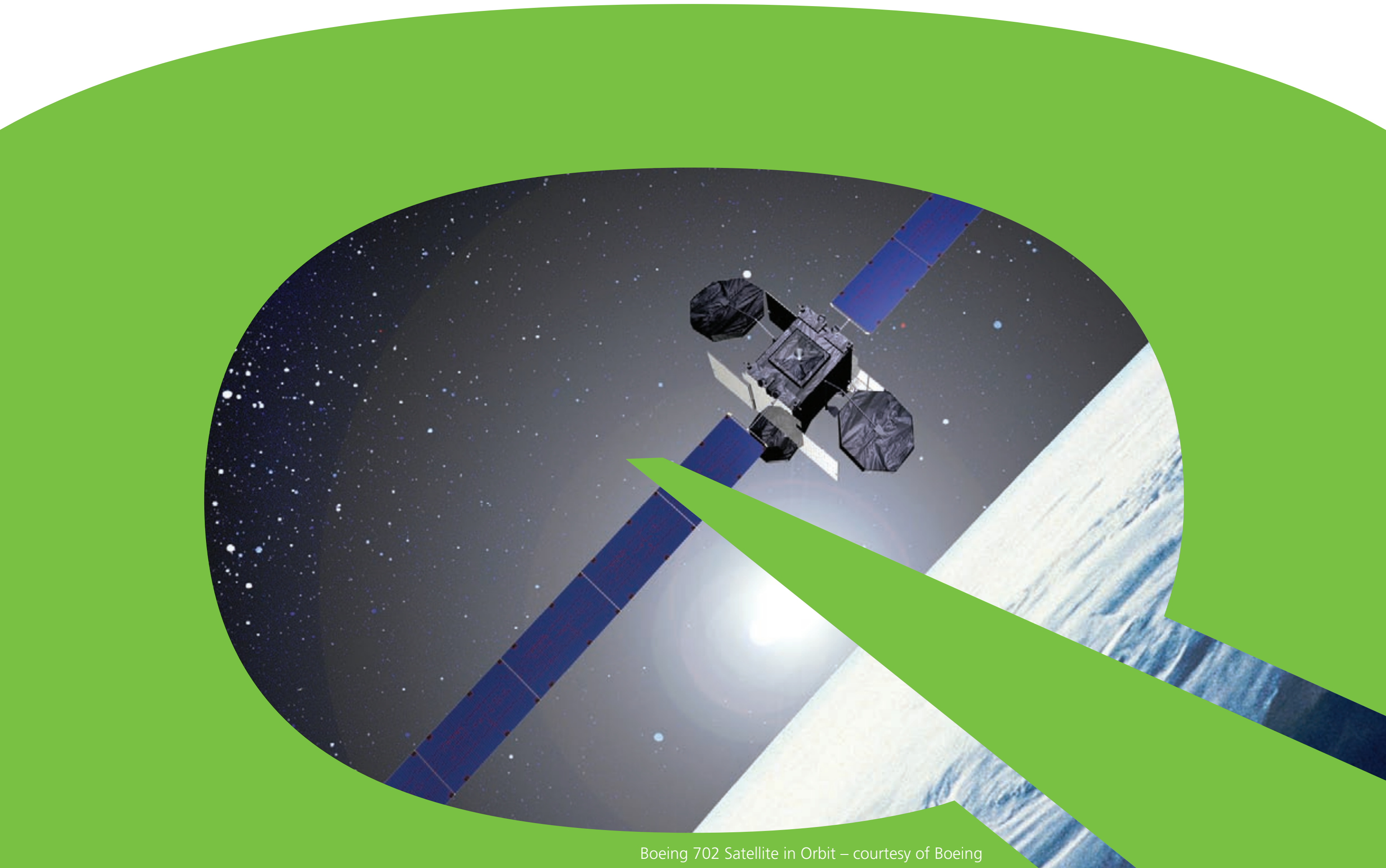

Boeing 702 Satellite in Orbit – courtesy of Boeing

Solar Cell
Coverglasses

Minimum Coverglass Transmission specifications with 0.10mm thick CMX, CMG and CMO glass types

		350 - 400nm	400 - 450nm	450 - 700nm	600 - 800nm	650 - 900nm	450 - 1100nm	900 - 1800nm	IR Cut-off	Min Emittance	Front Surface Resistance
CMX	Uncoated	73.5	91.5	94.0	95.0	95.0	95.0	95.0		0.88	
CMG		83.5	92.5	94.5	95.0	95.0	95.0	95.0		0.88	
CMO		88.0	94.0	94.5	95.0	95.0	95.0	95.0		0.88	
CMX	AR	73.5	93.0	96.5	97.5	97.5	96.5	96.5		0.88	
CMG		83.5	94.0	97.0	97.5	97.5	96.5	96.5		0.88	
CMO		88.0	95.5	97.0	97.5	97.5	96.5	96.5		0.88	
CMX	Conductive AR	73.5	94.0	96.5	97.0	97.0	96.5	96.0		0.86	<10M Ohms
CMG		83.5	95.0	97.0	97.0	97.0	96.5	96.0		0.86	<10M Ohms
CMO		88.0	96.0	97.0	97.0	97.0	96.5	96.0		0.86	<10M Ohms
CMX	Conductive	71.0	89.0	94.0	95.0	95.0	94.5	94.5		0.84	<5K Ohms
CMG		80.0	89.0	94.0	95.0	95.0	94.5	94.5		0.84	<5K Ohms
CMO		80.0	89.0	94.0	95.0	95.0	94.5	94.5		0.84	<5K Ohms
CMX	UV Reflector	73.5	92.0	96.0	96.5	96.5	96.0	94.0		0.86	
CMG		83.5	93.0	96.5	96.5	96.5	96.0	94.0		0.86	
CMO		88.0	94.5	96.5	96.5	96.5	96.0	94.0		0.86	
CMX	AR/IRR Silicon Blue Red Silicon	73.5	89.0	96.0	96.0	96.0	95.0		1165+/- 50nm	0.86	
CMG		83.5	90.0	96.0	96.0	96.0	95.0			0.86	
CMO		88.0	92.0	96.0	96.0	96.0	95.0			0.86	
CMX	UVR/IRR Triple Junction (PS 703)	73.5	92.0	96.5	96.5	96.5	95.0		1315+/- 35nm	0.86	
CMG		83.5	93.0	96.5	96.5	96.5	95.0			0.86	
CMO		88.0	88.0	96.5	96.5	96.5	95.0			0.86	

1. All spectral data measured at normal incidence in 1.43 matching index
2. Tolerances on specification values are available from relevant product specifications
3. Spectral data is for 0.10mm/0.004" coverglasses, please refer to relevant specification for spectral performance of other thicknesses.

Physical Properties

Property	CMX	CMG	CMO
Density	2.605 g/cm^3	2.554 g/cm^3	2.536 g/cm^3
Refractive Index	1.5265	1.516	1.51
Youngs Modulus	75GNm^{-2}	77GNm^{-2}	70GNm^{-2}
Poissons Ratio	0.22	0.20	0.22

For technical information contact:

Qioptiq Space Technology
sales@uk.qioptiq.com
phone +44 (0)1745 589833
www.qioptiq.com

Mechanical Properties

Thickness:	0.050mm to 0.50mm / 0.002" to 0.02" Special thicknesses on request
Tolerancing:	LxW ±0.05mm / 0.002"
Surface Finish:	As drawn to: MIL-PRF-13830B, 80/50 scratch dig
Parallelism:	0.05mm per 20mm
Perpendicularity:	90° ± 0° 30'
Coating:	Uncoated area, masked by coating tooling, shall not exceed 1% of the total coverglass area
Edge Quality:	Chemically etched for strength enhancement
Toughening:	CMX and CMG glass can be chemically toughened if required
Humidity Resistance:	98% ± 2% relative humidity for 72 hours @ 50°C ± 20°C
Adhesion:	Using cellulose tape to MIL-M-13508
Abrasion:	20 strokes with 6mm pencil type eraser to MIL-E-12397 loaded to 10N
Radiation Resistance:	UV exposure, electron, low energy proton, high energy proton - please refer to relevant specifications
Thermal Cycling:	Details on request